CATCH OF THE NET

Cybersecurity refers to the provisions and policies adopted to prevent and monitor unauthorized access, misuse, modification or denial of computer networks and network-accessible resources. With the emergence of the Web 2.0 and wireless technologies, cybersecurity is a major challenge for organisations, with new and increasingly more complex threats emerging on a daily basis in various forms. One of the most common form is hackers, who often exploit networking devices, including firewalls, routers and switches, for personal gain or profit, or as recent events have shown, for power, fame or, quite simply, personal satisfaction. Hackers can gain access to large amounts of lucrative information available inside networks, such as social security numbers, credit card numbers and other personally identifiable information which can misused in many ways. Furthermore, attacks such as distributed denial-of-service (DDoS) can cripple large networks or important companies. Hence, cybersecurity is an important issue to focus on as threats to computer networks can cause major losses in terms of time, money and resources. The following are relatively interesting and useful websites on cybersecurity:

1) Computer Emergency Readiness Team (CERT): Cyber Security Tips
http://www.cert.org/tech_tips/home_networks.html

2) National Energy Research Scientific Computing Center: Cybersecurity
http://www.nersc.gov/nusers/security/tutorial

3) Network and Computer Security Tutorial
http://www.comptechdoc.org/independent/security/recommendations
Provides introductory material and tutorials on key aspects of cybersecurity, including terminologies, policies, risks, protocols and applications.

4) CyberSecurity Malaysia: CyberSafe
http://www.cybersafe.my

5) National Cyber Security Alliance: StaySafeOnline
http://www.staysafeonline.org
Online portals that are aimed at increasing awareness among various stackholders on technological and social issues relating to internet usage.

6) CyberSecurity Malaysia: e-Security Bulletin
http://www.cybersecurity.my/en/knowledge_bank/bulletin/content/main/detail/182

7) Department of Homeland Security: Cyber Security Research and Development Center
http://www.cyber.st.dhs.gov/resources.html

8) Network Security Journal
http://www.networksecurityjournal.com
Resource centres providing recent articles and manuscripts on cybersecurity threats and solutions.

9) Federal Networking and Information Technology Research and Development (NITRD) Program: Federal Cybersecurity Game-change R&D
http://cybersecurity.nitrd.gov

10) US Cyber Command: Cybersecurity
http://www.defense.gov/home/features/2010/0410_cybersec

11) Network World: Security Research Center
http://www.networkworld.com/topics/security.html
Online portals providing up-to-date coverage of cybersecurity technologies and issues.

DEFENCE S&T TECHNICAL BULLETIN

BULETIN TEKNIKAL S&T PERTAHANAN

VOL. / JIL. 4 | NO. / BIL. 1 | YEAR / TAHUN 2011 | ISSN 1985-6571

CONTENTS

STRIDE ™

SCIENCE & TECHNOLOGY RESEARCH INSTITUTE FOR DEFENCE
INSTITUT PENYELIDIKAN SAINS & TEKNOLOGI PERTAHANAN

ISSN 1985-6571

AIMS AND SCOPE

The Defence S&T Technical Bulletin (*Buletin Teknikal S&T Pertahanan*) is the official technical bulletin of the Science & Technology Research Institute for Defence (STRIDE). It contains articles on research findings in various fields of defence science & technology. The primary purpose of this bulletin is to act as a channel for the publication of defence-based research work undertaken by researchers both within and outside the country.

WRITING FOR THE DEFENCE S&T TECHNICAL BULLETIN

Contributions to the journal should be based on original research in areas related to defence science & technology. All contributions should be in British English or Bahasa Melayu.

PUBLICATION

The editors' decision with regard to publication of any item is final. A paper is accepted on the understanding that it is an original piece of work which has not been accepted for publication elsewhere. Contributors will receive one complimentary copy of the issue in which their work appears.

PRESENTATION OF MANUSCRIPTS

The format of the manuscript is as below:

a) Page size B5 (JIS)
b) MS Word format
c) Single space.
d) Justified.
e) In Times New Roman 11-point font.
f) Should not exceed 20 pages, including references.
g) Margins should be 2 1/2 cm or 1 inch an all sides.
h) Texts in charts and tables should be in 10-point font.

Please e-mail the manuscript to :

1) Dr. Zalini bt Yunus (zalini.yunus@stride.gov.my)
2) Dr. Mahdi bin Che Isa (mahdi.cheisa@stride.gov.my)
3) Dinesh Sathyamoorthy (dinesh.sathyamoorthy@stride.gov.my)

The next edition of the bulletin is expected to be published in November 2011. The due date for submissions is 28th September 2011. **It is strongly iterated that authors are solely responsible for taking the necessary steps to ensure that the submitted manuscripts do not contain confidential or sensitive material.**

The template of the manuscript is as follows:

TITLE OF MANUSCRIPT

Name(s) of author(s)
Affiliation(s)
E-mail:

ABSTRACT

Contents of abstract.

Keywords: *Keyword 1; keyword 2; keyword 3.*

1. TOPIC 1

Paragraph 1.

Paragraph 2.

1.1 Sub Topic 1

Paragraph 1.

Paragraph 2.

2. TOPIC 2

Paragraph 1.

Paragraph 2.

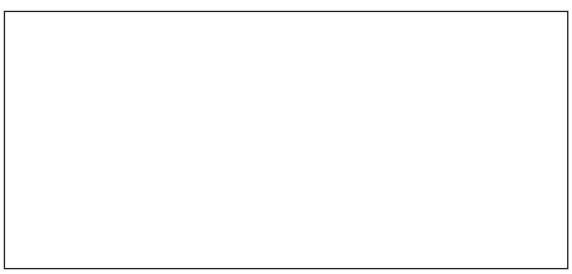

Figure 1: Title of figure.

Table 1: Title of table.

Content	Content	Content
Content	Content	Content
Content	Content	Content
Content	Content	Content

Equation 1 (1)

Equation 2 (2)

REFERENCES

Long lists of notes of bibliographical references are generally not required. The method of citing references in the text is 'name date' style, e.g. 'Hanis (1993) claimed that...', or '…including the lack of interoperability (Bohara *et al.*, 2003)'. End references should be in alphabetical order. The following reference style is to be adhered to:

Books

Serra, J. (1982). *Image Analysis and Mathematical Morphology*. Academic Press, London.

Book Chapters

Goodchild, M.F. & Quattrochi, D.A. (1997). Scale, multiscaling, remote sensing and GIS. *In* Quattrochi, D.A. and Goodchild, M.F. (Eds.), *Scale in Remote Sensing and GIS*. Lewis Publishers, Boca Raton, Florida, pp. 1-11.

Journals/ Serials

Jang, B.K. & Chin, R.T. (1990). Analysis of thinning algorithms using mathematical morphology. *IEEE T. Pattern Anal.*, **12**: 541-550.

Online Sources

GTOPO30 (1996). *GTOPO30: Global 30 Arc Second Elevation Data Set*. Available online at: http://edcwww.cr.usgs.gov/landdaac/gtopo30/gtopo30.html (Last access date: 1st June 2009)

Unpublished Materials (e.g. theses, reports and documents)

Wood, J. (1996). *The Geomorphological Characterization of Digital Elevation Models*. PhD Thesis, Department of Geography, University of Leicester, Leicester.

PHYSICAL PROPERTIES OF Al-Zn-Mg-xSn ALLOYS: HARDNESS AND ELECTRICAL RESISTIVITY STUDIES

Mahdi Che Isa*, Nik Hassanuddin Nik Yusoff, Mohd Subhi Din Yati,
Mohd Moesli Muhammad & Irwan Mohd Nor

Materials Research Group, Maritime Technology Division (BTM),
Science & Technology Research Institute for Defence (STRIDE),
Ministry of Defence, Malaysia

*Email: mahdi.cheisa@stride.gov.my

ABSTRACT

This paper discusses the effect of stanum (Sn) addition on the physical properties of Al–5.5Zn-2.0Mg-xSn (where x = 0.1 – 2.0 wt.%) alloys. These alloys were prepared using conventional casting techniques. The phases, microstructures, hardness and electrical resistivity of as-cast and heat-treated Al-5.5Zn-2.0Mg-xSn alloys were characterised using a confocal laser scanning microscope (CLSM), an x-ray diffractometer (XRD), a four point probe resistivity meter and a scanning electron microscope (SEM). The hardness of heat-treated Al-5.5Zn-2.0Mg-xSn alloys was much better than that of as-cast alloys mainly due to the dispersive distribution of Mg_2Sn phase in the aging-treated alloy. The calculated hardness values for both as-cast and heat treated Al-5.5Zn-2.0Mg-xSn alloys suggest that the decrease of hardness value with increasing Sn contents can be ascribed to formation of more Mg_2Sn intermetallic compound in these alloys. Electrical resistivity measurement shows a decrease in both as-cast and heat-treated alloys with decreasing Sn content in these alloys. It was concluded that the addition of Sn gives a strong influence on the formation of strengthening precipitates and electron mobility in the Al-5.5Zn-2.0Mg-xSn alloys.

Keywords: *Aluminium alloy; heat treatment; intermetallics; hardness; electrical resistivity.*

1. INTRODUCTION

Aluminum (Al) has several qualities that make it the preferred material for applications in the construction, aerospace, maritime, electronics, container and automotive industries. These characteristics include cost effectiveness, high strength and conductivity, low density, recyclability, desirable appearance and workability (Hoyle, 1995; Immarigeon *et al*., 1995; Miller *et al*., 2000; Stark & Staley, 1996). Combinations of magnesium (Mg) and zinc (Zn) in aluminum provide a class of heat treatable alloys, some of which develop the highest strengths presently known for commercial aluminum-based alloys. One of the main advantages of Al-Zn-Mg alloys in comparison with other aluminum-based alloys is their high strength and ductility (Lavernia *et al*., 1996). This is the result of a combination of elements that have high mutual solid solubility in aluminum and also develop unusually high precipitation-hardening characteristics (Du *et al*., 2006; Gür & Yildiz, 2004; Li *et al.*, 2008).

However, Al-Zn-Mg alloys show strong aging response due to the decomposition of the supersaturated solid solution (SSSS) and the formation of fine distribution of coherent Guinier-Preston (GP) zones and semicoherent η' precipitates (Li *et al*., 2008; Mondolfo, 1976). It has

also been established that two types of GP zones may form in these alloys (Berg *et al*., 2001; Engdahl *et al*., 2002; Wang *et al*., 2004; Werenskiold *et al*., 2000). The first type, called GP (I) zone, has spherical shape and forms at relatively low temperatures. The other, called GP (II) zone, forms above 70°C from vacancy-solute clusters and has an elongated ellipsoidal shape. The small GP(I) zones dissolve around 140 °C, while GP(II) zones are more stable and may transform continuously into the semicoherent η' phase (Desmukh *et al*., 2006; Maloney *et al*., 1999). It has been proposed that clustering of solute and possibly vacancies into vacancy-rich clusters (VRC) precedes to the formation of Guinier-Preston (GP) by the precipitation sequence below zones (Katz & Ryum, 1981; Stiller *et al*., 1999):

SSSS→VRC→GP (I) and GP (II) zones→η'(semicoherent)→η (coherent)

Stanum (Sn) is a minor alloying element in aluminium alloys. In the past, it was added to increase the fluidity of casting alloys and presently, it is added to alloys for bearings. According to the phase diagram, Al and Sn have mutual solid insolubility, with the maximum solubility of Sn in Al being about 0.1 wt %t at approximately 627 ºC, decreasing to reach a probable value of 0.05 to 0.07 %wt at the eutectic temperature, and considerably lower values at lower temperatures (Sha & Cerezo, 2004). The eutectic point occurs at 228 ºC to 229 ºC and 99.5% Sn, which is close to the melting point of Sn. In Al, Sn is usually used as an alloying element in bearing alloys in amounts of 5% or higher because of its good tribological properties (Abu-Zeid, 1990; Zeren *et al*., 2007; Xu *et al*., 2006). Murali *et al*. (1993) reported the effect of trace additions of Sn on the natural aging of Al-7% Si-Mg alloy, and showed that Sn prevented the formation of Mg_2Si. Kliauga *et al*. (2008) reported that adding 0.5 %wt. Sn to Al-Si-Mg alloys leads to a reduction of intermetallics volume fraction, causing a reduction of hardness. This effect was more pronounced in A356 type alloy. In spite of the abundance of literature in the related areas, there is very little data describing the effect of Sn addition on the electrical properties and hardness of Al-Zn-Mg alloy. Thus, this study addresses this point by investigating the precipitation of Sn and its effects on the electrical resistivity and hardness of the alloys in as-cast and heat treated conditions.

2. MATERIALS & METHODS

Al-5.5Zn-2.0Mg-xSn alloys are prepared using conventional casting technique under argon (inert) atmosphere by heating a mixture of pure metals (99.9%) in a graphite crucible. The chemical composition of the alloys was determined using an atomic absorption spectrometer (AAS) and is shown in Table 1. It should be mentioned that the iron (Fe) detected is a minor impurity in the metal that is used for the production of the alloys. The ingots were homogenised at 550 °C for 24 h in an air circulated furnace and then, quenched in air at room temperature. Sections (2 mm thick) were cut from the quenched ingots and then artificially aged at 150 °C.

Table 1: Chemical composition of fabricated Al-Zn-Mg-xSn alloys.

Alloy nominal composition (% wt.)	Contents (% wt.)				
Al-5.5Zn-2.0Mg-0.1Sn	Balance	5.5846	0.1358	1.8218	0.0239
Al-5.5Zn-2.0Mg-0.5Sn	Balance	5.5829	0.4299	1.8921	0.0237
Al-5.5Zn-2.0Mg-1.0Sn	Balance	5.4815	0.8264	1.9732	0.0746
Al-5.5Zn-2.0Mg-1.5Sn	Balance	5.3742	1.3625	1.6743	0.0224
Al-5.5Zn-2.0Mg-2.0Sn	Balance	5.5248	1.9488	1.7912	0.0271

The phases present in the alloys were determined using an x-ray diffractometer (XRD) machine from Bruker AXS with Cu K_α (λ = 1.543 Å) radiation source at scanning rate of 0.002º per second with 2θ from 20 º to 80 º. Micro structural characterisation was carried out using a confocal laser scanning microscope (CLSM). Samples for microscopic study were prepared following the standard procedure of grinding and polishing using Al_2O_3 powder. Samples were etched using Keller's reagent (2.5% HNO_3, 1.5% HCl, 1% HF and 95% H_2O, v/v), and rinsed with water and dried. The same samples were also examined with a Leo VP 1450 scanning electron microscope (SEM) coupled with INCA Energy dispersive x-ray microanalysis system. The Vickers micro hardness of the as-cast and heat treated alloys was measured at a load of 0.3 kg with a dwell time of 15 s, with at least 20 measurements being taken, and the average was reported. The electrical resistivity of the polished alloy specimen was evaluated using the four-point probe method, using a constant input current (*I*) and measuring the voltage (*V*), and using the following relationship (ASTM, 1995):

$$\rho = 2\pi S \frac{V}{I} \qquad (1)$$

where ρ = Electrical resistivity, (μΩ. mm)
S = Distance between probe point, (1.00 ± 0.01 mm)
V = Measured voltage, (μV)
I = Input current, (100 μA)

Three to four specimens of each type of alloys were tested. Tungsten carbide metal was used for electrical contacts in order to reduce contact and wiring resistances. A 100 g load was applied on the top faces of the specimens and measurements were taken for at least 10 different locations to obtain precise electrical resistivity readings.

3. RESULTS AND DISCUSSION

3.1 Phase Composition and Microstructure

Phase analysis and microscopic studies were carried out to characterise and identify the presence of new phases in the Al-5.5Zn-2.0Mg-xSn alloys in as-cast state and after the heat treatment process. The confocal micrograph of the Al-5.5Zn-2.0Mg-0.10Sn (nominal wt %) and Al-5.5Zn-2.0Mg-2.0Sn (nominal wt %) alloys, in the as-cast and heat treated conditions, are shown in Figures 1 and 2 respectively. Micro structural observation of the alloys in Figures 1(a) and 2(a) reveal the presence of dendrites with small precipitates in α-aluminium matrix and eutectic in interdendritic regions. As the Sn content increases, the volume and distribution of black precipitates in the α-aluminium matrix and interdendritic regions also increase. The as-cast Al-5.5Zn-2.0Mg-2.0Sn alloy has α-aluminium dendrites embedded in the eutectic mixture (Figure 2(a)) and also has similar micro structural features with more precipitates in the α-aluminium matrix.

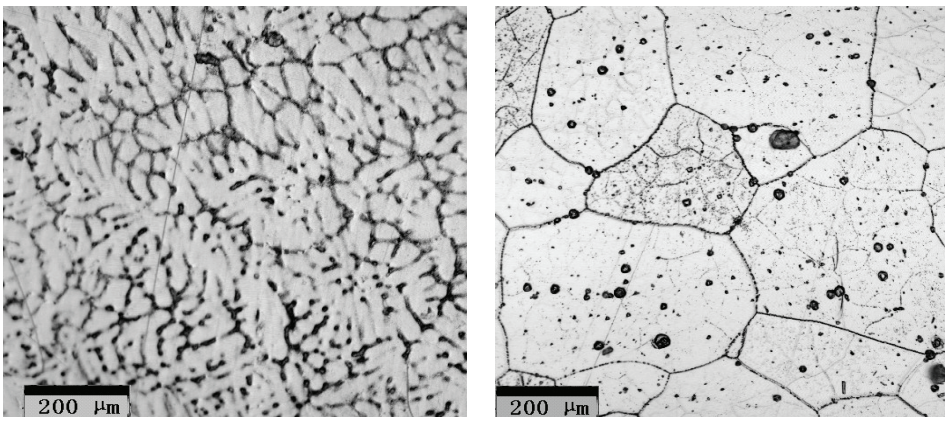

(a) **(b)**

Figure 1: Confocal micrographs of Al-5.5Zn-2.0Mg-0.10Sn wt % alloy: (a) As-cast condition; (b) Homogenised at 550 ºC for 24 hours and artificial ageing at 150 ºC for 3 hours.

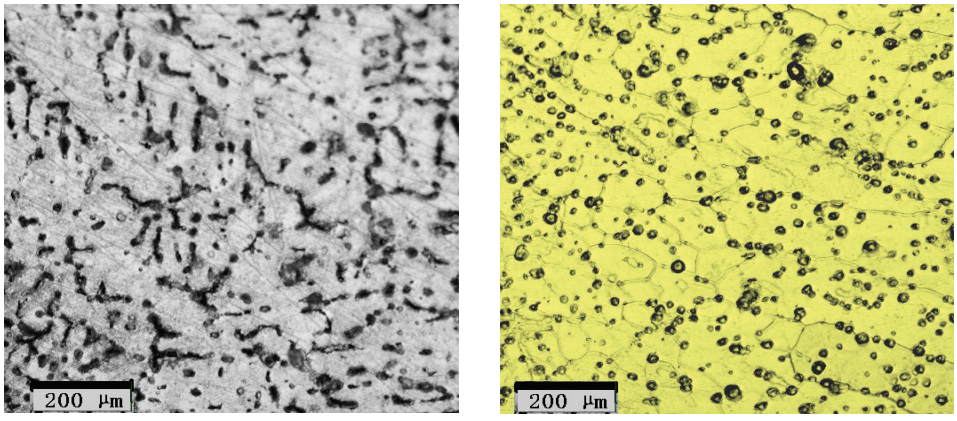

(a) **(b)**

Figure 2: Confocal micrographs of Al-5.5Zn-2.0Mg-2.0Sn wt % alloy (a) As-cast condition; (b) Homogenised at 550 ºC for 24 hours and artificial ageing at 150 ºC for 3 hours.

The microstructure of the Al-5.5Zn-2.0Mg-xSn alloys after homogenising and aging at 150 °C are shown in Figures 1(b) and 2(b) respectively. The micrographs show that after homogenising and artificial ageing, the dendritic structure has been broken down and the spheroidisation process has occurred. The micrographs reveal common features, such as spherical shape black particles in the matrix of α-aluminium and at the grain boundary. Electron microscopy coupled with energy dispersive x-ray analysis were employed in order to characterise precipitates and phases presence in the alloy. Figure 3(a) shows the backscattered electron (BSE) micrograph of the surface of as-cast Al-5.5Zn-2.0Mg-0.10Sn alloy after etching with Keller's reagent. From the micrograph, it can be determined that the presence of 2 phases in the alloy, which are α-Al and the white area, is attributed to the presence of secondary phase in the alloys. The chemical compositions of that area were found to be consisting of Al, Zn, Mg and Sn elements (Figure 3(b).

The XRD spectrums of Al-5.5Zn-2.0Mg-xSn alloy in as-cast and heat treated conditions are shown in Figures 4 and 5 respectively. The positions of the secondary phase peaks are clearly seen for higher Sn content in these alloys, thus it may be concluded that there are new phase precipitates in these alloys. Using EDX analysis, these peaks could be attributed to the formation of thermodynamically stable secondary phases. The alloys with higher Sn (0.82 – 1.94 wt %), in contrast to the low Sn (0.13 wt.%) alloy, show additional peaks which correspond to 2θ angles 22.74° and 26.33°.

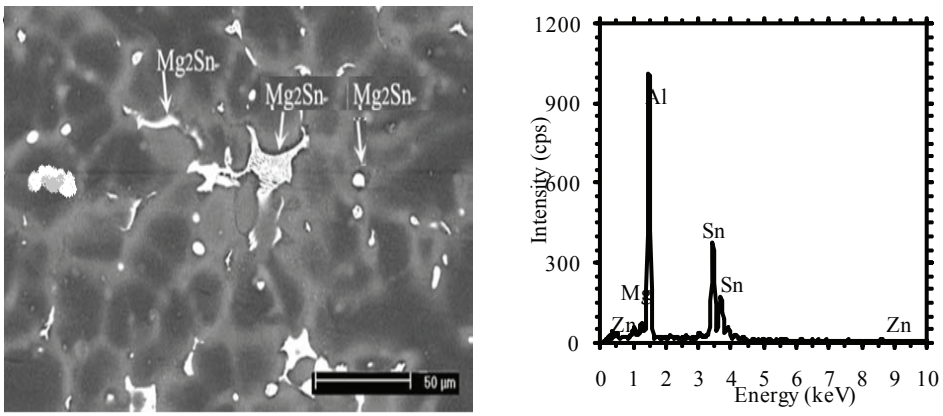

(a) **(b)**

Figure 3: (a) BSE image of the surface of as-cast Al-5.5Zn-2.0Mg-0.10Sn alloy; and (b) EDX analysis on the white area in Figure 3(a).

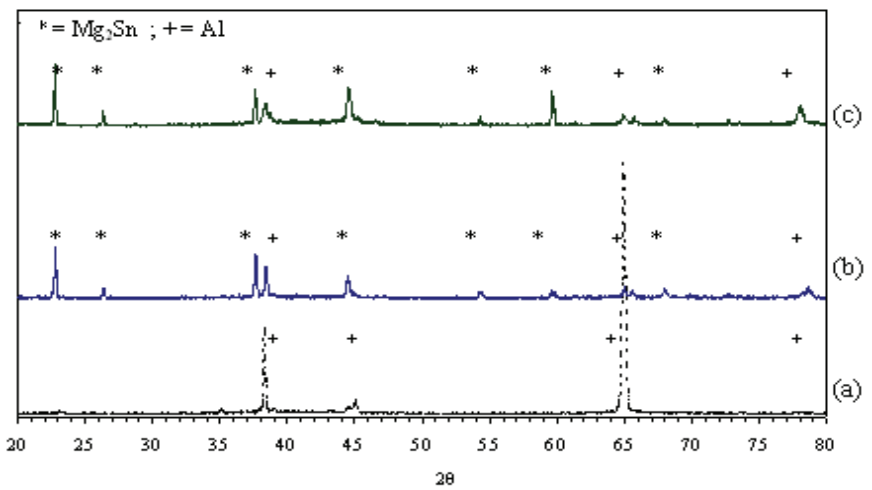

Figure 4: XRD diffractogram for as-cast Al-5.5Zn-2.0Mg-xSn alloys: (a) Al-5.5% wt. Zn-2.0% wt. Mg-0.10% wt. Sn; (b) Al-5.5% wt. Zn-2.0% wt. Mg-1.0% wt. Sn; and (c) Al-5.5% wt. Zn-2.0% wt. Mg -2.0% wt. Sn.

The lattice spacing (a= 6.76 Å) that correspond to these peaks fit to the lattice spacing of thermodynamically stable crystal structure of CaF_2 of binary alloy containing Sn

(Dyuzheva *et al.* 1995; Grosch & Range, 1996; Range *et al*., 1996). Those peaks belong to Mg_2Sn intermetallic compound. The morphology of Mg_2Sn precipitates has been characterized by TEM and exhibit three shapes: lath, polygon and plate (Zhang *et al*., 2007). Other researchers also reported that the Mg_2Sn precipitates exhibit a short rod-like Mg_2Sn phase in the as-aged magnesium alloy (Chen *et al.,* 2008; Mendos *et al.*, 2006). From the XRD patterns of as-cast and aging treated alloys in Figure 5, it is revealed that the diffraction strength of Mg_2Sn phase is evidently slightly reduced after aging-treatment. This is due to the facts that some of the Mg_2Sn compounds turn into solute atoms of Mg or Sn, and dissolve as solid solution in aluminium matrix. Mg_2Sn peaks that do not appear in the XRD spectrum of the low Sn 0.13 wt %Sn alloy in the as-cast and heat treated states are associated with their volume fractions being not high enough to form visible peaks in the XRD spectra as well as limitation of detection by the XRD machine. The presence of elements Al and Zn as shown in Figure 3(b) is due to the size of x-ray beam, which is bigger than precipitates area.

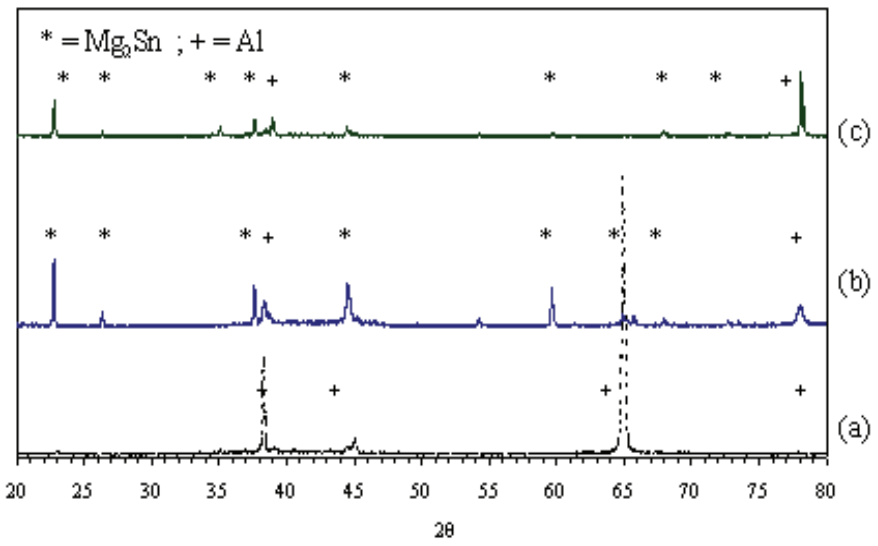

Figure 5: XRD diffractogram for heat treated Al-5.5Zn-2.0Mg-xSn alloys: (a) Al-5.5%wt.Zn-2.0% wt.Mg-0.10% wt.Sn; (b) Al-5.5% wt.Zn-2.0% wt.Mg-1.0% wt.Sn; and (c) Al-5.5% wt.Zn-2.0% wt.Mg -2.0% wt.Sn.

3.2 Mechanical Properties

Figure 6 shows the micro hardness plot of Al-5.5Zn-2.0Mg-xSn alloys as a function of ageing time at 150 ºC. The micro hardness for an ageing time equal to zero is that of as-cast alloys. The addition of Sn to the base alloy causes a decrease in the alloys hardness both in as-cast and heat treated condition. The micro hardness of as-cast Al-5.5Zn-2.0Mg-xSn alloys increases from about 77 – 100 HV to about 114–134 HV after 24 h homogenising at 550 ºC and artificial ageing at 150 ºC for 3 h, and remains high for longer aging times. The change in hardness after homogenising results from the formation of defects that have a strong influence on dislocation mobility, such as loops and voids (Kliauga *et al.*, 2008). During the homogenising stages of an Al–5.5Zn-2.0Mg-xSn alloy (550 °C/24 h), the saturated solid solution first develops solute clusters.

However, the super saturation of vacancies allows diffusion, thus leading to the formation of GP zones (Berg *et al*., 2001; Engdahl *et al*., 2002; Wang *et al*., 2004; Werenskiold *et al*., 2000). This state is known to be associated with a microstructure consisting primarily of GP zones and transitional phases. The composition of homogenised and aged Al-5.5Zn-2.0Mg-xSn alloys with aging time due to the precipitation of the Mg_2Sn phase, is responsible for the decrease in hardness (Kliauga *et al*., 2008). The decrease in hardness is bound with the growth of the Mg_2Sn phase and the transition into large and stable precipitates. The hardness decreases with aging time up to 6 h corresponding to the peak-aged and over aged conditions due to the coherent and incoherent equilibrium phase dominate the microstructure (Gür & Yildiz, 2004, Mondolfo, 1976). Therefore, in the Al-5.5Zn-2.0Mg-xSn alloy, hardening process may be influenced by the precipitation of both Mg_2Sn and $MgZn_2$ phases.

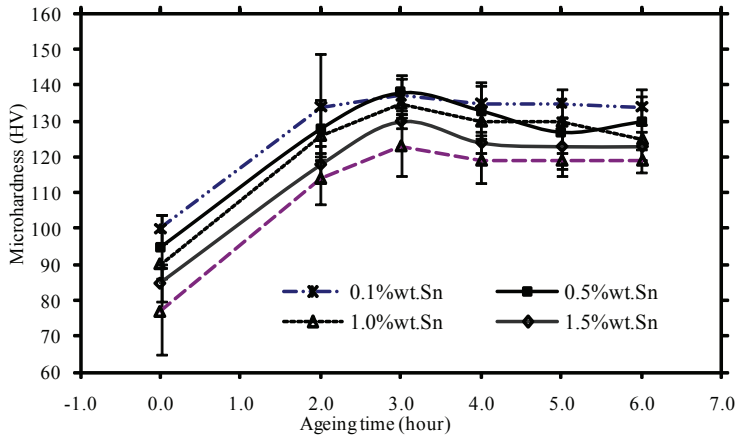

Figure 6: Micro hardness of Al-5.5Zn-2.0Mg-xSn as a function of homogenizing at 550 ºC for 24 hours and artificial ageing at 150 ºC. 0 hour ageing time indicate alloys in as-cast condition.

3.3 Electrical Resistivity

The pioneering work of Panseri & Federighi (1960) showed that electrical resistivity measurements were a very sensitive tool for studying precipitation in aluminium alloys. They also observed that during the initial stages of precipitation, the resistivity of the alloy increases as solute clusters form and grows even though this process also leads to the removal of solute atoms from solid solution. This effect has become to be known as the resistivity anomaly (Panseri & Federighi, 1960; 1963). Figure 7 shows the electrical resistivity of Al-5.5Zn-2.0Mg-xSn as a function of heat treatment. The electrical resistivity for ageing time equal to 0 h is that of as-cast Al-5.5Zn-2.0Mg-xSn alloys.

The electrical resistivity of as-cast Al-5.5Zn-2.0Mg-xSn decreases from about 38.4 – 51.5 μΩ.mm to about 30.1 – 45.2 μΩ.mm after homogenising for 24 h at 550 ºC and artificial ageing at 150 ºC for 3 h, and remains low for longer ageing times. The increase in electrical resistivity can result from the creation of defects such as vacancies and interstitials, defect clusters, dislocation loops, and voids in the alloy. In addition, the decrease of electrical resistivity of Al-5.5Zn-2.0Mg-xSn alloys after heat treatment is caused by the dissolution of Mg_2Sn strengthening particles. In fact, the dissolution of coherent and semi-coherent Mg_2Sn strengthening particles eliminates or reduces the scattering effect of these particles on electrical mobility, as shown by Guyot & Cottignies (1996).

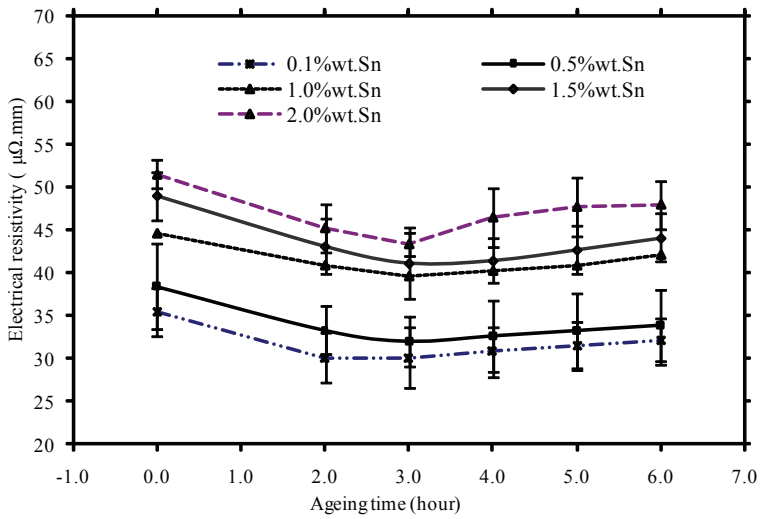

Figure 7: Electrical resistivity of Al-5.5Zn-2.0Mg-xSn as a function of homogenising at 550 ºC for 24 h and artificial ageing at 150 ºC. 0 h ageing time indicates alloys in ascast condition.

The increase of micro hardness of Al-5.5Zn-2.0Mg-xSn after the heat treatment process is caused by the dissolution of Mg_2Sn strengthening particles, which provide high strength to Al-Zn-Mg series. Since micro hardness and electrical resistivity remain constant for aging times longer than 3 h, it can be concluded that the dissolution of the Mg_2Sn strengthening particles is complete for aging times longer than 3 h. Therefore, it can be concluded that the matrix of solution heat treated alloy has higher Zn and Mg content compared to that of as-cast alloy due to the dissolution of Mg_2Sn strengthening particles during homogenising process.

Figure 7 also shows that the electrical resistivity of Al-5.5Zn-2.0Mg-xSn alloys slightly increases after 3 h of ageing time at 150 ºC. The increase in electrical resistivity shows that the metastable phase formation has almost finished after 6 h of ageing. Therefore, the reason of the increase in electrical resistivity is thought to be the purification of the matrix by means of segregation of the solute atoms and formation of semi-coherent metastable Mg_2Sn phase. As the rate of precipitation is accelerated, the foreign atoms that act as scattering centres of electrons segregate from the aluminium matrix at an enhanced rate, thus maximising their scattering effect. However, electrical resistivity measurements cannot, in principle, differentiate between GP zones since changes in resistivity are determined more by the number and size of the scattering centres than by their crystal structure or degree of coherency with aluminium alloy.

4. CONCLUSIONS

In this paper, the effects of Sn content and heat treatment on the physical properties of Al-5.5Zn-2.0Mg-xSn (%wt.) alloys have been discussed. The results of hardness and electrical resistivity investigations showed that the dispersion of Mg_2Sn particles within the Al-5.5Zn-2.0Mg-xSn alloys influences the dislocation movement and electron mobility in the alloys. The microscopic study indicates that the black spheroids of Mg_2Sn exist evenly in aging-treated alloy, hence reducing electron mobility resistance. On the other hand, these findings

indicate that the dislocations movement are more difficult in the aging-treated alloy than in the as-cast alloys. The as-cast alloys contributed to the increase in electrical resistivity and decrease in micro hardness. The magnitude of micro hardness and electrical resistivity were found to be dependent on the type and quantity of alloying element, and size and shape of phases.

ACKNOWLEDGEMENTS

The authors gratefully acknowledge the financial support by the Government of Malaysia, Universiti Kebangsaan Malaysia (UKM), and the Science and Technology Research Institute for Defence (STRIDE), Ministry of Defence, for providing research facilities and technical assistance.

REFERENCES

Abu-Zeid, O.A. (1990). Tribology and corrosion of Al-1.5wt.%Zn-5wt.%Sn ion platings, *Wear,* **139:** 313-318.

Berg, L.K., Gjønnes, J., Hansen, V., Li, X.Z., Knutson-Wedel, M., Waterloo, G., Schryvers, D. & Wallenberg, L.R. (2001). GP-zones in Al–Zn–Mg alloys and their role in artificial aging. *Acta Mater.,* **49:** 3443–3451.

Chen, J., Chen, Z., Yan, H., Zhang, F. & Liao, K. (2008). Effects of Sn addition on microstructure and mechanical properties of Mg–Zn–Al alloys. *J. Alloys Comp.,* **461:** 209-215.

Desmukh, M.N., Pandey, R.K. & Mukhopadhay, A.K. (2006). Effect of aging treatments on the kinetics of fatigue crack growth in 7010 aluminum alloy. *Mat. Sci. Eng. A,* **435-436:** 318-326.

Du, Z.W., Sun, Z.M., Shao, B.L., Zhou, T.T. & Chen, C.Q. (2006). Quantitative evaluation of precipitates in an Al–Zn–Mg–Cu alloy after isothermal aging. *Mat. Charac.,* **56:** 121-128.

Dyuzheva, T.I., Bendeliani, N.A., Dzhavadov, L.N., Kolobyanina, T.N., & Nikolaev, N.A. (1995). Crystal growth of the high-pressure phase of Mg_2Sn. *J. Alloys Comp.,* **223:** 74-76.

Engdahl, T., Hansen, V., Warren, P. J. & Stiller, K. (2002). Investigation of fine scale precipitates in Al–Zn–Mg alloys after various heat treatments. *Mat. Sci. Eng. A,* **327:** 59-64.

Grosch G. H. & Range, K.-J. (1996). Studies on AB_2-type intermetallic compounds, I. Mg_2Ge and Mg_2Sn: single-crystal structure refinement and ab initio calculations. *J. of Alloys Comp.,* **235:** 250-255.

Gür, C. H. & Yıldız, İ. (2004). Non-destructive investigation on the effect of precipitation hardening on impact toughness of 7020 Al–Zn–Mg alloy. *Mat. Sci. Eng. A,* **382:** 395-400.

Guyot, P. & Cottignies, L. (1996). Precipitation kinetics, mechanical strength and electrical conductivity of AlZnMgCu alloys. *Acta Mater.,* **44:** 4161-4167.

Hoyle, G. (1995). Recycling opportunities in the UK for aluminium-bodied motor cars. *Resources*, *Conser. Recycling,* **15:** 181-191.

Immarigeon, J-P., Holt, R.T., Koul, A.K., Zhao, L., Wallace, W. & Beddoes, J.C. (1995). Lightweight materials for aircraft applications. *Mat. Charac.,* **35:** 41-67.

Katz Z. & Ryum, N. (1981). Precipitation kinetics in Al-alloys. *Scripta Metall*., **15:** 265–268.

Kliauga, A.M., Vieira, E.A. & Ferrante, M. (2008). The influence of impurity level and tin addition on the ageing heat treatment of the 356 class alloy. *Mat. Sci. and Eng. A,* **480:** 5-16.

Lavernia, E., Rai, G. & Grant, N.J. (1986). Rapid solidification processing of 7XXX aluminium alloys: A review. *Mat. Sci. Eng.,* **79:** 211-221.

Li, Z., Xiong, B., Zhang, Y., Zhu, B. & Liu, H. (2008). Investigation of microstructural evolution and mechanical properties during two-step ageing treatment at 115 and 160 °C in an Al–Zn–Mg–Cu alloy pre-stretched thick plate. *Mat. Charac.,* **59:** 278-282.

Maloney, S.K., Hono, K., Polmear I.J. & Ringer, S.P. (1999). The chemistry of precipitates in an aged Al-2.1Zn-1.7Mg at.% alloy. *Scripta Mater*. **41:** 1031–1038.

Mendis, C.L., Bettles, C.J., Gibson, M.A. & Hutchinson, C.R. (2006). An enhanced age hardening response in Mg–Sn based alloys containing Zn. *Mat. Sci. Eng. A,* **435-436:** 163-171.

Miller, W.S., Zhuang, L., Bottema, J., Wittebrood, A.J., De Smet, P., Haszler, A. & Vieregge, A. (2000). Recent development in aluminium alloys for the automotive industry. *Mat. Sci. Eng. A,* **280:** 37-49.

Mondolfo, L.F. (1976). *Aluminum Alloy: Structure and Properties*, Butterworth and Co, London, pp. 512–19.

Murali, S., Kashyap, K.T., Ramen, K.S. & Murthy, K.S.S (1993). Inhibition of delayed ageing by trace additions in Al-7Si-0.3Mg cast alloy. *Scripta Metall. Mater.,* **29:** 1421–26.

Panseri, C. & Federighi, T. (1960). A resistometric study of pre-precipitation in Al-10% Zn. *Acta Metall.,* **8:** 217-238.

Panseri, C. & Federighi, T. (1963). Evidence for the interaction between Mg atoms and vacancies in Al-Zn 10%-Mg0.1%alloy. *Acta Metall.,* **11:** 575-584.

Range, K.-J., Grosch, G. H. & Andratschke, M. (1996). Studies on AB-type intermetallic compounds. *J. of Alloys Comp.,* **244:** 170-174.

Sha, G. & Cerezo, A. (2004). Early-stage precipitation in Al–Zn–Mg–Cu alloy (7050). *Acta Mater*., **52:** 4503–4516.

Standard Test Method for Resistivity of Electrical Conductor Materials, ASTM B193-961995, *American Society for Testing Materials*, Philadelphia, PA, USA.

Starke Jr. E.A., & Staley, J.T. (1996). Application of modern aluminum alloys to aircraft. *Prog. in Aerospace Sci.,* **32:** 131-172.

Stiller, K., Warren, P.J., Hansen, V., Angenete, J. & Gjønnes, J. (1999). Investigation of precipitation in an Al–Zn–Mg alloy after two-step ageing treatment at 100° and 150°C. *Mater. Sci. Eng. A***, 270:** 55–63.

Wang, S.Q., Schneider, M., Ye, H.Q. & Gottstein, G. (2004). First-principles study of the formation of Guinier–Preston zones in Al–Cu alloys. *Scripta Mater.,* **51:** 665-669.

Werenskiold, J.C., Deschamps, A. & Bréchet, Y. (2000). Characterization and modeling of precipitation kinetics in an Al–Zn–Mg alloy. *Mater. Sci. Eng. A***, 239**: 267–274.

Xu, G., Li, B. & Cui, J. (2006). Effect of Heat Treatment on Microstructure and Property of Al-Sn-Pb Bearing Material. *J. Iron Steel Res. Int.,* **13:** 73-76.

Zeren, A., Feyzullahoglu, E. & Zeren, M. (2007). A study on tribological behaviour of tin-based bearing material in dry sliding. *Mat. Design,* **28:** 318-323.

Zhang, M., Zhang, W., Zhu, G. & Yu, K. (2007). Crystallography of Mg_2Sn precipitates in Mg-Sn-Mn-Si alloy. *Trans. of Nonferrous Metals Soc. China,* **17:** 1428-1432.

STUDY OF THE EFFECT OF POROSITY FORMATION ON WELD JOINTS OF AA6061-T6 ALUMINIUM ALLOY USING TWO DIFFERENT FILLER METALS

Syed Roslee Sayd Bakar[1*], Mohd Faizol Ahmad Ibrahim[2], Azman Jalar[2,] Norinsan Kamil Othman[2], Syarif Junaidi Sjarifuddin Djalil [3] & Mohd Yazid Ahmad[1]

[1]Science Technology Research Institute for Defence (STRIDE), Ministry of Defence, Malaysia
[2]School of Applied Physics, Faculty of Science &Technology
Universiti Kebangsaan Malaysia (UKM), Malaysia
[3]Department of Mechanical & Material, Faculty of Engineering & Built Environment,
Universiti Kebangsaan Malaysia (UKM), Malaysia

[*]E-mail: syroslee.sybakar@stride.gov.my

ABSTRACT

The effect of porosity on weld metal of AA6061-T6 aluminium alloy with 6 mm thick plates using two dissimilar filler metals (ER4043 and ER5356) in the gas metal arc welding (GMAW) process is investigated. This paper provides a characterisation of porosity in terms of distribution and location of pores in the weldment region. Porosity characterisation was conducted using an optical microscope coupled with image analyser. The existing pores in the weldment using ER4043 (Al-Si 5%) was compared with the weldment using ER5356 (Al-Mg 5%). From this investigation, it is shown that the pores were distributed and localised mainly at the edges and root of the weldment with ER5356. However, for the weldment with ER4043, the pores were scattered mainly in the centre region. This is due to the effect of convections in the molten metal, solidification rate and gases induced during the welding process. In addition, the results of the tensile test indicated that the welding had affected the strength and ductility of the two fillers selected. The weldment with ER5356 showed a drop of 50% in ultimate tensile strength (UTS) and 40 % in elongation; while the weldment with ER 4043 showed a drop of 70% in UTS and 90% in elongation. The different principle alloying elements of these two filler metals played a significant role in the distribution of porosity in the AA6061-T6 weldments, and had influenced the tensile strength and ductility of the weld joints.

Keywords: *AA 6061-T6; arc weld; filler metal; porosity; tensile strength.*

1. INTRODUCTION

Among the 6000 series aluminium alloys, AA 6061-T6 is the most accepted applications in engineering structures due to their specific mechanical properties, corrosion resistance, heat treatability and formability from simple to complex profiles by extrusion (Cubberly, 1979, Punkari *et al.*, 2003; Othman *et al.*, 2011). ER4043 is a widely used filler metals, and can be classified as a general purpose type filler metal for welding aluminium alloys. Silicon is the major alloying element (Si-5%) which can improve the welding fluidity of weld pools

and also produces welds that are less sensitive to cracking. ER5356 filler metal with 5% magnesium as the main alloying element can provide excellent corrosion resistance in marine environments. It is commonly used for welding 5000 series aluminium base metals and is usually chosen when high shear strength is required (Cubberly, 1979).

Arc welding of these alloys are in good demand but unfortunately, weldability problems always exist because of solidification cracking, porosity and overaging of heat-affected zones (HAZ) (Ando *et al.*, 2009). In the case of aluminium welding, one common problem would be the tendency for porosity generation. Porosity is often present in arc welding, particularly for aluminium alloys and it depends on many factors, such as chemical compositions of the material and welding condition. Some studies have shown that the number, size and shape of porosities are influenced by the heat input during the welding process and the solidification rate in the weld pool (Coniglio *et al.*, 2009; Robert & Messler, 1999).

A number of researchers have conducted experiments and investigations on porosity distribution using several welding techniques such as laser beam welding, tungsten inert gas, electron beam weld and gas metal arc welding (GMAW) (Haboudou *et al.*, 2003; Fujii *et al.*, 2004; Kuk *et al.*, 2004; Kumar & Sundarrajan, 2009). They discovered that the formation and distribution of porosity has a close relationship with the rate of solidification in the weld pool. However, there is a lack of studies on the effect of filler metal on porosity distribution using the GMAW technique. Therefore, it is essential to study the effect of porosity distribution and mechanical characteristics of welded AA6061-T6 aluminium alloy with these two fillers (ER4043 and ER5356).

In this paper, the effects of the two fillers on the porosity distribution of GMAW single butt-joints are investigated. The tensile strength and mechanical characteristics of welded joints with both filler metals are investigated and discussed in term of distribution of porosity.

2. MATERIALS AND METHOD

Two 6 mm thick plates of AA6061-T6 aluminium alloy were cut into 300 x 150 mm portions using a power band saw machine. For each plate, a single 'V' butt joint weld shape was prepared using a milling machine. To secure the plates in position, the tack weld technique was applied as shown in Figure 1, with the appropriate type of clamp being used to avoid joint distortion. The single pass weld on both sides of each plate was conducted parallel to the rolling direction. The main welding parameters in the welding process, including arc current and filler feeding rate, were kept at the same condition for both samples. The AA6061-T6 aluminium alloy joints were cut into specimens, which were made into metallographic and tensile samples.

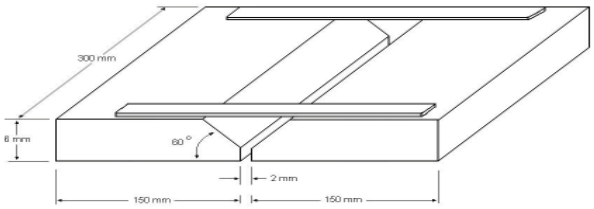

Figure 1: The tack weld and clamping technique for securing and avoiding the plates from distortion.

The micrograph of polished (unetched) specimens' weldment with ER5356 and ER4043 were captured using a Zeiss Axio vision image analyser. The percentage of pores was quantified using the image analysis software in accordance with the ASTM E1245 standard (ASTM, 2008). In addition, the tensile strength of the weld metals was measured using an Instron tensile machine (150 kN load cell), in accordance with the ASTM E8 / E8M - 09 standards (ASTM, 2009). Three specimens were prepared for each weld samples to perform the tests. A rotating weld specimen can be scanned using an X-ray CT-Scan machine to provide a 3D view of the pores in weldment, while a scanning electron microscope (SEM) provided the 3D features of the pores in the fracture surface of tensile specimen.

3. RESULTS AND DISCUSSION

The micrographs of both welded joints (Figure 2), obtained from the optical microscope, illustrated the porosity distribution in the weld metals. It clearly shows the distinction in distribution of pores between welded joints of AA6061-T6 with ER4043 and ER5356. The pores were found to be located mostly at the edges and root of the weld metal of AA6061-T6 with ER5356 (Figure 2(a)), whereas more scattered pores were seen in the centre region of the weld metal of AA6061-T6 with ER4043 (Figure 2(b)).

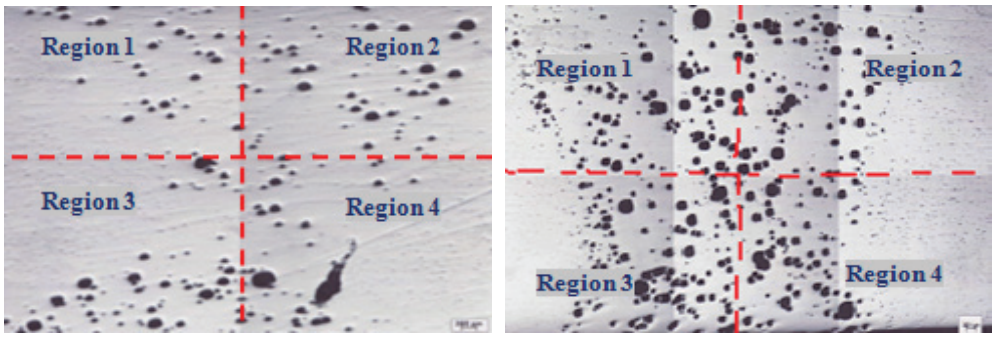

(a) **(b)**

Figure 2: Optical micrographs of the weld regions of AA6061-T6 with (a) ER5356; large number of pores at the bottom edge (regions 3 and 4) and (b) ER4043; pore concentration at the centre region of the weld metal.

A similar porosity distribution pattern was observed in the X-ray CT-scan analysis shown in Figure 3. As convection flow depends on buoyancy and surface tension gradient forces (Ando *et al.*, 2009), the location of pores in weld metals is affected by convection-movements of liquid aluminium in the weld pool during the welding process (Kou, 2003). This pattern of movement caused the bubbles to become trapped by being frozen at the edges and root of the weld. The schematic depiction of convection patterns in the weld pool is illustrated in Figure 4. The molten metal in the weld pool of AA6061-T6 with ER5356 moved from the pool edges to the weld centre, struck the bottom of the pool, and turned outwards and upwards along the pool edges (Figure 4(a)). In contrast, the bubbles in the weld pool of AA6061-T6 with ER4043 were swept outwards from the centre and downwards towards the pool edges (Figure 4(b)). This pattern of movement caused more pores to become trapped in the centre region of the weld metal.

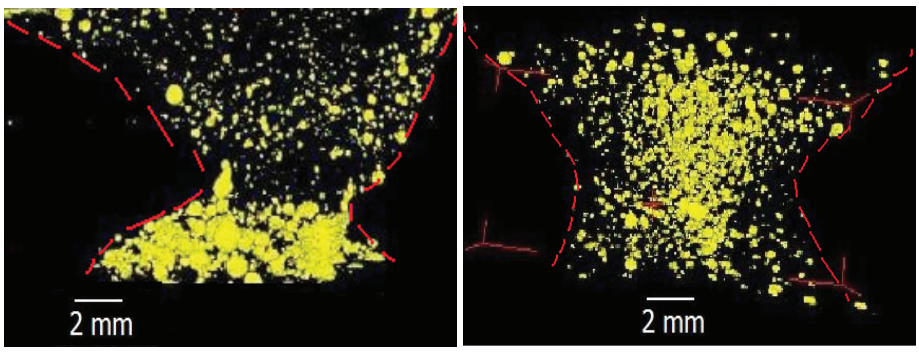

Figure 3: X-ray CT-scan analysis of AA6061-T6 with (a) ER5356; and (b) ER4043, showing 3D images of distribution and location of pores in the weldment.

Typical porosities, induced by the GMAW process, were found scattered in the microscopic examination, and can be categorised as microporosities and macrocavities with diameter size ranges of 30 - 150 µm and 150 - 300 µm respectively. The macrocavities were the dominant type of porosity in both weld regions of the weldments with ER5356 and ER4043. These types of pores are attributed to the entrapment of gas bubbles in the weld, which occurs due to large differences in solubility of hydrogen in liquid (Fujii *et al.*, 2004).

Figure 5 shows the pore and cavity distribution of each region. The number of pores in regions 1, 3, and 4 was found to be higher for the weldment with ER4043 as compared with the weldment with ER5356. However, the pore distribution in regions 2 of both micrographs was slightly similar in terms of percentage of area of pores. This may be due to the tendency of bubbles moving up to the surface of molten weld (Kou, 2003).

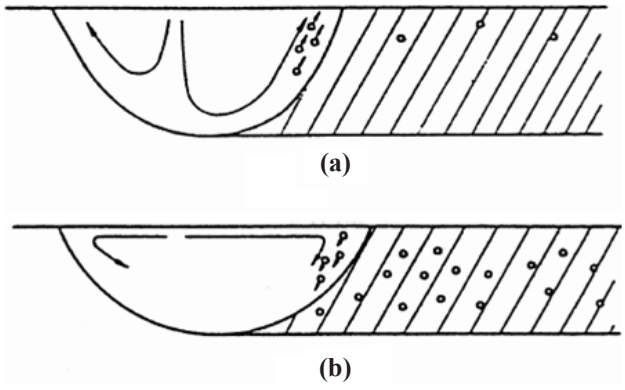

Figure 4: Flow pattern of molten metal in the weld pool influenced the porosity distribution: (a) Upwards; and (b) Downwards.
(Source: Kao, 2003)

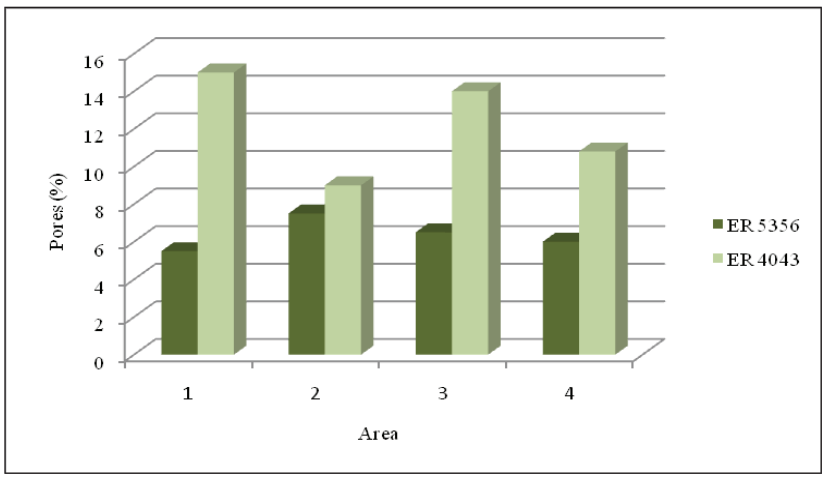

Figure 5: Percentage of areas of pores and cavities in each region of AA6061-T6 with ER5356 and ER4043.

The distributions of pores based on diameter are shown in Figure 6. The numbers of pores with diameter of 200 µm was found to be higher in the weldment with ER4043 as compared to the weldment with ER5356. Thus, the weldment with ER4043 has higher porosity as compared to that of the weldment with ER5356. More pores were quantified, using the image analysis software, in the weldment with ER4043 than the weldment with ER5356, with the total percentage area of pores for the weldments with ER4043 and ER5356 being 24% and 12% respectively. It is suggested that the convection flow forced the entrapped bubbles, and it could be due to the reaction between the shielding gas (argon) to the weld metal elements during the welding process as discussed in Kou (2003). These results are also in agreement with the findings of Hwang *et al.* (2009) and Che Lah *et al.* (2011), which reported that welds made with Al-Si filler exhibit more porosity than those made with Al-Mg filler wires.

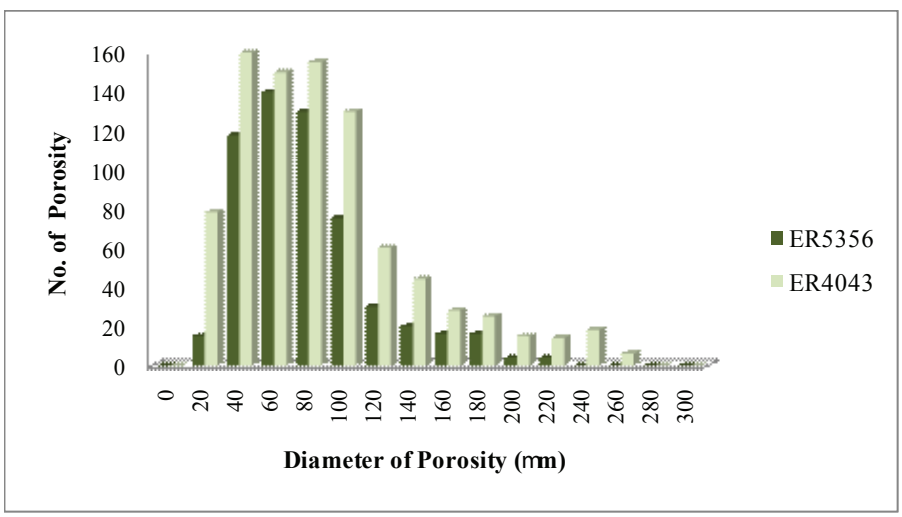

Figure 6: The distribution of pores based on diameter for AA6061-T6 with ER5356 and ER4043.

From the tensile test results shown in Figure 7, it is observed that the ultimate tensile strength (UTS) of the weldments with ER5356 and ER4043 filler metals decreased compared to the AA6061-T6 base metal, with the percentage of strength reduction being approximately 70 % for AA6061-T6 with ER4043 and 50 % for AA6061-T6 with ER5356. The tensile stress curves of both weld metals have approximately similar characteristic and values of yield strength.

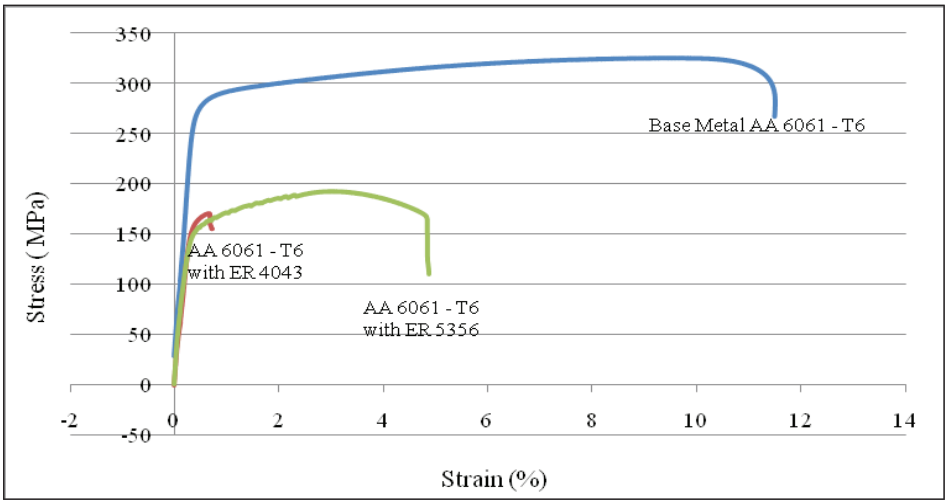

Figure 7: Tensile strength results of AA6061-T6 base metal, and AA6061-T6 with ER5356 and ER4043.

The elongation of the weldments with ER4043 and ER5356 dropped by almost 90% and 40% respectively compared to the base metal. This indicates that the elongation of weldment with ER5356 was superior to ER4043. Larger elongation is an indicator of higher material ductility, which also imparts greater resistance to fatigue crack propagation, and, ultimately, fatigue failure can be delayed. These results are consistent with the study done by Lakshminarayanan *et al.* (2009). They found that the usage of ER5356 filler metal has higher ductility compared to the usage of ER4043 filler. Maggiolino & Schmid (2008), and Aziz e*t al.* (2011) found that the magnesium content in ER5356 filler metal increases the mechanical properties of weldments through solid solution strengthening and improves strain hardening potential.

Figure 8 shows the SEM micrographs of fracture surfaces of the tensile tested weldments with ER5356 and ER4043. The pore sizes on the fracture surface of the weldment with ER5356 is larger than the pore sizes of fracture surface of the weldment with ER4043. The appearances of dimples on both samples indicate the mode of ductile failure at room temperature (Coniglio *et al.*, 2009; Engel & Klingele, 1981). The weldment with ER5356 (Figure 8(a)) exhibits fine dimples associated with highly plastic deformation characteristics, compared to the weldment with ER4043 (Figure 8(b)). The pore sizes also affect tensile strength; the coarse pores in the weldment with ER5356 provided more internal residual stress and needed extra strength and ductility to rupture (Davis, 1993). The pores and dimple characteristics exhibit a directly proportional relationship to strength and ductility, i.e., if the pore sizes are larger, the strength and ductility of the respective joint is higher and vice versa (Lakshminarayanan *et al.*, 2009).

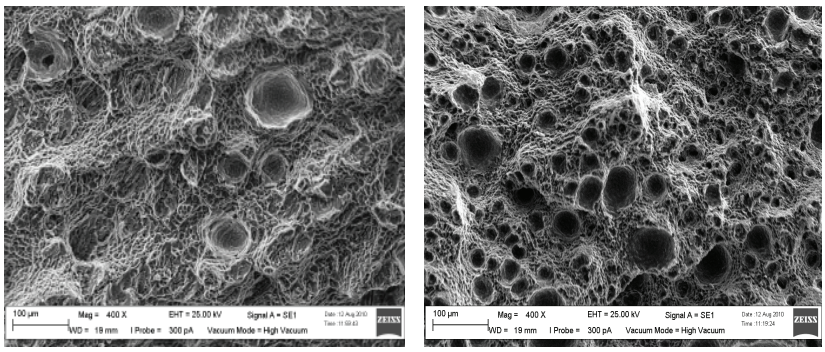

(a) **(b)**

Figure 8: SEM Fractographs of weld metals of specimens: (a) AA6061-T6 with ER5356; shows larger pore, fine dimples and highly plastic deformation features (indicated by arrow); (b) AA6061-T6 with ER4043; less plasticity features, fine pores but coarse dimples (indicated by arrow).

4. CONCLUSION

The study on the effect of porosity formation on the weld metal of AA6061-T6aluminium alloy welded joints with two types of filler metals (ER5356 and ER4043) using the GMAW process has yielded several findings. The weldment with ER 4043 exhibited larger pore sizes but similar shape as compared to the weldment with ER 5356. Both filler metals also play a significant role in the distinction in porosity distribution in AA6061-T6 weld joints due to the chemical reaction of alloying elements in molten metal during solidification process. The tensile yield strength for both weldmentsare slightly similar, but the weldment with ER5356 showed higher tensile strength and ductility than the weldment with ER4043.It can be concluded that the weldment with ER 5356 filler has relatively less porosity distribution and greater tensile behaviour than the weldment with ER 4043.

ACKNOWLEDGMENT

This work was supported by the Faculty of Science and Technology, National Malaysia University (FST-NMU) and the Structural Mechanic Branch, Science Technology Research Institute for Defence (STRIDE). The authors are highly thankful to the supporting technical staff of FST-NMU and STRIDE for their assistance and cooperation in this work.

REFERENCES

Ando Y., Fujimura, T. & Nakazaki, T. (2009). Studies on the porosity in welding joints (3rd Report): Results of experimental welding. *J. Jpn. JWS.*, **31**: 980-985.

American Society for Testing and Materials (ASTM) (2008). *ASTM E1245 – 03: Standard Practice for Determining the Inclusion or Second-Phase Constituent Content of Metals by Automatic Image Analysis*. American Society for Testing and Materials (ASTM), West Conshohocken, Pennsylvania.

American Society for Testing and Materials (ASTM) (2009). *ASTM. E8 / E8M – 09: Standard Test Methods for Tension Testing of Metallic Materials*. American Society for Testing and Materials (ASTM), West Conshohocken, Pennsylvania.

Aziz, A.A.A., Ibrahim, M.F.A., Jalar, A., Junaidi, S., Abdullah, S., Rashdi, N., & Kornain, Z. (2011). Effects of different fillers on microstructure and tensile properties of welded AA6061-T6. *Key Eng. Mater.*, **462-463**: 1189-1193.

Balasubramanian, V., Ravisankar, V. & Reddy, G. M., 2007. Influence of pulsed current welding and post weld aging treatment on fatigue crack growth behaviour of AA7075 aluminium alloy joints. *Int. J. Fatigue*, **30**: 405-416.

Che Lah, N. A., Ahmad Ibrahim, M. F., Jalar, A., Syarif, J., Othman, N. K. & Rashdi, N. M. (2011). The effect of filler ER4043 and ER5356 on porosity distribution of welded AA6061 aluminium alloy. *Adv. Mater. Res.*, **146-147**: 987-990.

Coniglio, N., Cross, C.E., Dörfel, I. & Österleb, W. (2009). Phase formation in 6060/4043 aluminium weld solidification. *Mater. Sci. Eng. A*., **517**: 321–327.

Cubberly, W.H. (Ed.) (1979). *Properties and Selection, Nonferrous Alloy and Pure Metals*. American Society for Metals, Ohio.

Davis, J. R. (1993). *Aluminium and Aluminium Alloys*. ASM International, Ohio.

Engel, L. & Klingele, H. (1981). *An Atlas of Metal Damage*. Wolfe Science Books, Munich.

Fabregue, D., Deschamps, A. & Suery, M. (2009). Influence of the silicon content on the mechanical properties of AA6xxx laser welds. *Mater. Sci. Eng. A.*, **506**: 157-164.

Fujii, H., Umakoshi, H., Aoki, Y. & Noi, K. (2004). Bubble formation in aluminium alloy during electron beam. *J. Mater. Process. Technol.*, **155-156**: 1252-1255.

Haboudou, A., Peyre, P., Vannes, A.B., Peix, G. (2003). Reduction of porosity content generated during Nd:YAG laser welding of A356 and AA5083 aluminium alloys. *Mater. Sci. Eng., A.*, **363**: 40-52.

Hwang, L.-R., Gung, C.-H. & Shih, T.-S. (2001). A study on the qualities of GTA-welded squeeze-cast A356 alloy. *J. Mater. Process. Technol.*, **116**: 101-113.

Jha, A.K., Murty, S.V.S.N., Diwakar, V. & Sree Kumar K. (2003). Metallurgical analysis of cracking in weldment of propellant tank. *Eng. Failure Anal.*, **10**: 265-273.

Kou, S. (2003). *Welding Metallurgy, 2nd Ed.*. John Wiley & Sons, Inc., Hoboken, New Jersey.

Kuk, J.M., Jang, K. C., Lee, D, G. & Kim, I. S. (2004). Effects of temperature and sheilding gas mixture on fatigue life of 5083 aluminium alloy. *J. Mater. Process. Technol.*, **155-156**: 1408-1414.

Kumar, A. & Sundarrajan, S. (2009). Effect of welding parameters on mechanical properties and optimization of pulsed TIG welding of Al-Mg-Si alloy. *Int. J. Adv. Manuf. Technol.*, **42**: 118 – 125.

Lakshminarayanan, A.K., Balasubramanian, V. & Elangovan, K. (2009). Effect of welding process on tensile properties of AA6061 aluminium alloy joints. *Int. J. Adv. Manuf. Technol.*, **40**: 286-296.

Maggiolino, S. & Schmid, C. (2008). Corrosion resistance in FSW and in MIG welding techniques of AA6xxx. *J. Mater. Process. Technol.*, **197**: 237- 240.

Punkari, A., Weckman, D.C. & Kerr, H. W. (2003). Effects of magnesium content on dual beam Nd.YAG laser welding of Al-Mg alloys. *Sci. Technol. Weld. Joining*, **8**: 269 – 281.

Raghu Babu, G., Murti, K. G. K. & Ranga Janardhana, G. (2008). An experimental study on the effect of welding parameter on mechanical and microstructural properties of AA 6082-T6 friction stir. *J. Engineering Appl Sci.*, **3**: 68-74.

Robert, W. & Messler, Jr. (1999). *Principles of Welding Processes, Physics, Chemistry, and Metallurgy*. John Wiley & Sons, Inc., Canada.

Roy, N., Zhang, L., Louchez, P.R. & Samuel, F. H. (1996). Porosity formation in Al-9wt%Si-3wt% Cu-X alloy systems: measurements of porosity. *J. Mater. Sci.*, **31**: 1243-1254.

Othman, N.K., Bakar, S.R.S., Jalar,A., Syarif,J. &Ahmad, M.Y., 2010. The effect of filler metals on mechanical properties of 6 mm AA 6061-T6 welded joints. *Adv. Mater. Res.*, **154-155**: 873-876.

SPECTRAL CONSTANCY ON HYPERSPECTRAL IMAGERIES

Izzati Ibrahim, Peter Yuen*, Aristeidis Tsitiridis, Kan Hong, Tong Chen, Umair Soori, James Jackman, David James & Mark Richardson

Department of Informatics & Sensor, Cranfield University, Defence College of Management & Technology, UK

*E-mail: p.yuen@cranfield.ac.uk

ABSTRACT

This paper concerns how the intrinsic electro-optical (EO) property, particularly the reflectance of objects in the scene, can be better estimated from hyperspectral imagery in attempt to minimise illumination artefacts. This is termed as spectral constancy, and the objective of the research is to derive a method to compensate the illumination artefacts, specifically shadows, so to improve object recognition and classification accuracy performance. One contribution of this work is the establishment of a new method, known as Diffused Irradiance Compensation (DIC), for shadow mitigations via the estimation of the directed and diffused irradiance of the scene.

Keywords: *Hyperspectral; illumination independent; shadow; spectral constancy.*

1. INTRODUCTION

Hyperspectral imaging system (HSI) is a spectral sensing technique which employs hundreds or more of contiguous waveband images in the visible and infrared regions of the electromagnetic spectrum as illustrated in Figure 1 (Yuen *et al*., 2010). Each waveband occupies a very narrow slice of the electromagnetic (EM) spectrum of approximately 5-20 nm wide, allowing the analysis to be performed on each individual waveband or a subset of them to maximise the contrast between the target and the clutter background. Each recorded pixel in each waveband contains a sampled spectrum, known as a spectral signature, or in some cases, the reflectance, which can be used to identify or discriminate materials in a scene. For instance, HSI is able to distinguish targets that appear to be of the same colour by exploiting slices of spectral information in a wide region as illustrated in Figure 2. Other conventional imaging systems, such as broadband conventional digital RGB imaging, would have difficulties discriminating these 'look-alike' targets. However, as HSI is capable of capturing a more detailed spectral signature of the targets, allowing it to be deployed in many applications such as for surveillance with performances far more superior than any other imaging technologies.

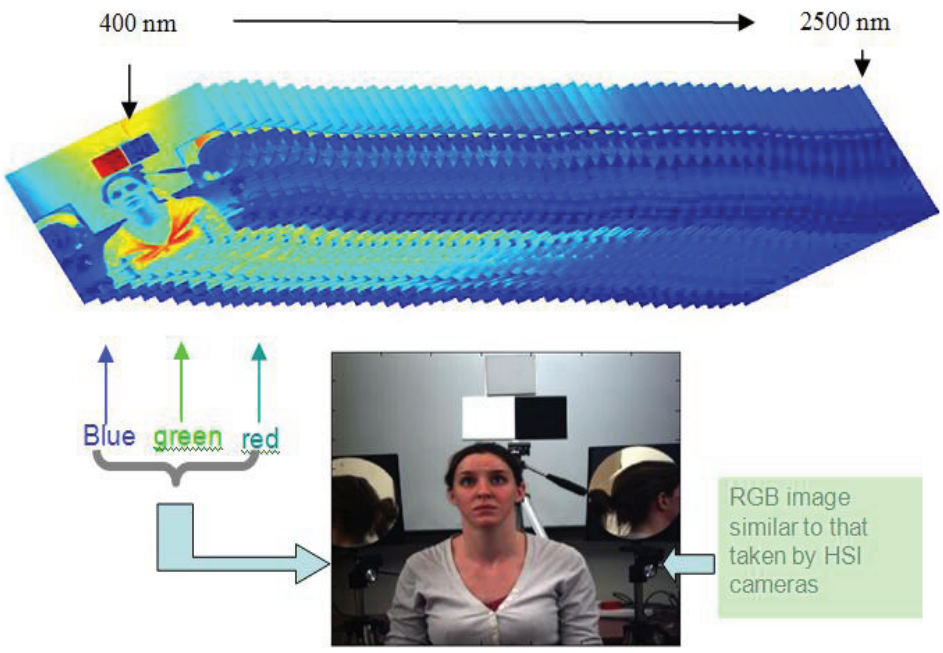

Figure 1: The concept of hyperspectral imaging (HSI) that records many contiguous narrow-wavebands images instead of only three broad bands of red, green and blue as in conventional imaging system.

The ultimate usefulness of this technology relies very much on whether the reflectance of the objects in the scene can be accurately retrieved from the image through the HSI system. However, many environmental and imaging issues can make the extraction of target reflectance spectra from imaging data complicated. For example, the solar energy that reaches the ground can be modulated due to atmospheric effects such as scattering and absorption, although the solar irradiance in the exoatmosphere is well characterised. Scattering and absorption by gases and particles in the atmosphere present significant considerations in imaging as they are the predominant factors responding for the wavelength dependent transmission of light to the sensor (Kruse *et al.*, 1990). Such modulations effects must be accounted for, in order to accurately recover the target reflectance of objects on the ground.

In normal circumstances when a flat landscape of the scenery is uniformly illuminated at or near to the normal plane of the surface, the reflectance of the objects in the scene can be deduced rather accurately if the atmosphere parameters are known. In practise this is not always the case due to self-shadowing cast by nearby objects contained within the scene. Shadow induces distorted reflectance interpretation of target. Early studies (Ajtay *et al.,* 1979; Verstraete *et al.,* 1991) have shown that shadow cast by cloud affects the accuracy of vegetation reflectance estimation by increasing the visible reflectance and thus reducing the Normalized Difference Vegetation Index (NDVI) estimates of vegetation (Simpson *et al.,* 1998).

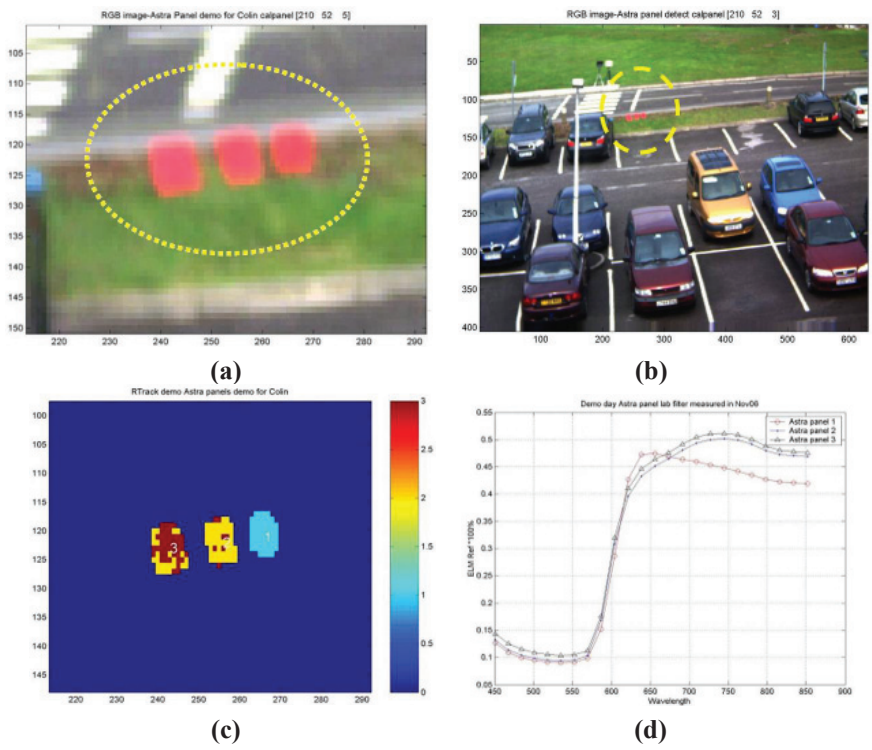

Figure 2: (a) RGB image; (b) location; (c) classification map; and (d) spectra of three look-alike red Astra car panels in the visible-near infrared (VNIR) spectral waveband. The hyperspectral imaging system is able to distinguish the three different panels by exploiting more detailed spectral information other than the RGB bands.

Hyperspectral imaging senses the reflected EM energy which consists of the direct irradiance (solar beam) and diffuse irradiance (reflected skylight irradiance) from objects on the ground. When the solar beam is blocked by objects casting shadows, the energy of the directed solar is reduced but the diffuse irradiance remains relatively constant as illustrated in Figure 3. Hence it is important to estimate the fractions of the direct E_{direct} and also the diffuse irradiance $E_{diffuse}$ for every pixel in the image in order to retrieve the intrinsic optical properties of the scene.

Objects under shadows may exhibit misleading electro-optical (EO) responses dependent on the background of the scene as well as the illumination conditions as illustrated in Figures 4 and 5. For outdoor scenes, where solar irradiance and skylight are the only sources of illumination, it is noted that the shadowed objects exhibit a higher proportion of 'apparent' radiance in the blue region (400 ~ 550 nm), as shown in Figure 4, compared to the same objects that are under directed solar irradiance. The scattering of light by the particles and air molecules in the atmosphere is most efficient in the vicinity of the blue region. This is due to the Rayleigh scattering effect of the solar irradiance by the atmosphere that is inversely proportional to the fourth power of the wavelength. As the blue wavebands have shorter wavelengths, they are scattered more efficiently in comparison to the longer wavelenghts, effectively causing a higher proportion of the blue spectrum in the diffused irradiance which is subsequently sensed from objects in the shadows.

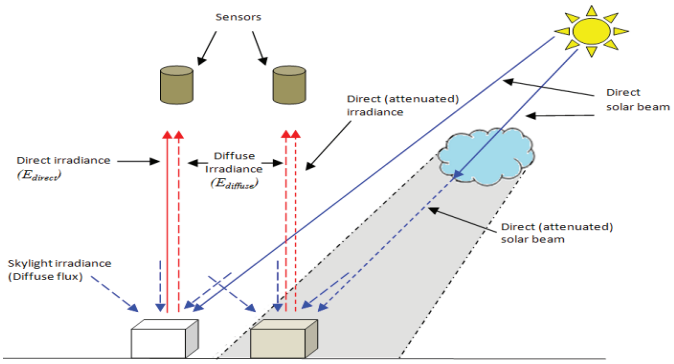

Figure 3: The sketch of cloud shadow geometry.

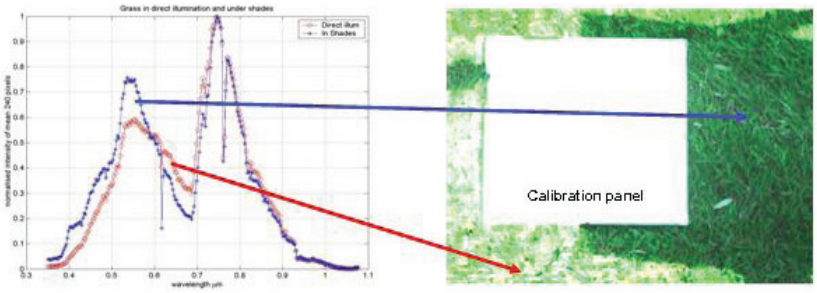

Figure 4: Spectral properties of the lawn under direct and sky light illuminations in an outdoor scenario. Note that the apparent reflectance of the shadowed target exhibits a slightly higher degree of 'blue' portion due to the higher proportion of blue spectrum in the diffused sky light irradiance of the shadow.

However, the situation is seen quite differently for the indoor scenarios where a higher radiance in the long wavelengths is sensed for objects in the shadows when they are in the indoor environment (see Figure 5). This observation may be due to the fact that the longer wavelengths in the near infrared (NIR) region is more efficiently scattered than the shorter ones, inducing a higher proportion of NIR energy in the diffused irradiance for the indoor case.

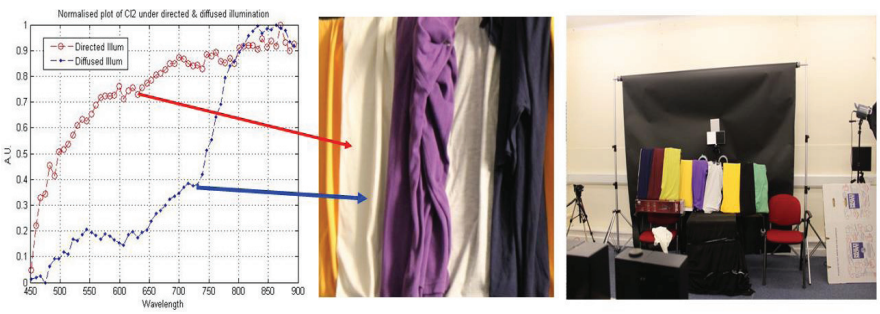

Figure 5: 'Apparent' spectral property of objects under directed (red) and diffused (blue) illumination as seen from an indoor HSI image. Note that the shadow pixels (blue) are affected very differently in comparison to the outdoor case (see Figure 4).

Any models that attempt to compensate for shadows must involve the spherical albedo of the surrounding as well as knowledge of the spectral density of the illumination source. This is hard to achieve in practice, particularly when only a single shot of image is taken under one illumination condition for the data processing. Modelling of the diffuse irradiance in the indoor case can be readily achieved when a priori knowledge of the environment is available.

The purpose of this paper is to outline some of the most common methods for compensating illumination artefacts, particularly shadows in HSI. Subsequently a method based upon the estimation of the spectral densities of the directed and diffused irradiances for shadow compensation is proposed.

2. ATMOSPHERIC COMPENSATION (AC): AN OVERVIEW

Atmospheric compensation (AC) aims to compensate the effects of atmospheric absorption and scattering as well as illumination angle artefacts on hyperspectral imageries by converting the radiance at the sensor to the reflectance of the target surface (West, 2005). It is important to compensate the atmospheric scatterings and absorption, as well as illumination artefact, for a more accurate data interpretation. Earlier studies have shown that AC can enhance target detection and classification in hyperspectral remote sensing (Yuen, 2004; Yuen & Bishop, 2004; Yuen *et al.,* 2004). Methods for AC can be roughly divided into two main categories (Ben-Dor & Levin, 2000):

i. Those that rely on ground data measurements taken during the experiment and
ii. Those that rely on data themselves, where no prior information of the atmosphere or surface condition is available.

Category 1 involves either atmospheric modelling or surface measurements. The Atmospheric Removal Program (ATREM) (Gao *et al.* 1993) and Atmospheric Correction Modelling (ATCOR) (Richter, 2005) are examples for the former, while the Empirical Line Method (ELM) (Roberts *et al.,* 1985, Kruse *et al.,* 1990) is for the surface measurements. The Internal Average Relative Reflectance (IARR) (Kruse, 1988) and the Flat Field (FF) method (Rast *et al*., 1991) are examples for Category 2.

2.1 ATCOR Overview

ATCOR is based on Equation 1 which employs a database of radiative transfer calculation using MODTRAN (Richter, 2005; Asras, 1989) to estimate the wavelength dependent transmissions of solar energy in various types atmospheric conditions. The at-sensor radiance L based on a flat-surface condition is given as (Richter & Muller, 2005):

$$L = L_p(\theta_v, \theta_s, \varphi) + \tau_v(\theta_v)\frac{\rho}{\pi}\frac{E_g(0)}{(1-\rho_r s)} \qquad (1)$$

where

L = at-sensor radiance for surface reflectance ρ

L_p = path radiance

$\theta_v, \theta_s, \varphi$ = view zenith, solar zenith and relative azimuth angle respectively

τ_v = total ground-to-sensor atmospheric transmittance, sum of direct τ_{direct} and diffuse $\tau_{diffuse}$ transmittance;

ρ = surface reflectance

π = 3.142 or $\frac{22}{7}$

E_g = global flux on a horizontal surface, sum of direct (E_{direct}) and diffuse ($E_{diffuse}$) flux, $E_g(0)$ is calculated for a ground surface with $\rho = 0$;

ρ_r = large scale reference background reflectance determining the effective global flux ($\rho_r = 0.15$ is used in ATCOR)

s = spherical albedo of the atmosphere, accounts for atmospheric backscaterring to the ground

Then, with the assumption of full solar illumination, the surface reflectance can be calculated using the following equation:

$$\rho = \frac{\pi\{d^2(c_o + c_1 DN) - L_{path}\}}{\tau(E_{direct} + E_{diffuse})} \quad (2)$$

where *DN* denotes digital numbers, *d* is the Earth-sun distance at the image acquisition time in astronomical units and c_o and c_1 are the radiometric calibration coefficients (offset and slope) to convert the digital number into the corresponding at sensor-radiance. To measure the c_o and c_1, two areas of the lowest and darkest albedo is identified on the scene. Given by the mean spectra from both areas, a linear regression is calculated to solve for gain and offset factors according to the Equation 2. In clear sky situations and for short range operations (<1 km range), the path radiance L_p may be small and therefore the estimation of L will be totally dependent on the E_g.

3. PREVIOUS WORK ON SHADOW COMPENSATION

Several methods have been developed for correcting the shadow regions in HSI systems. One of the methods is by utilising covariance matrix and zero-reflectance matched filter vector to identify the shadow areas in hyperspectral imagery (Richter & Muller, 2005). This method has been employed within ATCOR. The shadows are corrected using the 'unscaled shadow function' obtained from matched filtering which is then rescaled using the function's histogram to obtain a 'scaled shadow function' ranging from 0 to 1, where 0 indicates full shadow and 1 indicates full direct illumination. A shadow mask is established by thresholding the unscaled shadow function, and the shadow compensation will involve pixels surrounding shadows / clear transition zone.

This method results in smooth transitions between shadow and clear zone. As this method relies on the spectral measurement, it exhibits fast processing time and hence, it provides the possibility to be implemented in real-time applications. However, there are some restrictions on the implementations of this method as it is applicable only for the outdoor environments where cloud covers are less than 25%. Therefore, it may be more suitable for satellite or airborne HSI. Other works that employ the matched filter concept have also been reported (Richter & Muller, 2005) but with different techniques on the rescaling algorithm. Note that this method requires information in the short wave infrared (SWIR) region.

Another similar approach has been proposed by implementing a threshold based on the energy of each pixel for the establishment of the shadow mask. The reflectance is then calculated separately for full sunlight and in shadow using a reflectance equation based on a simplified radiometric transfer function (Banerjee *et al*., 2009). These authors have achieved an illumination-invariant motion detection and object tracking by using real hyperspectral video. However, the practicality of this method has been limited due to the need of the object undergoes illuminations by both directed and diffused irradiances co-exist in at least one of the video frames.

4. DIFFUSE IRRADIANCE COMPENSATION (DIC)

Most of the HSI reported work has assumed illuminations of the scene by directed irradiance. The irradiance due to diffused and multiple scattering by the background and environment of the scene have been largely ignored. This leads to errors in the estimation of the reflectance in the shadowed pixels, because the E_g has been assumed to be primarily due to direct irradiance only as shown in Equation 2. This results in a lower value in the 'apparent' reflectance estimation than that of the same target when it is truly under illumination by direct irradiance. Consequently, the same target will be classified into two different classes, heavily misleading the classification result.

The purpose of this work is to develop a method to compensate the shadow effect for indoor HSI scenarios requiring minimum information about the environment. The proposed method can be used when there is a lack of information in the SWIR region. In this paper, a method known as Diffused Irradiance Compensation (DIC) (Ibrahim *et al.,* 2010) is proposed based upon the methodology utilised by Richter & Muller (2005), with a slightly modified shadow masking and compensation mechanism. In this work, the spectral density of the diffused and directed irradiance E_g (E_{direct} +$E_{diffuse}$) are characterised via a separate experiment and it is then applied for the pixels in the shadow mask.

4.1 Low Reflectance and Shadow Mask

The reflectance of targets under shadow is hard to estimate due to the weak reflected signal. Most targets in shadow areas exhibit small non zero signal as the result of illuminations solely due to the relatively weak and diffused irradiance.

Since shadowed pixels exhibit low reflected DN, it is necessary to differentiate the shadowed pixels from the low reflectance objects, such as dark coloured objects, which are illuminated by direct irradiance within the scene. In both cases, the DN of these pixels are very small, but it is the shadowed pixels and not the low reflectance objects that are need to be corrected. In order to differentiate them, two different masks, spectral variance and the spectral means, have been utilised for the discrimination between the low reflectance from the shadowed pixels. This final shadow mask is shown in Figure 6. This region is employed for shadow compensation using the DIC method.

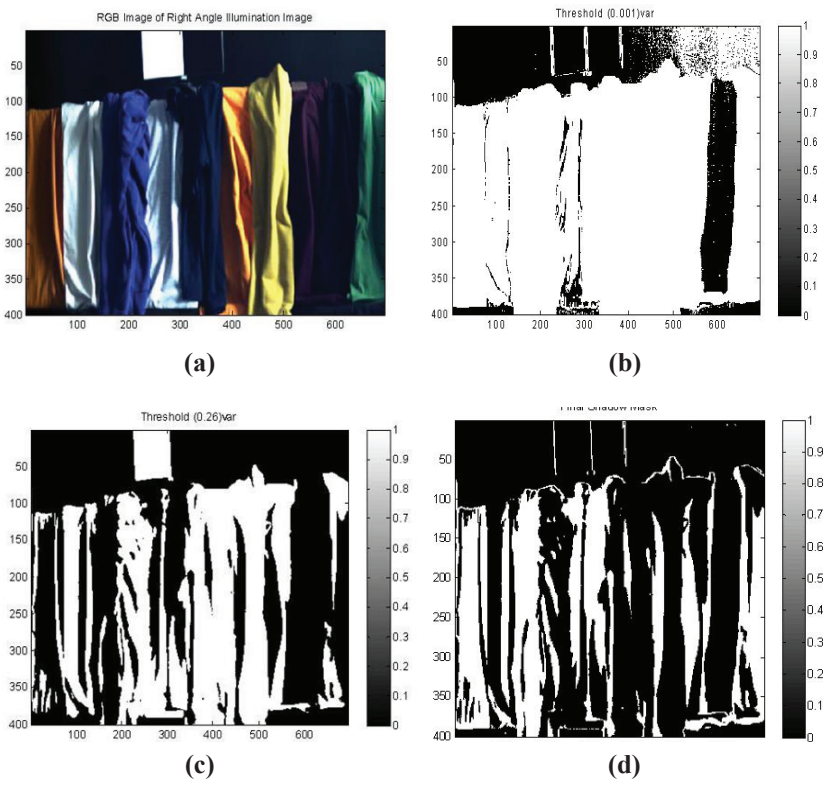

Figure 6: The procedure for obtaining the final shadow mask: (a) The RGB image under oblique illumination; (b) The threshold (0.001) of the variance values of the image which represents the flat reflectance target; (c) Threshold (0.26) of the spectral mean of the image which represents the low reflectance pixels in the scene; and (d) The final shadow mask (bright areas) after the flat reflectance pixels are removed.

4.2 Diffuse and Direct Irradiance Estimation

Upon the establishment of the final shadow mask of the scene, the illumination artefacts in HSI can be partially compensated through an estimation of the directed and diffused irradiance in the following manner:

i. For targets in the shadow area, the DN values are ratioed by the diffused irradiance estimated from the shadowed part of the white spectralon as illustrated in Figure 7.
ii. For targets that are directly illuminated, their DN values are ratioed by the directed irradiance obtained from the directly illuminated part of the white spectralon.

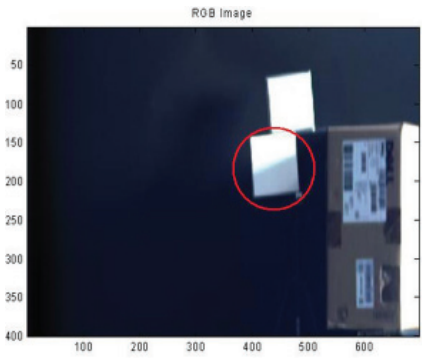

(a)

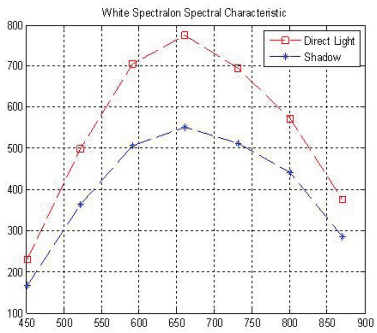

(b)

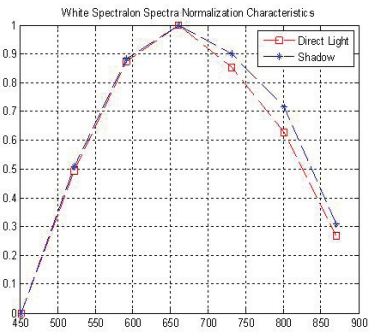

(c)

Figure 7: Estimation of E_{direct} and $E_{diffuse}$: (a) RGB image of the experimental set; (b) Spectral characteristics of E_{direct} and $E_{diffuse}$ in DN values; and (c) Difference in the spectral characteristics E_{direct} and $E_{diffuse}$.

The white spectralon employed in this experiment is used to measure the spectral density of the illumination sources of the scene. As shown in Figure 7, it illustrates the experiment for assessing the E_{direct} and $E_{diffuse}$ under the same illumination condition as that shown in Figure 6. The assessment is performed to characterise the multiple scattering of the environment prior to the collection of the shadow data as depicted in Figure 6.

5. HYPERSPECTRAL RESULTS

A hyperspectral data set of 10 different coloured T-shirts was captured using a Headwall VNIR HSI system within spectral bands of 400 o 1000 nm. An RGB image of the raw data is shown in Figure 8, which was collected under oblique illuminations of halogen lamps within a laboratory of predominantly white and yellow background at a range of ~4 m. The self-shadow cast by the oblique illumination have been formed in these targets. The objective of this experiment is to examine the ability of the proposed DIC method for retrieving the intrinsic reflectance of the targets under shade and the results will be compared with that under directed illuminations. The effectiveness of the DIC approach was examined alongside with the conventional AC method which ignores $E_{diffuse}$ in Equation 2.

Figure 8: The set up of the shadow compensation experiment under oblique illumination, inducing shadow cast on part of the targets. The T-shirts classes are labelled from 1 to 10, from left to right. At the top of the targets are 3 standard panels (spectralon) for calibration purpose.

The RGB images after the conventional AC and DIC correction are given in Figure 9(a) and 9(b) respectively. Sample spectra extracted from the regions under directed and diffused illumination in class 1 (yellow T-shirt) and 10 (green T-shirt) are presented in Figure 9(c) and Figure 9(d). Note the large differences in the 'apparent' reflectance for the directly illuminated and the shaded regions of the same target. It is seen in these figures that the proposed shadow compensation algorithm has reduced the illumination artefact rather substantially, particularly in target 10 where the intrinsic reflectance of the shadowed region can be retrieved using the proposed method. This result may also suggest that further improvement of the method is needed for a more robust performance of the algorithm.

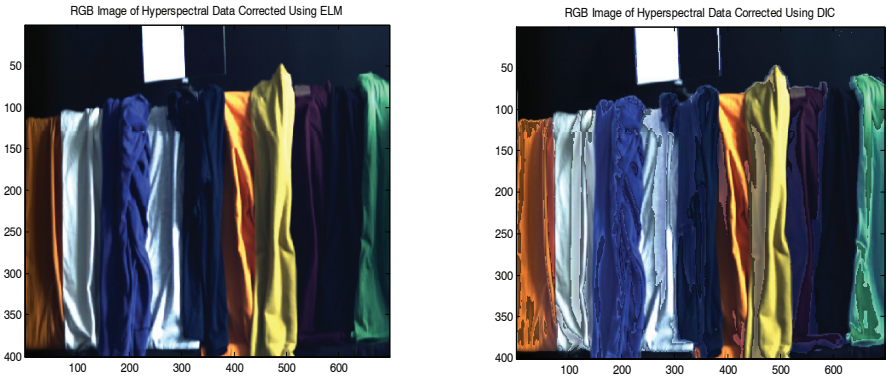

(a) **(b)**

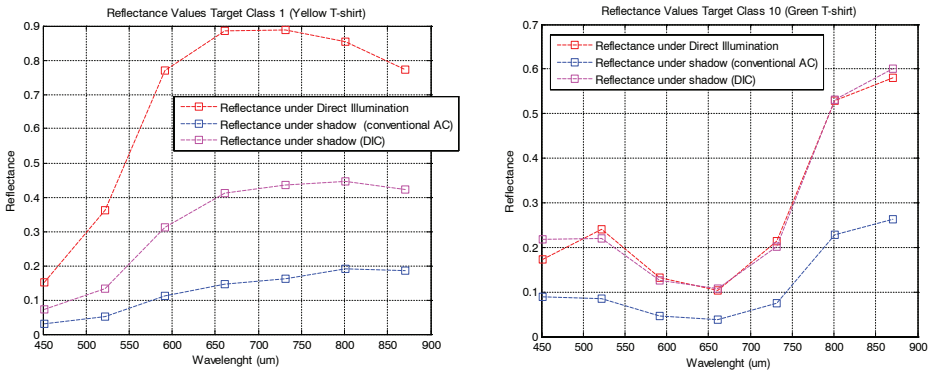

(c) **(d)**

Figure 9: RGB image of the hyperspectral data corrected using (a) Conventional AC and (b) DIC. (c) Reflectance values of target class 1 (white t-shirt). Note the enhancement of reflectance of target under shadow using the proposed shadow compensation technique. (d) Reflectance values of target class 10 (green t-shirt). The reflectance of target under shadow (using DIC) is almost consistent with the reflectance of target under direct illumination.

6. CONCLUSION

We have presented a DIC method for the compensation of shadow effects in HSI. The method involves the characterisation of spectral densities of the directed and diffused irradiance of the environment, and they are then applied to a shadow mask of the image for estimating the intrinsic reflectance of objects in the scene. The result has shown some success for the retrieval of the intrinsic reflectance but further improvement is needed for a more robust performance.

ACKNOWLEDGEMENTS

The authors would like to thank Malaysian Ministry of Science & Technology (MOSTI) for the scholarship to make this project possible. The second author would like to thank Drs C Lewis, R Bower & R Botton of the CPNI for the interest and partial support of this work. AT would like to thank EPSRC for the provision of DTA grant, and TC & KH would like to thank the DCMT internal funding for the provisions of studentships.

REFERENCES

Ajtay, G.L., Ketner, P., & Duvingeaud, P. (1982). *Terretrial Primary Production and Pytomass in the Global Carnon Cycle*. Wiley, New York.

Asrar, G. (1989). *Theory and Applications of Optical Remote Sensing*. Wiley, New York.

Banerjee, A., Burlina, P. & Broadwater, J. (2009). Hyperspectral video for illumination-invariant tracking. *Proceedings of First Workshop on Hyperspectral Image and Signal Processing: Evolution in Remote Sensing*, 1-3.

Ben-Dor, E. & Levin, N. (2000). Determination of surface reflectance from raw hyperspectral data without simultaneous ground data measurements: a case study of the GER 63-channel

sensor data acquired over Naan, Israel. *Int. J. Remote Sens.,* **21:** 2053-2074.

Gao, B. C., Heidelbrecht, K. B. & Geotz, A. F. H. (1993). Derivation of scaled surface reflectance from AVIRIS data. *Remote Sens. Environ.,* **44**, 165-178.

Ibrahim, I., Yuen, P., Tsitiridis, A., Hong, K., Chen, T., Jackman, J., James, D & Richardson, M. (2010). Illumination independent object recognition in hyperspectral imaging. *SPIE Proceeding: Defence, Security & Sensing, Toulouse, France.*, **7838**: 78380Q-1-12.

Kruse, F. A. (2011). *Imaging spectrometer data analysis – A Tutorial*. Available online at: http://www.hgimaging.com/PDF/Kruse_isssr94tut.pdf (Last access date: 3 March 2011)

Kruse, F. A. (1988). Use of airborne imaging spectrometer data to map minerals associated with hyfrothermally altered rocks in the northern Grapenvine Mountains, Nevada and California. *Remote Sens. Environ.*, **24**, 31-51.

Kruse, F. A., Kieren-Young, K.S. & Boardman, J. W. (1990). Mineral mapping at Cuperite, Nevada with 63 channel imaging spectroradiometer. *Photogramm. Eng. Remote Sen.*, **56**, 83-92.

Rast, M., Hook, S. J., Elvidge, C.D. & Alley, R. C. (1991). An evaluation of techniques for the extraction of mineral absorption features from high spectral resolution remote sensing data. *Photogramm. Eng. Remote Sen.*, **57**, 1303-1309.

Richter, R. (2005). *Atmospheric/Topographic Correction for Satellite Imagery* (ATCOR-2/3 User Guide). German Aerospace Center, German.

Richter, R. & Muller, A. (2005). De-shadowing of satellite/airborne imagery. *Int. J. Remote Sens.*, **26:** 3137-3148.

Roberts, D.A., Yamaguchi, Y. & Lyon, R.J.P. (1985). Calibration of airborne imaging spectrometer data to percent reflectance using field spectral measurements. *Proceedings of the Nineteenth International Symposium on Remote Sensing Environment, Ann Arbor, Michigan, 21-25 October 1985,* ERIM, Ann Arbor, MI, 679-688.

Simpson, J.J & Stitt, R.S. (1998). A procedure for the detection and removal of cloud shadow form AVHRR data over land. *IEEE T Geosci. Remote Sens.,* **36**: 880-896.

Yuen, P. (2004). Atmospheric correction preprocessing for hyperspectral target detection. *DTC EMRS Report No.: EMRC-HAD-03*.

Yuen, P. & Bishop, G. (2004). Enhancements of target detection using atmospheric correction preprocessing techniques in hyperspectral remote sensing. *SPIE Proceeding: Military Remote Sensing, London*, **5613**: 111-118.

Yuen, P., Killey, A., Hobson, S. & Bishop, G. (2004). Atmospheric correction preprocessing techniques in Hyperspectral remote sensing. *1st EMRS DTC Conference, Edinburgh*, **B15**.

Yuen, P.W.T. & Richardson, M. (2010). An introduction to hyperspectral imaging and its application for security, surveillance and target acquisition. *Imag. Sci. J.*, **58**: 241-253.

EVALUATION OF OPERATING BANDWIDTH AND POWER LEVEL THRESHOLD OF RF DETECTORS

Dinesh Sathyamoorthy*, Mohd Faudzi Muhammad, Mohd Idris Ishak, Shalini Shafii, Jamilah Jaafar, Aliah Ismail, Zainal Fitry M. Amin, Siti Zainun Ali & Mohd Hasrol Hisam M Yusoff

Instrumentation and Electronics Technology Division (BTIE), Science & Technology Research Institute for Defence (STRIDE), Ministry of Defence, Malaysia

*E-mail: dinesh.sathyamoorthy@stride.gov.my

ABSTRACT

In December 2010 to February 2011, the Instrumentation & Electronics Technology Division (BTIE) conducted a series of tests to measure the operating bandwidth and power level threshold of two RF detectors; HomeSafe (model 790) and Ghost (model CT-AS0039). It was determined that the Ghost RF detector's Channel A has the largest operating bandwidth (0.3 MHz to 4.84 GHz), followed by its Channel B (0.4 MHz to 4.35 GHz), while the HomeSafe RF detector has the smallest operating bandwidth (91 MHz to 3.88 GHz). The HomeSafe RF detector has the lowest power level thresholds for the frequency range of approximately 0.7 to 2.9 GHz, while the Ghost RF detector's Channel A has the lowest power thresholds for the remaining tested frequencies. The Ghost RF detector's Channel A also generally has the most stable power level thresholds over the frequencies. Based on the results obtained, the Ghost RF detector is more suitable for detection of wireless spy devices as it can allow for the detection of a wider range of signal frequencies. In addition, its two power level threshold channels, Channel A with lower power level threshold for detection of low power level signals, and Channel B with higher power level threshold to avoid false alarms, allows the user to sweep the suspected area using Channel A, and then, hone in on the target using Channel B.

Keywords: *RF detector; maximum and minimum operating frequencies; operating bandwidth; power level threshold; signal detection.*

1. INTRODUCTION

Radio frequency (RF) detectors are used to detect RF signals transmitted in given proximities. They are generally used to detect transmissions from wireless spy devices, such as listening bugs or cameras, hidden in objects or covertly placed in rooms (hence the nickname "bug detector"). An RF detector is usually able to sweep a room or area for bugs and warn the user about active RF transmitters (Peterson, 2001; Savry & Vacherand, 2010). In Malaysia, there has been a proliferation of purchases of such equipment, especially in the aftermath of a particular high profile sex video scandal that occurred in January 2008 (Cruez, 2008; Siew & Yuen-C, 2008). In addition, RF detectors provide important protection to pacemaker users (Pinski & Trohman, 2002a, b; Patel *et al.*, 2007; Seidman *et al.*, 2010), and to those who work in the presence of RF or microwave hazards (USN, 1997; Curtis, 2003; MOL, 2009).

The performance of RF detectors is dependent on two key parameters; operating bandwidth and power level threshold. A number of wireless spy devices are designed to transmit signals with low power levels in order to avoid detection (Peterson, 2001; Davis, 2004). An RF detector

with low power level threshold is required for detection of such devices. However, if the detector has a power level threshold that is too low, it could cause false alarms, such as from handphones or Bluetooth devices. In addition, RF detectors with larger operating bandwidths allow for the detection of a wider range of transmitted signal frequencies (Peterson, 2001; Savry & Vacherand, 2010).

In December 2010 to February 2011, the Instrumentation & Electronics Technology Division (BTIE) conducted a series of tests to measure the operating bandwidths and power level thresholds of two RF detectors (Figure 1) (STRIDE, 2010, 2011a-d):

i. HomeSafe (model 790) (Lelux, 2008).
ii. Ghost (model CT-AS0039) (Satcus, 2010).

(a) **(b)**

Figure 1: The RF detectors evaluated in this study: (a) HomeSafe (model 790); and (b) Ghost (model CT-AS0039).

Based on the provided specifications of the respective devices, the operating bandwidth of the HomeSafe RF detector is 20 MHz to 3 GHz, and 100 MHz to 2.6 GHz for the Ghost RF detector. The HomeSafe RF detector has only one power level threshold channel, while the Ghost RF detector has two channels (Channels A and B, with higher and lower power thresholds respectively). The power level thresholds for both devices are not provided in the respective specifications.

It should be noted that both RF detectors are not high precision meters. The power level thresholds for both RF detectors are not fixed for the respective devices' operating bandwidths, but rather vary with frequency. This paper is aimed at discussing the procedures employed in the conducted tests, and the findings obtained.

2. METHODOLOGY

The apparatus used in the tests were an Advantest U3751 spectrum analyser (Advantest, 2009), a HP 83620B signal generator (Hewlett Packard, 1998), an Aeroflex-IFR 2026B signal generator (Aeroflex, 2005), a Hyperlog 60180 directional antenna (Aaronia, 2009), and a Diamond RH799 omnidirectional antenna (Diamond, 2010). The test setup is as shown in Figure 2. All the tests were conducted in the STRIDE Radar Lab (Figure 3).

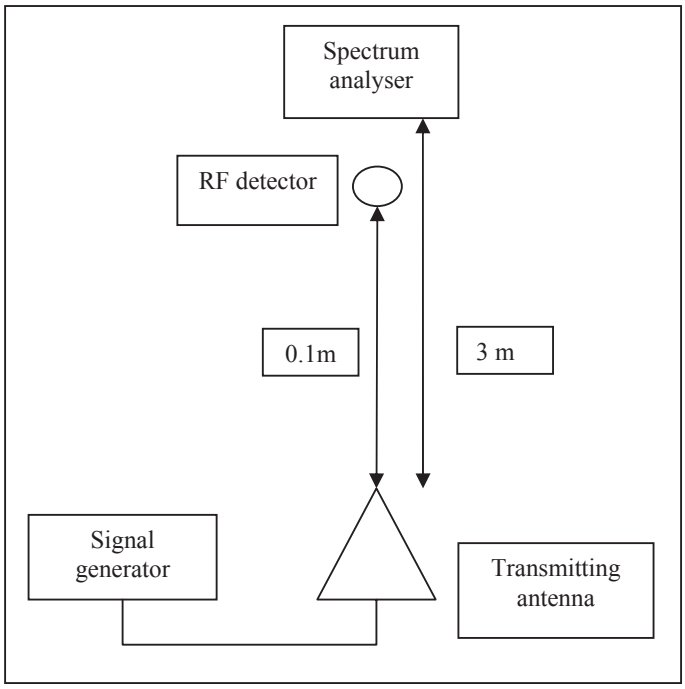

Figure 2: The test setup.

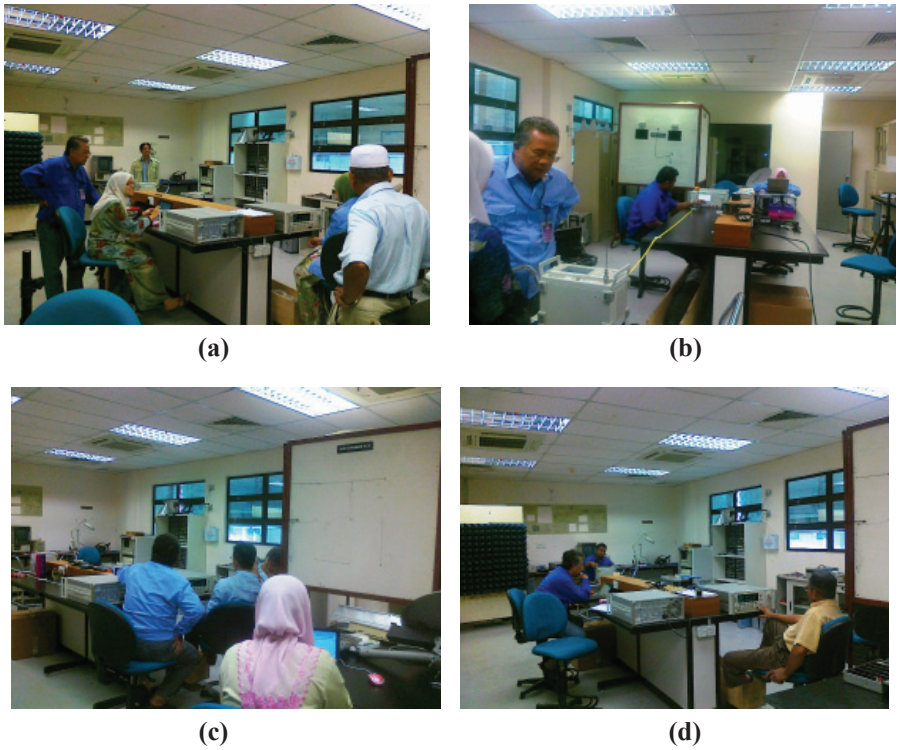

(a) **(b)**

(c) **(d)**

Figure 3: BTIE officers and staff conducting the tests in the STRIDE Radar Lab.

The spectrum analyser is placed 3 m away from the transmitting antenna to avoid damage from power levels that are too high. The computation of the received power levels at the location of the RF detector is performed as in the appendix. For transmissions below 700 MHz, the Diamond antenna is used, while for transmissions of 700 MHz and above, the Hyperlog antenna is used. For transmissions below 10 MHz, the IFR 2026B signal generator is used, while for transmissions of 10 MHz and above, the HP 82620B signal generator is used. For the Ghost RF detector, the tests are conducted for both Channels A and B.

In order to determine the minimum operating frequencies of each RF detector, transmission is set at power level of 24 dBm and frequency of 0.1 MHz. The frequency is increased incrementally by 0.1 MHz until the signal is detected. The received power level at this point is recorded. These steps are repeated for transmission power levels of 23 to -20 dBm (decrements of 1 dBm). In order to determine the maximum operating frequencies of each RF detector, the procedure is repeated, with the starting transmission frequency set at 6 GHz, and the frequency being decreased decrementally by 0.1 MHz until signal detection.

In order to determine the power level threshold of each RF detector, transmission is set at power level of -30 dBm and frequency of 20 MHz. The power level is increased incrementally by 0.1 dBm until the signal is detected. The received power level at this point is recorded. The procedure is repeated for transmission frequencies of 40 to 100 MHz (increments of 20 MHz) and 200 MHz to 6 GHz (increments of 100 MHz).

3. RESULTS & DISCUSSION

The measured minimum and maximum operating frequencies of the RF detectors over the tested power levels are as shown in Figures 4 and 5 respectively. The maximum operating frequency increases with power level, and vice-versa for the minimum operating frequency. All the plots have linear regressions with high coefficients of determination R^2, indicating that the variances of these parameters are largely due to the variance of power level, rather than from other factors.The errors in the goodness of fit plots were caused by detector oscillator instability.

The operating bandwidths of the RF detectors, determined based on minimum and maximum operating frequencies at the highest power levels at which stability in the plots was achieved, are as shown in Table 1. While there are tested power levels that have lower minimum operating frequencies, this is due to the detector oscillator instability. It is observed that the Ghost RF detector (Channel A) has the largest operating bandwidth, followed by its Channel B and the HomeSafe RF detector.

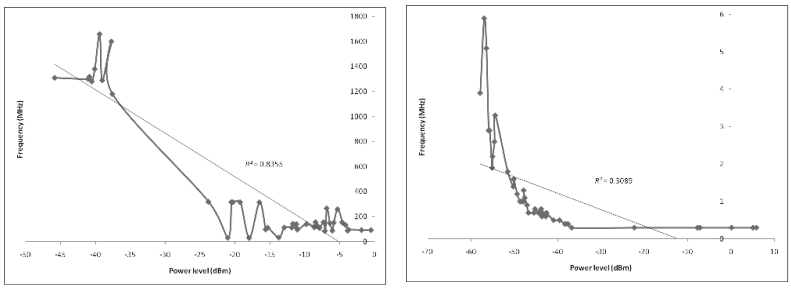

(a) **(b)**

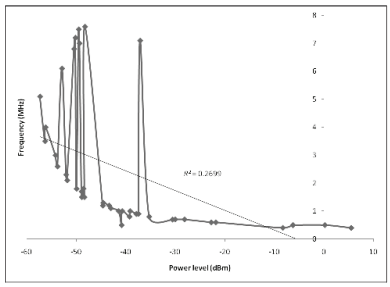

(c)

Figure 4: Minimum operating frequencies of the evaluated RF detectors: (a) HomeSafe (model 790) ; (b) CT-AS0039 Ghost (Channel A); and (c) CT-AS0039 Ghost (Channel B).

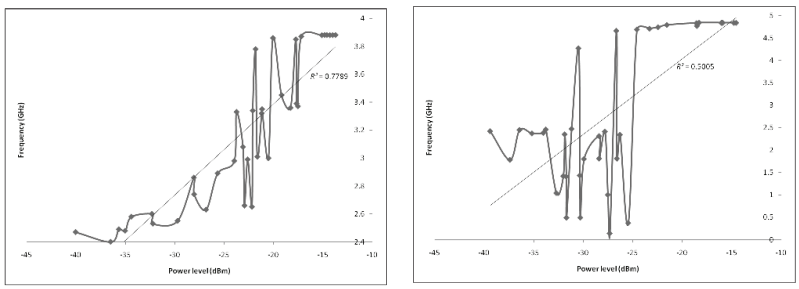

(a) **(b)**

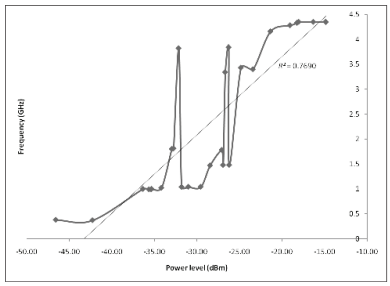

(c)

Figure 5: Maximum operating frequencies of the evaluated RF detectors: (a) HomeSafe (model 790); (b) CT-AS0039 Ghost (Channel A); and (c) CT-AS0039 Ghost (Channel B).

Table 1: Measured operating bandwidths of the evaluated RF detectors.

RF Detector	*Operating Bandwidth*
HomeSafe (model 790)	91 MHz - 3.88 GHz
Ghost (model CT-AS0039): Channel A	0.3 MHz - 4.84 GHz
Ghost (model CT-AS0039): Channel B	0.4 MHz - 4.35 GHz

Based on the plots in Figure 6, it is observed that the evaluated RF detectors have varying power level threshold performances over frequency. The HomeSafe RF detector has the lowest power level threshold for the frequency range of approximately 0.7 to 2.9 GHz, while the Ghost RF detector's Channel A has the lowest power thresholds for the remaining frequencies. The Ghost RF detector's Channel A has lower power level thresholds compared to its Channel B. Of the three plots, the Ghost RF detector's Channel A generally has the most stable power level threshold performance over the frequencies.

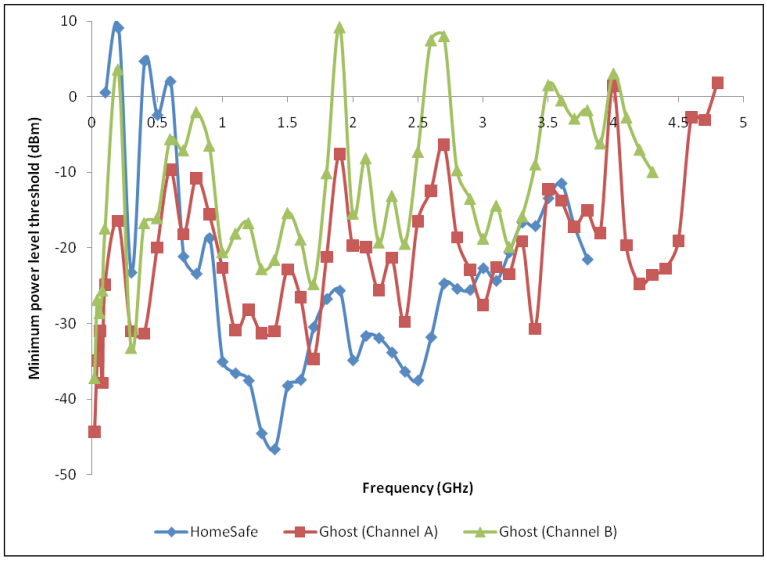

Figure 6: Power level thresholds of the evaluated RF detectors over the tested frequencies.

4. CONCLUSION

Based on the results obtained, the Ghost RF detector is more suitable for detection of wireless spy devices as it can allow for the detection of a wider range of signal frequencies. In addition, its two power level threshold channels, Channel A with lower power level threshold for detection of low power level signals, and Channel B with higher power level threshold to avoid false alarms, allows the user to sweep the suspected area using Channel A, and then, hone in on the target using Channel B. This study will be extended to evaluate a larger range of RF detectors, in particular detectors with larger operating bandwidths.

ACKNOWLEDGEMENT

The authors are grateful to Mr. Kamarulzaman Mustapa, Mr. Ahmad Faridz Abdul Ghafar and Mr. Khairul Anwar Abd Rahim for their support. The authors also thankful to the reviewers, Dr. Mahdi Che Isa, Mdm. Nor Hafizah Mohamed and Mr. Wong Siew Kwan, for their suggestions that have helped strengthen this manuscript.

REFERENCES

Aaronia (2009). *Precompliance Test Antenna Series HyperLOG® 60xxx: Span 680 MHz to 18 GHz*. Aaronia AG, Strickscheid, Germany.

Advantest (2009). *U3741/3751 Spectrum Analyzers*. Advantest Corporation, Chiyoda-ku, Tokyo.

Aeroflex (2005). *2026B Multi-source Generator.* Aeroflex, Plainview, New York.

Cruez, A.F. (2008). *Worried VIPs Stock Up on Anti-spy Devices*. Available online at: http://findarticles.com/p/news-articles/new-straits-times/mi_8016/ is_20080109/worried-vips-stock-anti-spy/ai_n44386752 (Last access date: 4th January 2011).

Curtis, R. (2003). *Introduction to Radio Frequency Radiation*. Occupational Safety & Health Administration (OSHA), US Department of Labor, Washington D.C.

Davis, B. (2004). Spy gear: Modern surveillance tools use the newest technology to catch crooks on the sly. *Police: Law Enforcement Mag.*, **28**: 38-43.

Diamond (2010). *RH799: 70 to 1000MHz Wide-band Antenna*. Diamond Antenna Corporation, Tokyo, Japan.

Hewlett Packard (1998). *HP 8360B Series Synthesized Swept Signal Generators*. Hewlett Packard, Chicago.

Lelux (2008). *HomeSafe RF Detector (Model 790)*. Lelux Electronics Ltd., Tsuen Wan, New Territories, Hong Kong.

Ministry of Labour (MOL) (2009). *Radiofrequency and Microwave Radiation in the Workplace*. Ministry of Labour (MOL), Ontario.

Patel, M.B., Thaker, J.P., Punnam, S. & Jongnarangsin, K. (2007). Pacemaker interference with an iPod. *Human Rhythm*, **4**: 781-784.

Peterson, J.K. (2001). *Understanding Surveillance Technologies: Spy Devices, Their Origins & Applications*. CRC Press, Boca Raton, Florida.

Pinski, S.L. & Trohman, R.G. (2002a). Interference in implanted cardiac devices, Part I. *Pace*, **25**: 1367-1381.

Pinski, S.L. & Trohman, R.G. (2002b). Interference in implanted cardiac devices, Part II. *Pace*, **25**: 1496-1509.

Satcus, 2010. *CT-AS0039 Ghost Wireless RF Detector*. Satcus Industry Co. Ltd., Guangdong, China.

Savry, O. & Vacherand, F. (2010). Security and privacy protection of contactless devices. I n Giusto, D., Iera, Morabito, G. & Atzori (Eds.), *The Internet of Things: 20th Tyrrhenian Workshop on Digital Communications*. Springer, New York, pp. 409-420.

Science & Technology Research Institute for Defence (STRIDE) (2010). *Evaluation of Operating Bandwidth and Power Level Threshold of a HomeSafe RF Detector (Model 790)*. Science & Technology Research Institute for Defence (STRIDE), Ministry of Defence, Malaysia.

Science & Technology Research Institute for Defence (STRIDE) (2011a). *Follow Up Test on the Evaluation of Power Level Thresholds of a HomeSafe RF Detector (Model 790)*. Science & Technology Research Institute for Defence (STRIDE), Ministry of Defence, Malaysia.

Science & Technology Research Institute for Defence (STRIDE) (2011b). *Follow Up Test on the Evaluation of Operating Bandwidth of a HomeSafe RF Detector (Model 790)*. Science & Technology Research Institute for Defence (STRIDE), Ministry of Defence, Malaysia.

Science & Technology Research Institute for Defence (STRIDE) (2011c). *Evaluation of Operating Bandwidth of a CT-AS0039 Ghost RF Detector*. Science & Technology Research Institute for Defence (STRIDE), Ministry of Defence, Malaysia.

Science & Technology Research Institute for Defence (STRIDE) (2011d). *Evaluation of Power Level Threshold of a CT-AS0039 Ghost RF Detector*. Science & Technology Research Institute for Defence (STRIDE), Ministry of Defence, Malaysia.

Seidman, S., Randall, Brockman, R., Lewis, B.M., Guag, J., Shein, M.J., Clement, W.J., Kippola, J., Digby, D., Barber, C. & Huntwork, D. (2010). In vitro tests reveal sample radiofrequency identification to implantable pacemakers and implantable cardioverter-defibrillators. *Human Rhythm*, **7**: 99-107

Siew, A. & Yuen-C, T. (2008). *Spy-cam Detectors: Sweeping Away the Myths*. Available online at:

http://www.straitstimes.com/Free/Story/STIStory_198253.html (Last access date: 4th January 2011).

US Navy (USN) (1997). *Electronics Technician: Volume 1 - Safety*. US Navy (USN), Washington D.C.

APPENDIX

Power level estimation:

P_T : Transmitter power
P_R : Receiver power
G_T : Transmitter gain
G_R : Receiver gain
L : Free-space path loss
L_E : External losses
R : Distance (km)
f : Frequency (MHz)

$$P_R = P_T + G_T + G_R - L - L_E \quad \text{(A1)}$$

$$L = 32.44 + 20\log R + 20\log f \quad \text{(A2)}$$

Effective transmitted power P_{Teff}:

$$P_{T_{eff}} = P_T + G_T \quad \text{(A3)}$$

Effective received power P_{Reff}:

$$P_{R_{eff}} = P_R - G_R \quad \text{(A4)}$$

With L_E and f being constant:

$$P_{R_{eff}} = P_{T_{eff}} - 20\log R - L_O - G_R \quad \text{(A5)}$$

where:

$$L_O = 32.44 + 20\log f + L_E \quad \text{(A6)}$$

ASSESSMENT ON EFFECTS OF UNDER-RELAXATION FACTORS ON 2D INCOMPRESSIBLE LAMINAR FLOW OVER A BACKWARD-FACING STEP (BFS)

Yogeswaran Sinnasamy

Ship Silencing Centre (SSC), Royal Malaysian Navy (RMN), Malaysia

Email: yoges_aero@yahoo.com

ABSTRACT

Relaxation factors play an important role in determining the convergence behaviour of flow in engineering applications. For example, over-relaxation is often used to accelerate the convergence of pressure-velocity iteration methods, which are needed to satisfy an incompressible flow condition. Under-relaxation is sometimes used to achieve numerically stable results when all the flow equations are implicitly coupled together. The amount of over- or under-relaxation used can be critical; too much leads to numerical instabilities, while too little slows down convergence. In this paper, the effects of changing under-relaxation factors for different variables on the numerical solution of 2D incompressible laminar flow over a backward-facing step (BFS) are studied. This is conducted by changing under-relaxation factors for velocities (u_v and u_w) and pressure (u_p) during the 2D simulation. Ten different batches of u_p ranging from 0.1 to 1.0 were used, while the values of u_v and u_w were manipulated between 0.05 and 1.0. For each batch of the computation, the error percentage of pressure (err (p)) and velocities (err (v) and err (w)) were obtained. Based on the plots of err (p), err (v) and err (w) versus the combined values of u_v and u_w, it is found that the recommended values of u_p to achieve lower err (w) during the computation is between 0.6 and 0.8. Based on the plots of the error percentages at three different values of u_p (0.1, 0.2 and 0.5) versus combined values of u_v and u_w, it is determined that in order to achieve lower values of err (v), the recommended values of u_p is between 0.5 and 1.0, with the combined values of u_v and u_w recommended to be between 0.6 and 0.9. Based on findings of the study, the appropriate values of u_p and combined values u_v and u_w can be selected to achieve the levels of error percentage permitted for computational studies.

Keywords: *Under-relaxation factors; convergence; pressure-velocity iteration methods; numerical instabilities; 2D incompressible laminar flow; backward-facing step (BFS).*

1. INTRODUCTION

Flow along a sudden expansion channel is one of the common flow mechanisms which have attracted researchers from various fields due to the importance of such type of flow in technology and scientific research, and can be found in many applications, ranging from human medicine to the latest engineering technologies. In aerospace engineering, this type of flow can be found on gas turbine engine airfoils of commercial and military aircrafts as shown in Figure 1.

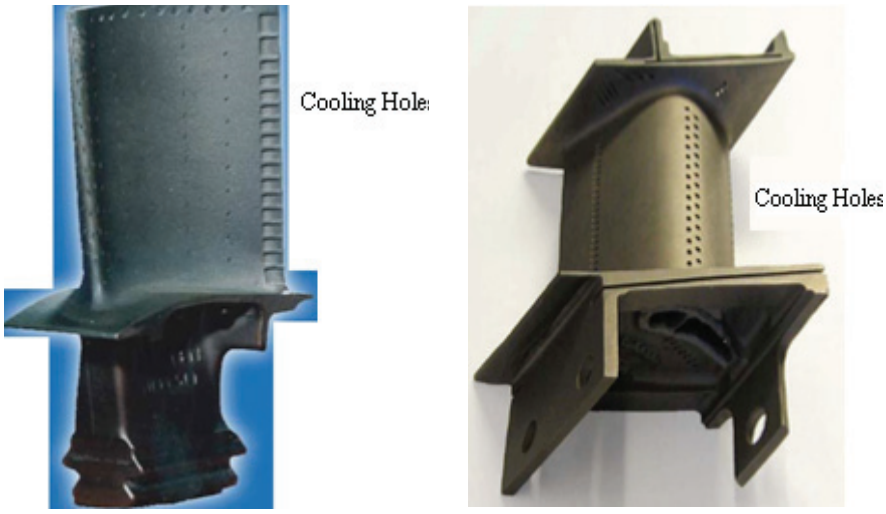

Figure 1: Airfoils of gas turbine engine with cooling holes: (a) Blade; and (b) Vane. (Source: Bons *et al.*, 2002)

From the schematic of the airfoil shown in Figure 2, the cooling holes placed on the surface of the airfoil allow coolant to pass from the internal cavity to the external surface. The ejection of coolant gas through the holes in the airfoil body results in a layer or "film" of coolant gas flowing along the external surface of the airfoil (Bogard, 2006). This is one of the examples of sudden expansion channel configuration, and is one of the simplest geometries of sudden expansion flow, which is a backward-facing step (BFS) flow. Figure 3 shows a BFS flow in a duct where the step height is h, the upstream channel is L_u and downstream channel is L_d.

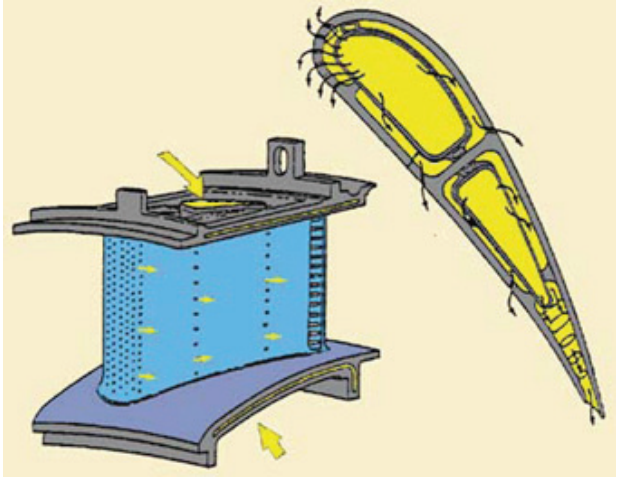

Figure 2: Schematic of film cooling configurations on a vane. (Source: Bogard, 2006)

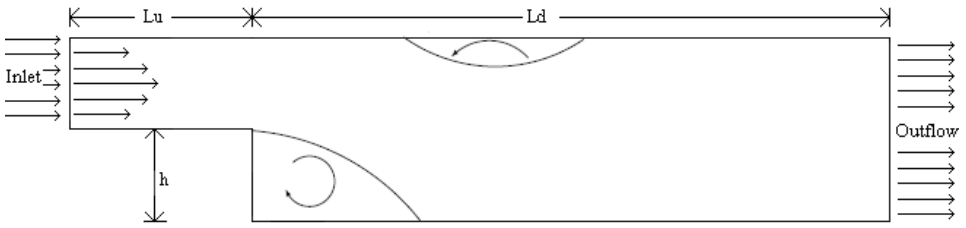

Figure 3: Backward-facing step flow in a duct.

While there have been various numerical studies conducted on 2D BFS flow (Armaly *et al.*, 1983; Lee & Mateescu, 1998; Yee, 1999; Erturk *et al.*, 2005; Abughalia, 2008; Erturk, 2008; Rouizi *et al.*, 2009), not much attention has been given to the investigation of the ranges of safe and recommended values for relaxation. Barron & Neyshabouri (2003) performed computational investigation on the effects of changing under-relaxation factors for different variables, convective schemes and grid sizes on the convergence of the numerical solution of 2D turbulent flow situations. The under-relaxation factors for velocity (α_u, α_v), turbulent kinetic energy (α_k), dissipation of turbulent kinetic energy (α_ε), eddy viscosity (α_ν) and generation term (α_g) were systematically changed between the limits of 0.1 – 0.9, and the divergence or the number of iterations (NITER) required to reach convergence was recorded in each case. Three different flows were tested, duct flow, trench flow and inclined free falling jet, and two different convective schemes were used, the power-law scheme (POW) and second-order upwind scheme (SOU). This investigation allowed for the computation of two ranges for any under-relaxation factor, namely the range of safe values, which is based on the non-divergent solution, and recommended range or value, which is narrower than the safe range and results in faster convergence. No such study has been conducted to investigate the ranges of safe and recommended values for laminar flow situations.

In this study, the effect of under-relaxation factors on the error percentage produced during the computation of 2D steady incompressible flow over a BFS is studied. Three under-relaxation factors which can affect the convergence of the BFS flow have been identified; *x*- and *y*-direction velocities, and pressure. The suitable ranges of these factors in order to achieve higher accuracy of BFS flow computation are determined.

2. COMPUTATIONAL METHODOLOGY

2.1 Geometry and Grid Formation of Computational Domain

The computational domain used for the preliminary computation is shown in Figure 4. The domain has dimensions of 1.000 m x 0.250 m, with a step block placed at the left-hand side corner of the lower plane. The domain consists of a shorter entry length with the dimensions of the step being 0.100 m x 0.025 m. This computation is set up as 2D with just one cell along the spanwise (*y*) direction. The variations in the spanwise direction are not significant; hence, a 2D model is a fairly good approximation. The origin of the coordinate system is placed at the lower step corner.

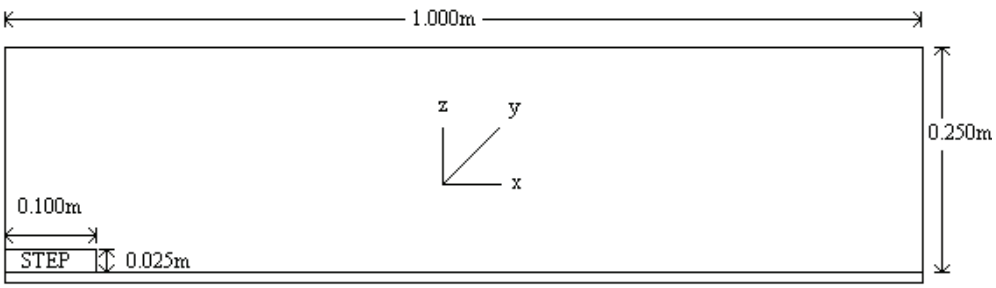

Figure 4: Geometry of the computational domain. *x*-, *y*-, and *z*-coordinate directions denote the streamwise, transverse and spanwise directions respectively.

The next step of the solution process is to make the appropriate mesh selection so that the problem can be solved and accurate values can be achieved. The domain is divided into 7 regions along *x*- and *z*-directions as indicated in Table 1, and as shown in Figures 5 and 6. For the *y*-plane of the domain, it is considered as one single cell to set up a 2D domain. Each region consists of rectangular cells with different expansion or extraction power, and symmetrical conditions. A grid stretching at corners is recommended, because of the pressure and velocity gradients, which can be a serious drawback to the convergence of the numerical procedure.

The boundary conditions are schematically shown in Figure 7. At the inlet boundary, we imposed that the flow is a fully developed Plane Poiseuille flow between parallel plates such that the inlet velocity profile is parabolic with the maximum streamwise velocity of *U*. In this study, the inlet boundary is located 0.100 m upstream of the step.

Table 1: Mesh setting details.

Region	End Point	Cells	Distribution	Power	Symmetric	Cell Power
***x*- direction settings**						
1	0.100	20	Geometric Program	1.200	Yes	Set
2	0.200	40	Geometric Program	1.050	Yes	Set
3	0.300	50	Geometric Program	1.050	Yes	Set
4	1.000	35	Geometric Program	1.130	No	Set
***z*-direction settings**						
5	0.010	15	Geometric Program	1.050	Yes	Set
6	0.035	20	Geometric Program	1.050	Yes	Set
7	0.250	50	Geometric Program	1.100	Yes	Set
***y*-direction settings**						
8	0.010	1	Power Law	1.000	No	Set

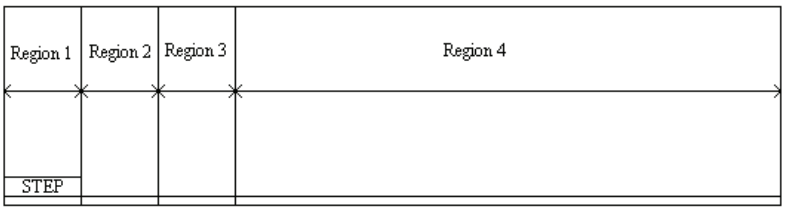

Figure 5: Regions along the *x*- direction.

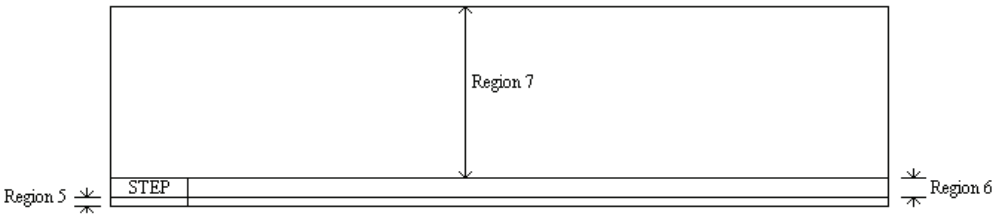

Figure 6: Regions along *z*-direction.

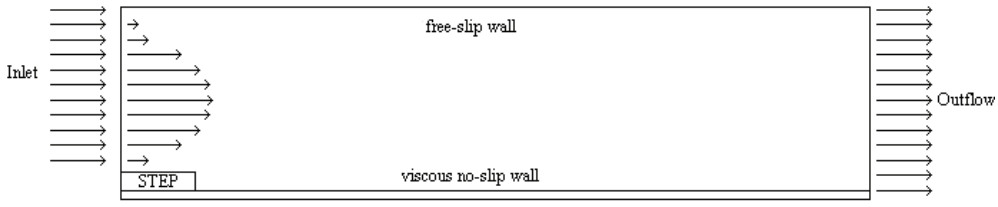

Figure 7: The boundary conditions.

At the outlet (x = 1.000 m), the outflow boundary conditions are used to allow the fluid to freely leave the domain with minimum reflection. The lower boundary is a viscous no-slip wall and the top wall is a symmetry free-slip boundary. Symmetry boundary conditions are also used in the spanwise direction.

2.2 Case Description

This case is described as 2D steady incompressible flow over a BFS flow and fully developed with the streamwise velocity component U. The objective of the computation is to determine the relationship between under-relaxation factors and error percentages of concerned variables such as pressure and velocities of the converged flow solutions. The average inlet velocity is 0.100 ms^{-1} and the physical properties of fluid are constants; density d is 1.189 kgm^{-3}, and viscosity v is 1.544 x 10^{-5} m^2s^{-1}. The other velocity components of the y- and z-directions are set as zero at the inlet section. The no-slip boundary condition is applied at all the wall surfaces. Fully developed parabolic velocity conditions are applied at the inlet boundary of the computation domain. The Reynolds number Re (Equation 1) is computed to be 1,620 or 1.620 x 10^3.

$$\mathrm{Re} = \frac{U \bullet d}{v} \qquad (1)$$

2.3 Numerical Scheme

An important consideration in CFD is the discretisation of the convection terms in the finite-volume equations. The accuracy, numerical stability and the boundedness of the solution depends on the numerical scheme used for these terms. The central issue is the specification of an appropriate relationship between the convected variable, stored at the cell centre, and it values at each of the cell faces. In this study, the hybrid-differencing scheme (HDS) has been used for all variables. This scheme employs the 1st order upwind-differencing scheme (UDS) in high convection regions, and the 2nd order central differencing scheme (CDS) in low-convection regions. The UDS is bounded and highly stable, but highly diffusive when the flow direction is skewed relative to the grid lines. The HDS is only marginally more accurate than the UDS, as the 2nd order CDS will be restricted to regions of low Peclet number.

3. TEST CASES

Under-relaxation factors are significant parameters affecting the convergence of a numerical scheme. In this study, 2D simulations for flow over a backward step are performed by changing under-relaxation factors for velocities (u_v and u_w) and pressure (u_p). Ten different batches of u_p ranging from 0.1 to 1.0 as indicated in Table 2 were used, while the values of u_v and u_w were manipulated between 0.05 and 1.0. For example, in the first batch at $u_p = 0.1$, the first computational runs started with $u_v = 0.05$ and $u_w = 0.05$. Once the first computational run had converged, for the second computational run for the same value of u_p, the value of u_v was maintained at 0.05 but the value of u_w was changed to 0.06. Then, for the third computational run, the value of u_v was changed to 0.06 and the value of u_w to 0.05. Then, for the fourth computational run, the value of u_v and u_w were changed to 0.06. This pattern of variable manipulation was continued until the values of u_v and u_w reached 1.0, and the steps as mentioned above were repeated for the following batches u_p with values of 0.2 to 1.0 (increments of 0.1). In total, there were 430 computational runs with each batch consisting of 43 runs.

Table 2: Values of velocities (u_v and u_w) and pressure (u_p) used in the test.

Batch	Variables	
	Fixed	Manipulated
1	$u_p = 0.1$	$0.05 \leq u_v, u_w \leq 1.00$
2	$u_p = 0.2$	$0.05 \leq u_v, u_w \leq 1.00$
3	$u_p = 0.3$	$0.05 \leq u_v, u_w \leq 1.00$
4	$u_p = 0.4$	$0.05 \leq u_v, u_w \leq 1.00$
5	$u_p = 0.5$	$0.05 \leq u_v, u_w \leq 1.00$
6	$u_p = 0.6$	$0.05 \leq u_v, u_w \leq 1.00$
7	$u_p = 0.7$	$0.05 \leq u_v, u_w \leq 1.00$
8	$u_p = 0.8$	$0.05 \leq u_v, u_w \leq 1.00$
9	$u_p = 0.9$	$0.05 \leq u_v, u_w \leq 1.00$
10	$u_p = 1.0$	$0.05 \leq u_v, u_w \leq 1.00$

4. RESULTS AND DISCUSSION

For each batch of the computation, the error percentage of pressure (*err (p)*) and velocities (*err (v)* and *err (w)*) were obtained from the white frame boxes in the computational window, as shown in Figure 8. In this window, the plot on the left contains the values of the monitoring point and the lines are expected to be flat towards the end of the computation, indicating convergence. The plot on the right shows the computation errors at the monitoring point and the lines are expected to go down towards the end of the computation. These trends indicate that the simulation results are stable.

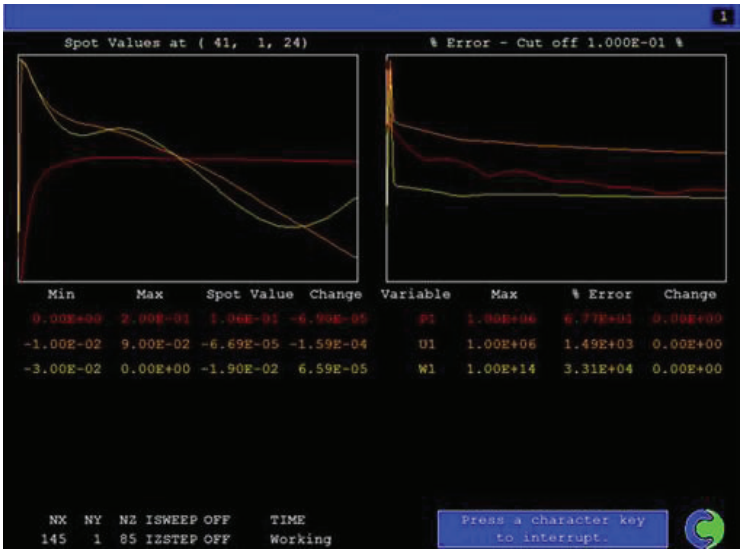

Figure 8: The computation window for one batch of the computation.

The error percentages were plotted as shown in Figure 9. The range of the combined values of u_v and u_w on the *x*-axis of the plots is $0.05 \leq u_v, u_w \leq 1.00$. Each plot consists of three lines indicating *err (p)*, *err (v)* and *err (w)* versus the combined values of u_v and u_w. Increasing and constant trends of *err (p)* and *err (v)*, respectively, are observed, with these trends being almost the same for all ten batches. For *err (w)*, Figure 9 (a) - (e) shows increasing trends at $0.1 \leq u_p \leq 0.5$, but the gradient of the trend becomes lower at $0.6 \leq u_p \leq 0.7$. The trend becomes almost constant at $u_p = 0.8$, but increased again at $0.9 \leq u_p \leq 1.0$. Based on these findings, it can be concluded that the recommended values of u_p to achieve lower *err (w)* during the computation is between 0.6 and 0.8.

Each plot in Figure 7 shows three lines indicating the error percentages for u_p, u_v and u_w at three different values of u_p versus the combined values of u_v and u_w. Based on the Figure 10 (a), it was found that *err (p)* increases at the same trend for $0.1 \leq u_p \leq 1.0$. However, for Figure 7(b), it was found that the trends of *err (v)* in this range of u_p values are not the same; *err (v)* at $u_p = 1.0$ decreases with the combined values of u_v and u_w. However, *err (v)* at $u_p = 0.1$ and 0.5 increases, with the gradient of the increment being larger for $u_p = 0.1$ than $u_p = 0.5$. For Figure 7(c), it was found that *err (w)* increases with the combined under-relaxation factors for $0.1 \leq u_p \leq 1.0$, with these increments having different trends. Based on these findings, it is determined that in order to achieve lower values of *err (v)*, the recommended values of u_p is between 0.5 and 1.0, with the combined values u_v and u_w of are recommended to be between 0.6 and 0.9.

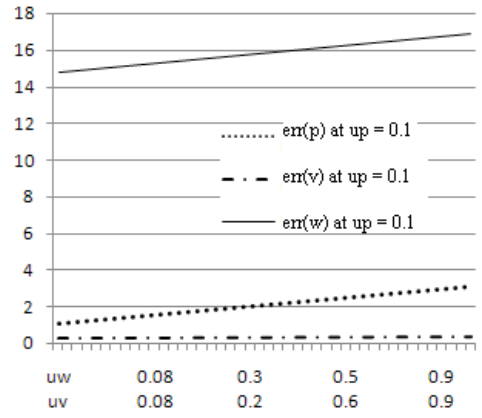
18
16
14
12
10
8
6
4
2
0
en(p) at up = 0.1
en(v) at up = 0.1
en(w) at up = 0.1
uw 0.08 0.3 0.5 0.9
uv 0.08 0.2 0.6 0.9

(a)

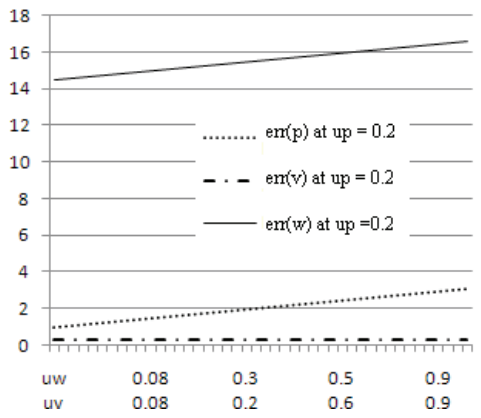
18
16
14
12
10
8
6
4
2
0
en(p) at up = 0.2
en(v) at up = 0.2
en(w) at up =0.2
uw 0.08 0.3 0.5 0.9
uv 0.08 0.2 0.6 0.9

(b)

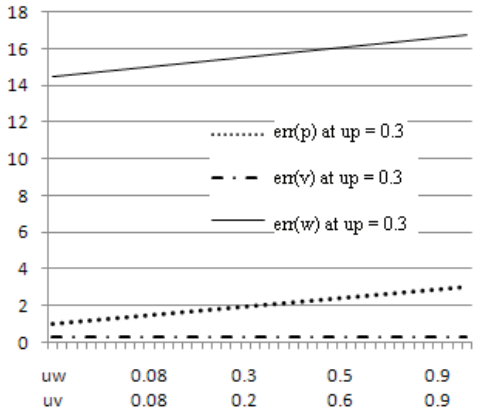
18
16
14
12
10
8
6
4
2
0
en(p) at up = 0.3
en(v) at up = 0.3
en(w) at up = 0.3
uw 0.08 0.3 0.5 0.9
uv 0.08 0.2 0.6 0.9

(c)

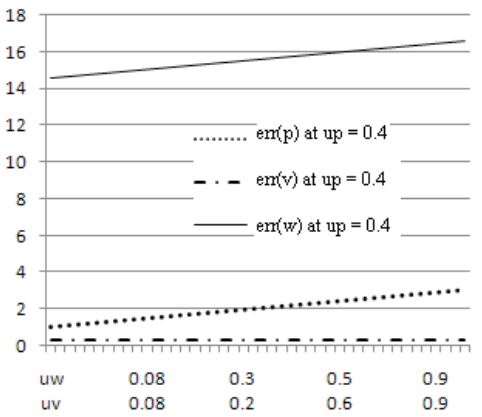
18
16
14
12
10
8
6
4
2
0
en(p) at up = 0.4
en(v) at up = 0.4
en(w) at up = 0.4
uw 0.08 0.3 0.5 0.9
uv 0.08 0.2 0.6 0.9

(d)

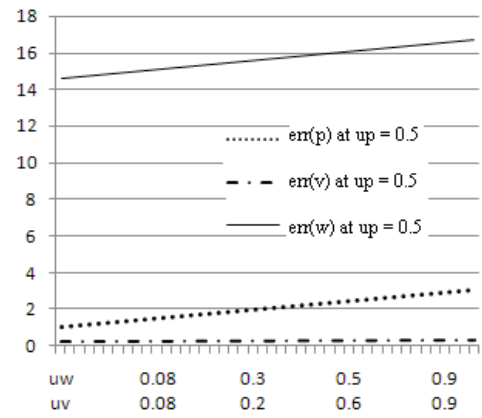
18
16
14
12
10
8
6
4
2
0
en(p) at up = 0.5
en(v) at up = 0.5
en(w) at up = 0.5
uw 0.08 0.3 0.5 0.9
uv 0.08 0.2 0.6 0.9

(e)

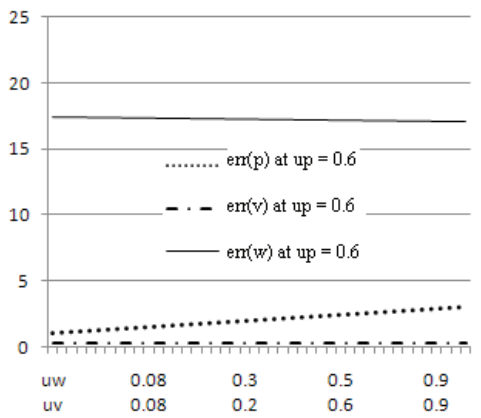
25
20
15
10
5
0
en(p) at up = 0.6
en(v) at up = 0.6
en(w) at up = 0.6
uw 0.08 0.3 0.5 0.9
uv 0.08 0.2 0.6 0.9

(f)

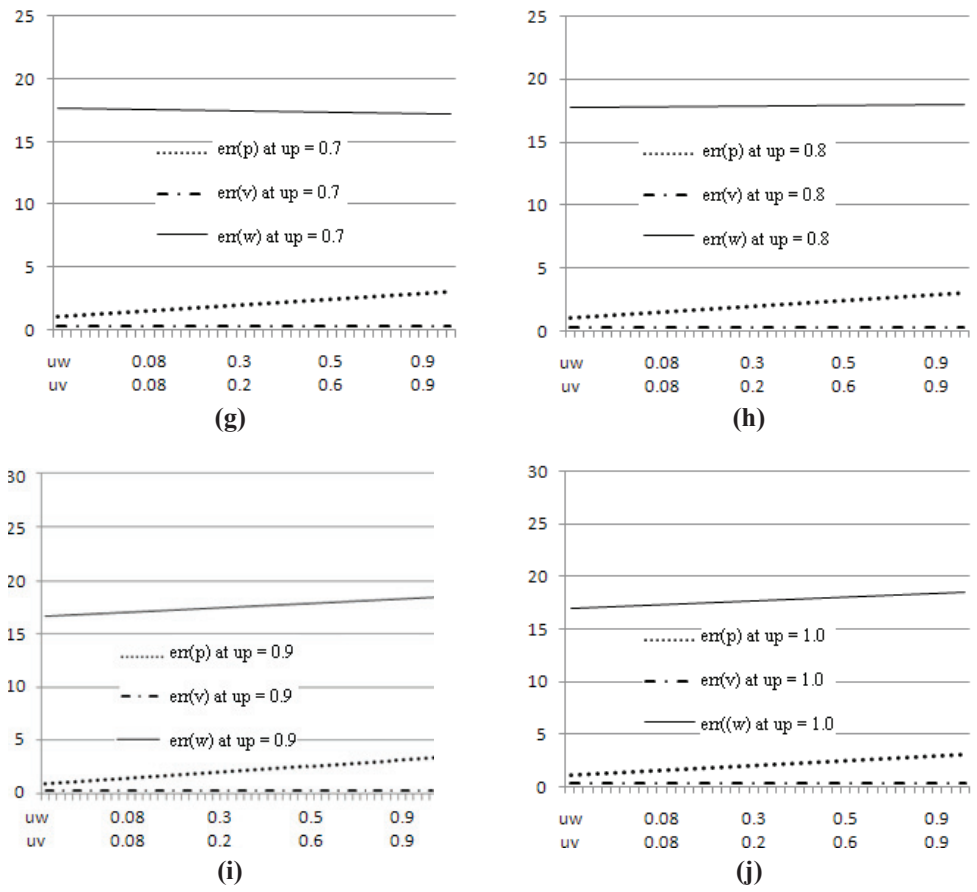

Figure 9: Plots of the error percentages of u_p, u_v and u_w at u_p = (a) 0.1; (b) 0.2 ; (c) 0.3; (d) 0.4; (e) 0.5; (f), 0.6; (g) 0.7; (h) 0.8; (i) 0.9; and (j) 1.0.

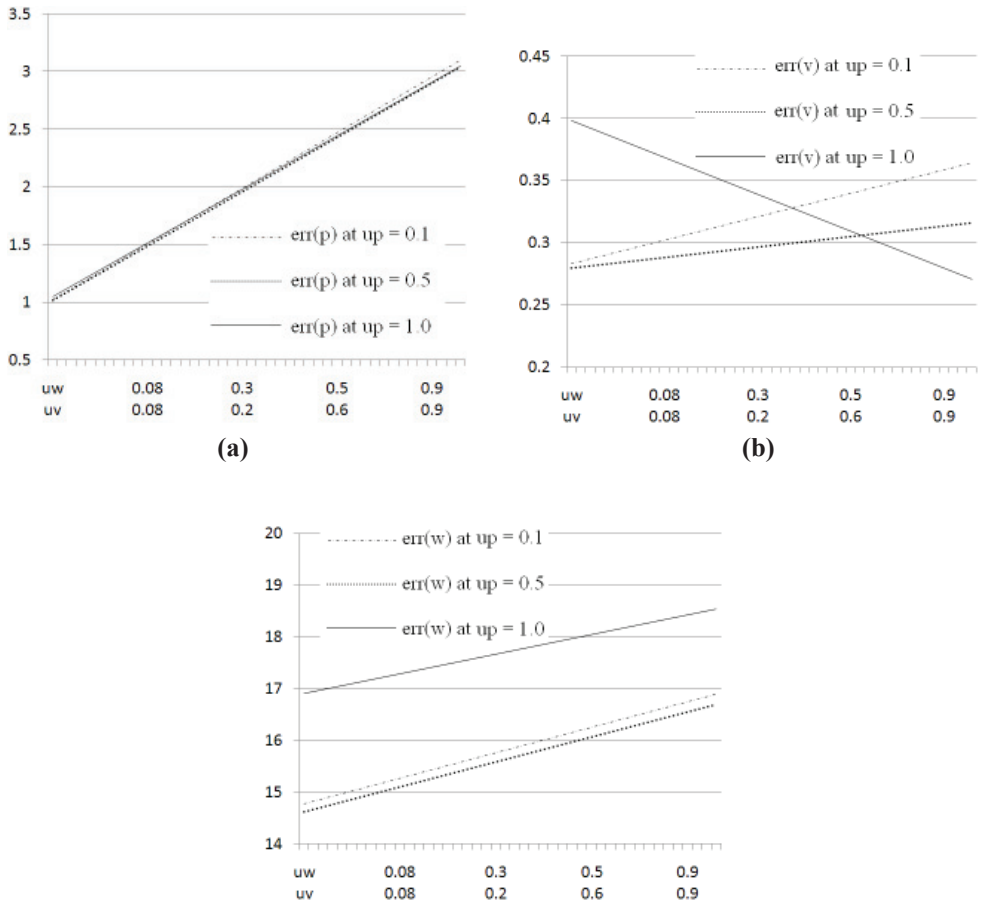

Figure 10: Error percentages of (a) u_p; (b) u_v; and (c) u_w at = 0.1, 0.5 and 1.0.

5. CONCLUSION

It can be concluded that as the results of error percentages presented in Figures 9 and 10 agree with each other, the appropriate value of u_p and combined values of u_v and u_w can be selected to achieve the levels of error percentage permitted for computational studies. The recommended values of u_p to achieve lower *err (w)* during computation are between 0.6 and 0.8. In order to achieve lower values of *err (v)*, the recommended values of u_p are between 0.5 and 1.0, while the combined values u_v and u_w of are recommended to be between 0.6 and 0.9. Future studies will focus on the effect of various values of Reynolds numbers and the formation of streamlines of 2D incompressible laminar flow over a BFS using different numerical schemes, such as UPWIND, QUICK, SUPBEE and MINMOD. In addition, the study on determining the separation and reattachment points of flow over a BFS is also needed as this type of information is important for improving cooling effectiveness of gas turbine components.

REFERENCES

Abughalia, M.A.M. (2008). Prediction of laminar flow over a back facing step using new formula of penalty parameter. *Adv. Fluid Mech.*, **7**: 23-34.

Armaly B.F., Durst F., Pereira J.C.F & Scho¨nung, B. (1983). Experimental and theoretical investigation of backward-facing step flow. *J. Fluid Mech.*, **27**:473–96.

Bogard, D.G. (2006). Airfoil film cooling. *In* Dennis, R. (Ed.), *The Gas Turbine Handbook*. National Energy Technology Laboratory (NETL), Office of Fossil Energy, US Department of Energy, Washington D.C.

Bons, J., Shih, T., Wang, Z.J., Hamed, T., Tabakoff, W. & Rivir, R. (2002). *Turbine Surface Degradation with Service and Its Effects on Performance*. Brigham Young University, Provo, Utah.

Erturk, E (2008). Numerical solutions of 2-D steady incompressible flow over a backward-facing step, Part I: High Reynolds Number solutions. *Comput. Fluids*, **37**: 633–655.

Erturk, E., Corke, T.C. & Gokcol, C. (2005). Numerical solutions of 2-D steady incompressible driven cavity flow at high reynolds numbers. *Int J Numer Methods Fluids*, **48**:747–777.

Barron, R.M. & Neyshabouri, A. A. S. (2003). Effects of under relaxation factors on turbulent flow simulations. *Int. J. Numer. Meth. Fluids*, **42**: 923–928.

Lee, T. & Mateescu, D. (1998).Experimental and numerical investigation of 2-D backward-facing step flow. *J. Fluids Struct.*, **12**: 703-716.

Rouizi, Y., Favennec, Y., Ventura, J. & Petit, D. (2009). Numerical model reduction of 2D steady incomressible laminar flows: Application on the flow over a backward-facing step. *J. Comput. Phys.*, **228**: 2,239-2,255.

Yee, H.C., Torczynski, J.R., Morton, S.A., Visbal, M.R. & Sweby, P.K (1999). On spurious behavior of CFD simulations. *Int. J. Numer. Methods Fluids*, **30**:675–711.

DETECTION OF SKI SLOPES IN VIBRATION SPECTRUMS

Mohd Moesli Muhammad*, Subhi Din Yati & Irwan Mohamad Noor

Maritime Technology Division (BTM), Science and Technology Research Institute for Defence (STRIDE), Ministry of Defence, Malaysia

*moesli.muhammad@stride.gov.my

ABSTRACT

The most important parameter that must be considered in vibration analysis is the recognition of patterns of faulty data. Ski slopes are commonly present in vibration spectrums when the transducer is not properly mounted. The primary objective of this paper is to study the effect of ski slopes on the overall value of vibration level reading. The test was carried out in two different conditions of mounting; properly mounted and with gap of 2 mm. The properly mounted transducer had a good vibration spectrum with a smooth and flat pattern of noise floor. The transducer with gap of 2 mm had a faulty pattern of vibration spectrum. A ski slope was present, while the noise floor had a rough pattern. Observation of the overall vibration levels showed that the vibration level of the 2 mm gap mounted transducer had increased as compared to the properly mounted transducer. This study demonstrated that loose mounting of transducers can contribute to the presence of ski slopes in vibration spectrums, resulting in increase of overall value of vibration level reading.

Keyword: *Vibration analysis; loose mounting; ski slope; vibration spectrum; transducer*.

1. INTRODUCTION

Vibration analysis is widely used for machinery diagnostics and has been implemented for many applications in condition monitoring of machinery. In vibration analysis, the recognition of patterns of faulty data is an essential skill for vibration analysts. Faulty data can be caused by faulty cables or cable connectors, sensor faults, mounting conditions, settling time, or even cable movement. One of the typical indications of faulty data pattern is the presence of ski slopes in vibration spectrums. A ski slope is a high amplitude of very low frequency content which can cause the increase of overall value of vibration level (Barrett, 2011; Commtest Instruments Ltd., 2006; Metrix Instrument Co., 2011). Figure 1 shows an example of ski slope present in the vibration spectrum of a boat propulsion system.

The overall vibration level is the total sum of all energies in the spectrum of the vibration measured by the transducer within the frequency span chosen (Berry, 2002). The transducer may even sense vibrations from an adjacent machine and include it within the vibration spectrum. It collects all vibrations regardless of source or origin, making them part of both the vibration spectrum and the overall vibration. Overall vibration is different from vibration spectrums in frequency domain as it is a total summation of all the vibrations, no matter what the frequency range. Figure 2 shows the overall vibration level of a spectrum. The overall vibration level is calculated by taking the square of the amplitude (A^2) of each frequency bin (A_i), summing the squared amplitudes, computing the square root of the sum, and dividing this sum with the noise factor for the FFT window chosen. The equation of overall vibration level is summarised in Equation 1.

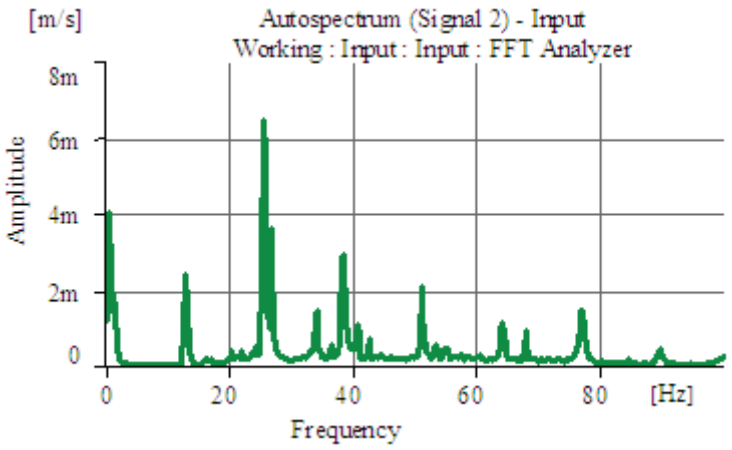

Figure 1: High amplitude of ski slope at 0 Hz present in the vibration spectrum of a boat propulsion system.

$$OA(inRSS) = \frac{\sqrt{\sum_{i=1}^{n} A_i^2}}{\sqrt{N_{BF}}} \qquad (1)$$

OA	=	Digital overall level of vibration spectrum
RSS	=	Root sum square level, which is the "summation of energies" in the spectrum from F_{min} to F_{max}.
n	=	Number of FFT lines.
A_i	=	Amplitude of each FFT line.
N_{BF}	=	Noise bandwidth for window chosen (1.5 for Hanning Window).

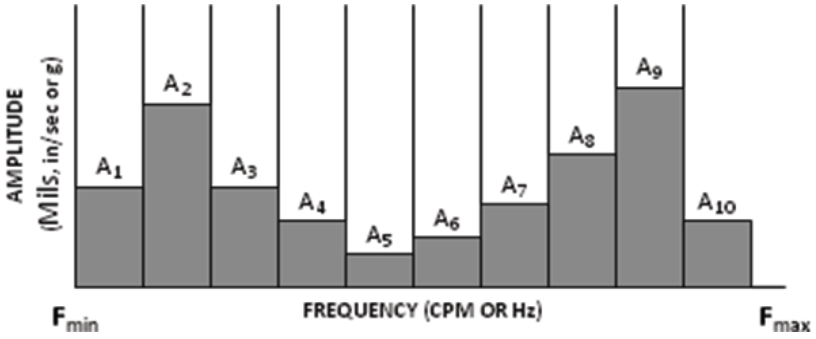

Figure 2: Overall vibration level of a spectrum.
(Source: Berry, 2002)

The problem related to ski slopes is the interruption of online condition monitoring systems due to the alarm limit being triggered, which means that the vibration level has exceeded the

limits set. There are many reasons why ski slopes occur and in many cases, it is contributed by manmade mistake or artefacts (Mobius Institute, 2008; Dahl, 2001).

The primary objective of this paper is to study the effect of ski slopes on the overall value of vibration level reading. It is demonstrated that loose mounting, which can occur when the setup of the vibration measurement is not conducted properly, is one of the causes of the presence ski slopes in vibration. In addition, it is also shown that analysis of vibration should not only be based on overall value reading but must also be in conjunction with vibration spectrum in the frequency domain in order to validate the data and avoid wrong interpretation of the system that is being monitored.

2. EXPERIMENTAL SETUP

The test rig used in this study is shown in Figure 3. It consists of an AC motor which is connected to the shaft and is supported by two bearing housings. A transducer with sensitivity of 10 pc/g and dynamic range of 0.1 to 12 kHz was used to measure vibration. The transducer was mounted using a magnet mount in the vertical direction on the bearing housing just above the drive shaft bearing. The test was carried out in two different conditions of mounting, properly mounted and with gap of 2 mm (Figure 4). The motor was run at a constant speed of 3,600 RPM or 60 Hz. The data of the vibration measurement test was recorded and the results were displayed in frequency domain and root mean square (RMS) respectively. Before the test, the bearing housings were tightened and each component in the test rig was checked to be in good condition in order to eliminate component fault frequency.

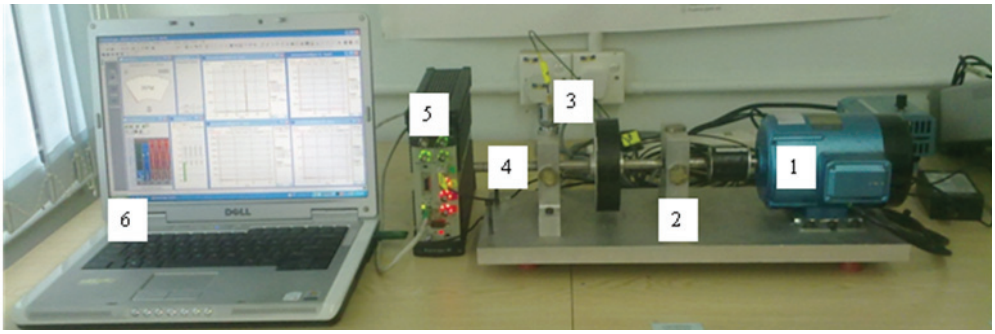

Figure 3: Experimental setup of the test rig: (1) AC drive motor; (2) Bearing housing; (3) Transducer; (4) Drive shaft; (5) Data acquisition hardware; and (6) Pulse Labshop software.

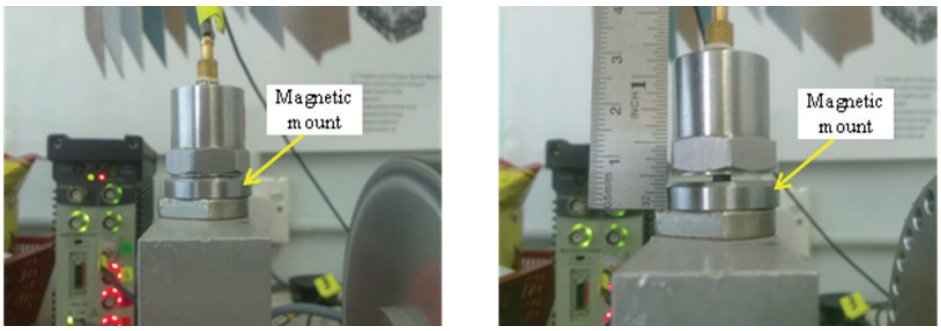

(a) (b)

Figure 4: The two different conditions of transducer mounting tested: (a) Properly mounted (no gap); and (b) 2 mm gap.

3 RESULTS AND DISCUSSION

The vibration signals from the two conditions of transducer mounting are shown in Figure 5. The results are presented in frequency domain, which is a normal practice in vibration analysis to determine the individual frequency of each component (Tongue, 1996; Goldman, 1999; Wowk, 1991). In this paper, the vibration spectrum is zoomed in the range of 100 Hz in order to examine the ski slope peak at a very low frequency.

In Figure 5(a), where the transducer was properly mounted, a distinct peak appears at frequency of 60 Hz and is identified as the shaft or running speed. The noise floor pattern is smooth and almost flat. Noise floors in vibration spectrums represent the condition of background vibration during measurements, which causes noise. It can originate from the test rig, cables or adjacent machinery. Since all sources of noise were eliminated before the experiment was carried out, a smooth pattern of noise floor was obtained, indicating that the transducer had a strong contact and was firmly in place on the bearing housing.

The signal of the transducer with gap of 2 mm is shown in Figure 5(b). Similar to Figure 5(a), the shaft speed appears at frequency of 60 Hz. However, at a very low frequency, near 0 Hz, a peak with high amplitude is present. This peak is a ski slope, which shows that the data is faulty . It indicates a faulty vibration spectrum which is due to poor vibration measurement. The mounting gap affects the contact between the transducer and the bearing housing. The transducer itself easily rattles and vibrates when the component that is being measured is vibrating. It creates noise and produces a rough pattern on the noise floor in the vibration spectrum. However, in practice, the presence of ski slopes is not just limited to mounting looseness but also can be due to thermal transience, excessive cavitations, saturation of sensors and sensors being bumped at the beginning of the measurement (Mobius Institute, 2008; Cole-Parmer, 2011; LaRocque, 2011).

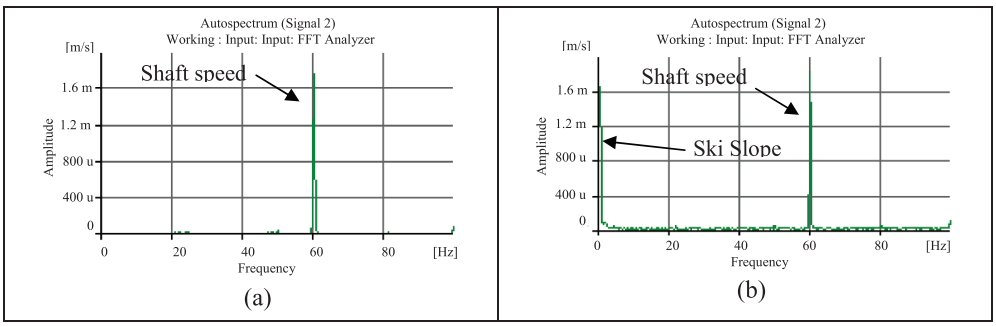

Figure 5: Vibration spectrum results in frequency domain: (a) Properly mounted (no gap); and (b) 2 mm gap.

The ski slope peak also influences the overall value of vibration level. Figure 6 shows the overall vibration level in root mean square (RMS) of the spectrums of both conditions of transducer mounting being tested. The overall vibration is total summation of all the vibrations measured by the transducer within the frequency span chosen (Berry, 2002). It is a single value that is relatively easy to collect, process, analyse and trend. The result shows that the vibration level of the properly mounted transducer is 1.74 mm/s, and 2.74 mm/s for the 2 mm gap mounted transducer. The increase of 57 % in vibration level of the 2 mm gap transducer can affect the vibration reading if the system is being monitored by an online condition monitoring system. It will trigger the alarm limit that has been set and gives wrong information on the system that is being monitored.

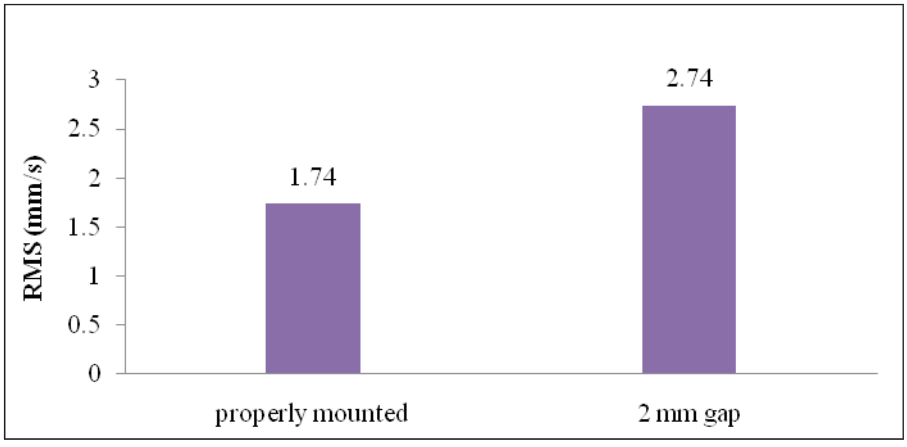

Figure 6: The overall value of vibration levels obtained in RMS.

5. CONCLUSION

This experiment was carried out in two conditions of transducer mounting. The properly mounted transducer had a good vibration spectrum with a smooth and flat pattern of noise floor. The transducer with gap of 2 mm had a faulty pattern of vibration spectrum. A ski slope was present, while the noise floor had a rough pattern. Observation of the overall vibration

levels showed that the vibration level of the 2 mm gap mounted transducer had increased as compared to the properly mounted transducer. It can be concluded that loose mounting of transducers contributes to the presence of ski slopes in vibration spectrums, thus influencing the overall value of vibration level. Therefore, the analysis of vibrations should be conducted on both overall value in Root Mean Square (RMS) and vibration spectrums in frequency domain to avoid wrong interpretation of the system being monitored.

ACKNOWLEDGEMENT

This study was conducted as part of the 9th Malaysia Plan (RMK9) project entitled 'Royal Malaysian Navy Ship Propulsion System Condition Based Monitoring'. The authors would like to thank the Science and Technology Research Institute for Defence (STRIDE) for providing research facilities and technical assistance during the experimental works.

REFERENCES

Barrett, R. M. (2011). *Troubleshooting accelerometer installations*. Available online at: http://www.globalspec.com/wilcoxon/ref/AccelInstall.html (Last access date: 17th February 2011).

Berry, J.E. (2002). *How to Implement an Effective Condition Monitoring Program Using Vibration Analysis*. Technical Associates of Charlotte, Inc.,USA.

Cole-Parmer (2011). *Trouble Shooting Industrial Accelerometer Installation.* Available online at:http://www.coleparmer.com/techinfo/techinfo.asp?htmlfile=accelerometer.htm&ID=3 (Last access date: 12th February 2011).

Commtest Instruments Ltd. (2006). *Beginner's Guide to Machine Vibration, Technical Manual*. Commtest Instruments Ltd., Christchurch, New Zealand.

Dahl, K.C. (2001). *Accelerometer Overload*. DLI Engineering Corporation. Woburn, USA.

Goldman, S. (1999). *Vibration Spectrum Analysis, A Practical Approach*. Industrial Press Inc, New York.

LaRocque, T. (2011). *Practical Tips to Identifying and Troubleshooting Portable Measurement Cables for Vibration Analysis.* Available online at: http://www.ctconline.com/pdf/pubTechPapers/07-Troubleshooting%20-%20Portable%20Measurement%20Cables%20for%20Vibration%20Analysis.pdf (Last access date: 17th February 2011).

Metrix Instrument Co. (2011). *Accelerometer Application Note.* Metrix Instrument Co., Houston, USA.

Mobius Institute (2008). *Vibration Training Course Book*. Mobius Institute, Australia.

Tongue, B.H. (1996). *Principles of Vibration*. Oxford University Press Inc, New York.

Wowk, V. (1991). *Machinery Vibration, Measurement and Analysis*. Mac Graw Hill Inc., USA.

ALL-HAZARDS RESILIENCE: A PARADIGM FOR THE 21ST CENTURY

Rita Parker

Innovative Solutions for Security and Resilience (ISSR), Australia

Email: rita.parker@issr.com.au

ABSTRACT

The challenges of dealing with fast moving disruptive and catastrophic events required a significant change in thinking and approach. The extent and frequency of disruptive events faced by communities, organisations and nations has demanded a new way of dealing with the changing global political, cultural and social environment which has added uncertainty to an unknown future in the 21st century. A significant paradigm shift has taken form through the convergence of two different models to address the imperative for a different approach. All hazards resilience has emerged as the paradigm for the future management of disruptive events which impact communities, organisations, individuals and nations.

Keywords: *All-hazards; resilience; disruption; lessons learned; risk management; group think*.

1. INTRODUCTION

For many years, there has been a clear divide between how security and safety issues were viewed and dealt with by governments. Each area was handled differently with separate procedures and treatments. However, the extent and frequency of threats and disruptions experienced worldwide this century, from both natural and anthropogenic sources, has required a change in thinking and approach. This has been driven in part by the recognition that the future is not predictable and plans cannot address every possible, likely or unexpected disruption.

The necessary change in thinking and approach has resulted in the emergence and convergence of two different but complementary models to meet the imperative of change. The first model relates to a greater understanding of the concept and application of resilience as an overarching framework for societies and organisations to deal with crises and disruptions. The second is the adoption of the evolving concept of an all-hazards approach to deal with the extensive range of natural, accidental and intentional disruptions. Consequently, we have a convergence of resilience and all-hazards.

These two models have been combined to produce a significant paradigm shift in strategic thinking, planning and operational level responses to address all forms of disruption, whether accidental, natural or deliberate. In turn, this paradigm has led to both a shift and a union of ideas, approaches and, to some extent, roles to deliver outcomes.

2. RESILIENCE

The nature and meaning of resilience has been debated over many years with each discipline offering its own definition. It is a concept which has been around for some time in the areas of ecology, engineering and psychology, and resilience is gaining traction in other milieus every day: corporations, governments, critical infrastructure owners and operators through to national security and personal well being.

Interpretations of resilience also vary in different communities, organisations or nations because different populations respond differently to disruptions, catastrophic or unexpected events. For any definition to be meaningful, it needs to be based on a shared understanding with the primary dimensions clarified and it needs to be contextually relevant. Resilience implies that individuals, communities and organisations are able to reduce their exposure to risks and at the same time, enhance their ability to recover. Organisations often accept a level of risk to enable activities to occur that give a benefit to the wider society. Adopting a resilience based approach means focusing on capabilities and resources to anticipate, to prepare and to manage disruptive events. This approach is different from a vulnerability-based approach which focuses on identifying weaknesses and then implementing mitigation strategies to overcome them. This latter approach depends to a large extent on risk identification and its assessment.

Resilience requires a holistic, systemic approach which includes all stakeholders, integrates previously disparate elements and explicitly recognises the need for adaptation and agility. An all-hazards resiliency approach implicitly offers economies of scale and reduced duplication of effort while anticipating and continually adjusting to changing circumstances through a more adaptive and flexible approach to survive and even thrive after a disruption.

3. ALL-HAZARDS

The term all-hazards has also been defined in a number of different ways by different organisations. For example, the US Department of Homeland Security defines it as (DHS, 2006):

> *"an approach for prevention, protection, preparedness, response, and recovery that addresses a full range of threats and hazards, including domestic terrorist attacks, natural and manmade disasters, accidental disruptions, and other emergencies"*.

This definition has been expanded upon by George Washington University as (ICDRM, 2007):

> "*a descriptor that denotes a specific strategy for managing activities in an emergency management program. Throughout the four phases of emergency management, management structure, processes and procedures are developed so they are applicable to every significant identified hazard. The remaining hazard specific interventions are layered on top of the basic components as indicated and presented through "incident" annexes in the emergency operations plan (EOP). For example, the procedures for notifying appropriate personnel during EOP activation would use the same process across all hazard types, even though the types of personnel notified and mobilized may vary by hazard*".

4. A PARADIGM SHIFT

Until a few decades ago, disasters were viewed as one-off events and responded to by governments and relief agencies without taking into account the social and economic implications and causes of these events. Gradually, this approach changed to an emphasis on preparedness measures, such as stockpiling of relief goods, preparedness plans and a growing role for non-government agencies. This "contingency planning" approach helped improve handling of disruptive events.

In the 1990s, disaster risk management emerged. This approach had three distinct but interrelated components: hazard assessment, vulnerability analysis and enhancement of management capacity. Under this model, disasters were no longer viewed as extreme events created entirely by natural forces. This model recognised that physical, social and economic risks left unmanaged or mismanaged for a long time contributed to the occurrence of disasters (Yodmani, 2007).

Factors such as the 2001 attack on the World Trade Centre and anthrax attacks influenced a shift from disaster risk management to the all-hazards planning approach. It was a more efficient and effective way to prepare for a broader range of emergencies and disruptions. Rather than managing planning initiatives for a multitude of threat scenarios, the all-hazards approach focuses on developing capacities and capabilities that are critical to preparedness for a full spectrum of emergencies or disasters.

This all-hazards approach has generally been effective although it has lacked a contextual framework and does not necessarily entrench ongoing capacity for change because it relies for the most part on pre-determined response plans. As noted by Waugh (2004), all-hazards does not literally mean being prepared for any and all hazards that might manifest themselves in a particular community, state or nation. In his view, it means there are things that commonly occur in many kinds of disasters, such as the need for emergency warning or mass evacuation, that can be addressed in a general plan, which can provide the basis for responding to unexpected events.

By contrast, the capacity to adapt, anticipate, deal with change and continue to develop is a fundamental tenet of resilience. It has evolved as we progressively understand the complexity and interconnectedness of organisations, communities and individuals especially in the context of disruptive events and catastrophic situations.

Embracing an all hazards approach within an overarching framework of resilience is a logical step given the unprecedented set of disruptions and catastrophic events which have increased the challenges of the 21st century. This new paradigm is an enabler of synergies and has a multiplier effect for the allocation and use of resources needed to anticipate, prepare, manage, adapt and survive a disruptive event. This new paradigm encourages the transition from being reactive to proactive and to become adaptive as it offers governments, organisations and communities greater flexibility to deal with changing circumstances.

All-hazards resilience recognises the synergies and relationships which exist and form part of anticipating, adapting to and managing disruptive events and catastrophic situations. It recognises that emergency responders and crisis managers do not operate in isolation. Rather, under the all-hazards resilience paradigm, organisations together with individuals and communities have a clearly defined role before, during and after any type of disruptive event.

Part of the need for adopting all-hazards resilience is to counter the fragmentation within organisation to address disruptions. In many organisations, the approach to dealing with operational risks is to separate responsibility across different entities for different situations, hazards and even disruptions. As a result each area has its own priorities, separate resources are used to address a disruptive situation, and there is limited coordination between areas.

Organisations are potentially vulnerable when work units develop as silos or stove pipes as they become isolated from other areas and lose sight of the organisation's vision. In some instances, these units generate their own culture and vision which may not be in the best interests of the overall organisation. Duplications and inefficiencies result when the organisation does not work as an integrated system linked to the community it serves. Silos can be created around an individual, a group, a division, a function, or even a product line or service, or a hazard response area. Wherever it is found, silo mentality becomes synonymous with power struggles, lack of cooperation, and loss of productivity and flexibility. The resultant effect is that any benefits to the overall society are diminished or lost.

A resilience framework means that business units, processes and activities are no longer operating in isolation of each other or their community. It brings them together to sit at the very centre of an organisation's ethos and way of operating, which ultimately contributes to societal resilience. The foundation of a successful all-hazards resilience approach demands that we confront workplace silos of expertise and address the issues associated with our increased global connectedness. Silos erode this foundation.

5. A WORLD OF DISRUPTIONS

The changing global social, cultural and political environment has been impacted by the additional challenges of terrorism, piracy, threats to energy and supply chains, political instability, climate change, and population shift. Recent political instability in the Middle East and Africa has had an impact across the globe on oil and share prices, trends in air travel, as well as localised population shifts. Natural disasters alone are now four times higher than in the 1970s (Oxfam, 2007). Two thousand people are killed in disasters each month (Arbon, 2010). That is the equivalent of six 747 aircrafts crashing each month. True catastrophes, on the scale of the 2010 floods in Pakistan, thankfully, are rare. Those floods resulted in 21 million people injured or homeless, 20 % of Pakistan's total land area submerged under water, extensive damage to infrastructure, and an estimated economic impact equal to one third of its GDP. The situation was further compounded by disease and increased activity by the Taliban.

The Pacific Ocean Ring of Fire is an area where a large number of volcanic eruptions and earthquakes occur with approximately ninety percent of the world's earthquakes and eighty percent of the world's largest earthquakes (USGS, 2009). Australia and New Zealand have recently experienced unprecedented disruptions. Floods in the Australian state of Queensland covered an area the size of France and Germany combined, while the earthquake which reduced much of the city of Christchurch in New Zealand to rubble reportedly brought an estimated 200,000 tonnes of silt to the surface and face masks were issued to citizens (RNZ, 2011). The magnitude of the local and global, and social and economic impacts of the earthquake and tsunami in Japan and the subsequent nuclear emergency has yet to be measured.

Over the past few years, there have been various emergencies and major disruptive events of one sort or another that may not have been of the magnitude of the Pakistan floods or the earthquake in Haiti in 2010, or the attacks on the World Trade Centre in 2001, but which still have significant impact on the ability of those affected to go about their daily lives and which test the resilience of the communities and organisations affected and often, the nation. The impact extends to how safety and security issues are viewed and each of these disruptive events has provided many lessons to learn, develop and improve effective all-hazards resiliency.

6. LESSONS FROM PAST DISRUPTIONS

A key component of this new paradigm is learning lessons from past disruptions and this can lead to the adoption of best practices which contribute to all-hazards resilience.

In almost every instance of successful response to a crisis or disruption, management and response activities consisting of sound operating execution coupled with superior communication predominate. Practised operational response is essential. It saves lives, property and other assets. The ability to communicate is no less important. All-hazards resilience is inclusive and not confined to an elite team of disaster experts. Resilience recognises the critical importance of organisations, social groups and individuals in dealing with the unexpected and this recognition is embraced in all-hazards resilience.

One of the most recent examples of changing communications in disasters in the 21st century comes from the Ushahidi Project during the 2010 Haiti earthquake and the use of social media. In that case, emergency radio broadcasts directed victims who were stranded and without other means of communications to send a text message of their emergency needs. Ushahidi Platform is a tool to crowd-source information using multiple channels, including SMS, email, Twitter and the web; it was used to produce an interactive map during the recent Australian floods in the northern state of Queensland (Ushahidi, 2011). The changing cultural and social environment means that social media now has a role in emergencies and disruptive situations. Social media is a resource which has yet to be fully harnessed to assist in anticipating, managing and surviving disruptions, but which offers considerable potential to contribute to all-hazards resilience.

Among the identified and recurring reasons why governments and organisations are not effective in dealing with disruptions are failures of communications systems, inefficiency in deploying resources, and fractured command and control structures. Hurricane Katrina, which devastated the city of New Orleans, provides a good example. In a media conference in February 2006 to release the White House report of the lessons learned from that major disruption, Frances Townsend, Assistant to the President for Homeland Security and Counter Terrorism, noted the key lessons as planning, resource management, evacuation, situational awareness, communications and coordination (Donahue & Tuohy, 2006).

Command and control is often cited as a problem in disruptions and catastrophic events. The ideal scenario is that everyone uses the same system and terminology when dealing with a disruptive event. In theory, this allows disparate groups, organisations and communities to come together quickly and avoid miscommunication during heightened periods of potential confusion such as during disasters. Nonetheless, as first responders are often not trained emergency workers but instead, friends and neighbours, the command, control and communication issues are often confused amidst the desire to help. Even when formal response mechanisms are involved, such as during Hurricane Katrina in 2005, command and

control structures are often fractured with overlapping roles and responsibilities (Townsend, 2006). Learning is a process of growth, as a successful learning process requires commitment to change. This is not to suggest that change and learning are synonymous. We need to learn, unlearn and relearn to move forward and not repeat the same mistakes. Part of that process is that lessons must be implemented to achieve all-hazards resilience.

The changing risk environment means that plans and people need to be flexible, adaptive and aware of ongoing changes in their environment. Situational awareness is a factor highly relevant to all-hazards resilience. It is a necessary attribute to anticipate changes or anomalies which could provide information about a potential disruption and by acting on it in order to minimise or avoid a serious impact. A lack of situational awareness has been identified as one of the primary factors in accidents attributed to human error (Nullmeyer *et al.*, 2005). Too often, anomalies are either ignored or dismissed as irrelevant, and this results in the normalisation of the abnormal, often with detrimental effects.

7. EXERCISES AS A TOOL TO ACHIEVE ALL-HAZARDS RESILIENCE

Planning is an important tool to assist with any potential or actual disruption. However, it takes more than just having a plan to survive a disruptive event. Planners play an important role in the design of exercises to test plans and implement lessons to ensure they are targeted with clear goals and objectives, and achieve a balance between what is known and what is unknown. The use of exercises is a major tool to build capacity for all organisations and communities to achieve an all-hazards resilience. A way to accomplish this is through the development of exercises which allow participants to demonstrate skills, knowledge and capabilities, and which extend their capacity for further learning.

Collaborative planning and building relationships between all stakeholders is part of building resilience. Everyone involved needs to know and understand their role before a disruption, any type of disruption, occurs. This means plans must be tested to demonstrate if they are workable, relevant and reliable. The next critical step is to ensure that the lessons are in fact implemented. Otherwise mistakes will be repeated, incident after incident.

While there is a need for common understanding, in times of stress particularly during a fast moving disruptive event, there can be a natural desire to reduce that stress by increasing group harmony, and ignoring or minimising problems. The 1986 Space Shuttle Challenger disaster was attributed to the failure of the O-rings, due to the unrelenting pressure to meet the demands of an accelerated flight schedule, leading managers to ignore recommendations by the engineers (Rogers *et al.*, 1986). It was a notable example of group-think, which is described by Janis (1972) as "*a mode of thinking that people engage in when they are deeply involved in a cohesive in-group, when the members' strivings for unanimity override their motivation to realistically appraise alternative courses of action*". When people are in groups, there is an overall tendency towards a shift in risk perception. People in groups make decisions about risk differently from when they are alone. In the group, their risk appetite may change and they may make riskier decisions, particularly during disruptive events because the shared risk makes the individual risk less.

8. TRAINING AND EXERCISES

Response is always better when the responders are prepared and training is a major part of response preparation. All-hazards resilience offers an inclusive approach and does not limit responders to safety and security personnel or emergency workers. Instead, it implicitly and explicitly recognises and includes engagement of all individuals in the affected communities and organisations.

The key to learning lessons is through inculcating an environment of learning through training and exercises which improve performance and implement changes rather than exercises which simply repeat familiar processes. If this does not happen, then lessons are not leaned, they are simply observed. Too often, considerable resources are used to create a plan and to test it, but while identifying lessons is relatively straightforward, true learning is much harder. Too often, lessons tend to be observed and remain isolated and perishable rather than incorporated and absorbed into the culture of the organisation and community.

Each disruptive event is unique, yet solutions to them have some common elements and the integration of planning, training, exercises and implementing lessons is an important practise to achieve all-hazards resilience. A very real consequence of failing to learn lessons is future loss of lives, property and assets.

9. CONCLUSION

The all-hazards resilience paradigm reflects the changing needs of the 21st century in the face of the increasingly complex challenges presented by the unprecedented natural, accidental and intentional disruptions. It offers governments, communities and organisations a comprehensive convergence of two relevant models to address disruptive and sometimes catastrophic events. All-hazards resilience goes beyond preparation and response to embrace the need to be alert and to anticipate abnormalities which indicate potential disruptions. It offers economies of scale and reduced duplication of effort by enabling development of sufficiently flexible and adaptive capabilities, and actively builds on lessons to ensure they are learned and implemented. In this way, it discourages normalising the abnormal. It breaks down traditional silos by connecting crisis managers and emergency responders in the matrix of relationships between organisations, communities and individuals, and builds on those synergies before, during and after any type of disruptive event. All-hazards resilience is the paradigm for the future management of disruptive events which impact communities, organisations, individuals and nations.

REFERENCES

Arbon, P. (2010). A framework for disaster resilient communities. *National Security Science & innovation Conference*, 23rd September 2010, Canberra, Australia.

Donahue, A.K. & Tuohy, R.V. (2006). Lessons we don't learn: A study of the lessons of disasters, why we repeat them, and how we can learn them. *Homeland Secur. Affairs*, **2**: 1-28.

Department of Homeland Security (DHS) (2006). *National Infrastructure Plan*. US Department of Homeland Security (DHS), Washington D.C.

Institute for Crisis, Disaster, and Risk Management (ICDRM) (2007). *ICDRM/GWU Emergency Management Glossary of Terms*. Institute for Crisis, Disaster, and Risk

Management (ICDRM), George Washington University (GWU).
Janis, I.L. (1972). Victims of Groupthink. Houghton Mifflin Company, Boston.
Nullmeyer, R.T., Stella, D., Montijo, G.A., & Harden, S.W. (2005). Human factors in air force flight mishaps: Implications for change. *Proceedings of the 27th Annual Interservice / Industry Training, Simulation, and Education Conference*, National Training Systems Association, Arlington, Virgnia.
Oxfam (2007). *Climate Alarm: Disasters Increase as Climate Change Bites*. Oxfam, Cowley, Oxford.
Radio New Zealand (RNZ) (2011). *Radio New Zealand*. Available online at: http://www.radionz.co.nz (Last access date: 2nd March 2011).
Rogers, W.P., Armstrong, N.A., Acheson, D.C., Covert, E.E., Feynman, R.P., Hotz, R.B., Kutnya, D.J., Ride, S.K., Rummel, R.W., Sutter, J.F., Walker, A.B.C., Wheelon, A.D., Yeager, C. & Keelm A.G. (1986). *Report of the Presidential Commission on the Space Shuttle Challenger Accident*. Presidential Commission on the Space Shuttle Challenger Accident Report, Washington D.C.
Townsend, F.F. (2006). *The Federal Response to Hurricane Katrina Lessons Learned*. US Government, Washington D.C.
US Geological Survey (USGS) (2009). *Earthquakes FAQ*. US Geological Survey (USGS), U.S. Department of the Interior, Washington D.C.
Waugh, W.L.J. (2004). Terrorism and the all-hazards model. *IDS Emergency Management On-Line Conference*, 28th June-16th July 2004.
Ushahidi (2011). *Ushahidi*. Available online at: http://www.ushahidi.com (Last access date: 7th March 2010).
Yodmani, S. (2001). Disaster risk management and vulnerability reduction: protecting the poor. *Asia Pacific Forum on Vulnerability*, February 2001, Manila.

PROPOSAL OF THE PROTOTYPE RoSyD-CBRN, A ROBOTIC SYSTEM FOR REMOTE DETECTION OF CBRN AGENTS

Andrea Malizia[1*], Riccardo Quaranta[1], Roberto Mugavero[2], Riccardo Carcano[3] & Giuliano Franceschi[4]

[1]Department of Mechanical Engineering, Faculty of Engineering, University of Rome "Tor Vergata", Italy
[2]Department of Electronic Engineering, Faculty of Engineering, University of Rome "Tor Vergata", Italy
[3]B.M.D s.p.a, Tivoli Terme (RM), Italy
[4]Oto Melara s.p.a, La Spezia, Italy

*Email: malizia@ing.uniroma2.it

ABSTRACT

In this work, a prototype robotic system is proposed to avoid direct exposure of responders and permit remote detection of CBRN agents. The system, is named by the acronym RoSyD-CBRN (Robotised System to Detect CBRN agents), basically consists of two functional areas which interact and communicate with each other; a mobile system (robot) and a remote station. Suitable first alarm, identification, and identification and first alarm CBRN detectors are chosen for the robot and remote station. In addition, suitable meteorological detectors are chosen to obtain the environmental parameters that are necessary to launch simulation with the predictive software (such as NBC-Analysis) in order to provide safe routes for the responders and the population. The conceptual work scheme of the robot is divided into three phases; Phase 1: Launch of the robot; Phase 2: Detection and data transmission; Phase 3: Robot returns and sample analysis in the laboratory. On the whole, the prototype integrates into a single architecture all the components that at present, in the case of CBRN events, operate separately or merged partially, but not totally cooperating with a high degree of automation as in the proposed system.

Keywords: *Chemical, Biological, Radiological and Nuclear (CBRN) agents; robot; remote station; CBRN detectors; meteorological detectors.*

1. INTRODUCTION

Chemical, Biological, Radiological and Nuclear (CBRN) risks are caused by the diffusion of these substances in the environment, causing serious damages to persons and things (DOA, 1996a). The accidents connected with these types of substances can be either due to man, in the event of industrial accidents, road accidents, human error in process, manipulation, transport and / or storage of dangerous materials and substances, or to natural causes, when the structures where these substances are produced or stored are damaged by natural events (earthquakes, flood, etc.) (DOA, 1988). In other cases, war or terrorism, man voluntarily determines the spread of CBRN agents. In any of these cases, one of the main problems related to this type of event is the capability of responders to effectuate detection in safe condition (TMCTL, 1998; DOA, 1996b).

In this work, a prototype robotic system is proposed to avoid direct exposure of responders and permit remote detection of CBRN agents. The system basically consists of two functional areas which interact and communicate with each other:

i. The first consists of a **mobile system (robot)** that can perform:

   - Automatic detection of CBRN agents.
   - Transmission of data to the remote station.
   - Collection and transport of samples (air-water-soil) from the contaminated area to the remote station.

ii. The second is the **remote station** (NATO, 2005), housed, for example, on a vehicle of the First Responders Team, which interacts with the robot and is equipped for:

   - Qualitative analysis of samples taken on the contaminated site by means of a mobile laboratory (IAEA, 2003, 2005; Lazcka *et al.*, 2007).
   - Real-time simulation in order to map the contaminated area by the evaluation of diffusion routes of CBRN agents (IAEA, 2004).
   - Driving the mobile unit.
   - Controlling the sensors on board the robot.
   - Sending information.

The innovative aspect of the project is the integration into a single architecture of all the components that at present, in the case of CBRN events, operate separately or merged partially, but not totally cooperating with a high degree of automation as in the proposed system.

The system is named by the acronym RoSyD-CBRN (Robotised System to Detect CBRN agents). Figure 1 shows a functional architecture that highlights the main components of the system.

2. CBRN DETECTORS PROPOSED

The CBRN detectors have been divided into three categories (Figure 2):

i. First Alarm
ii. Identification
iii. Identification and first alarm.

In order to pursue the objectives for the robot, it is proposed to use first alarm, or first alarm and identification detectors which have small dimensions and weight, and the capability to automatically transmit data. For the remote station, it is proposed to use identification, and first alarm and identification detectors in order to do detailed analyses of air, soil and water samples. The detectors used for the robot and remote station are summarised in Table 1, with their main characteristics shown in Tables 2 to 7.

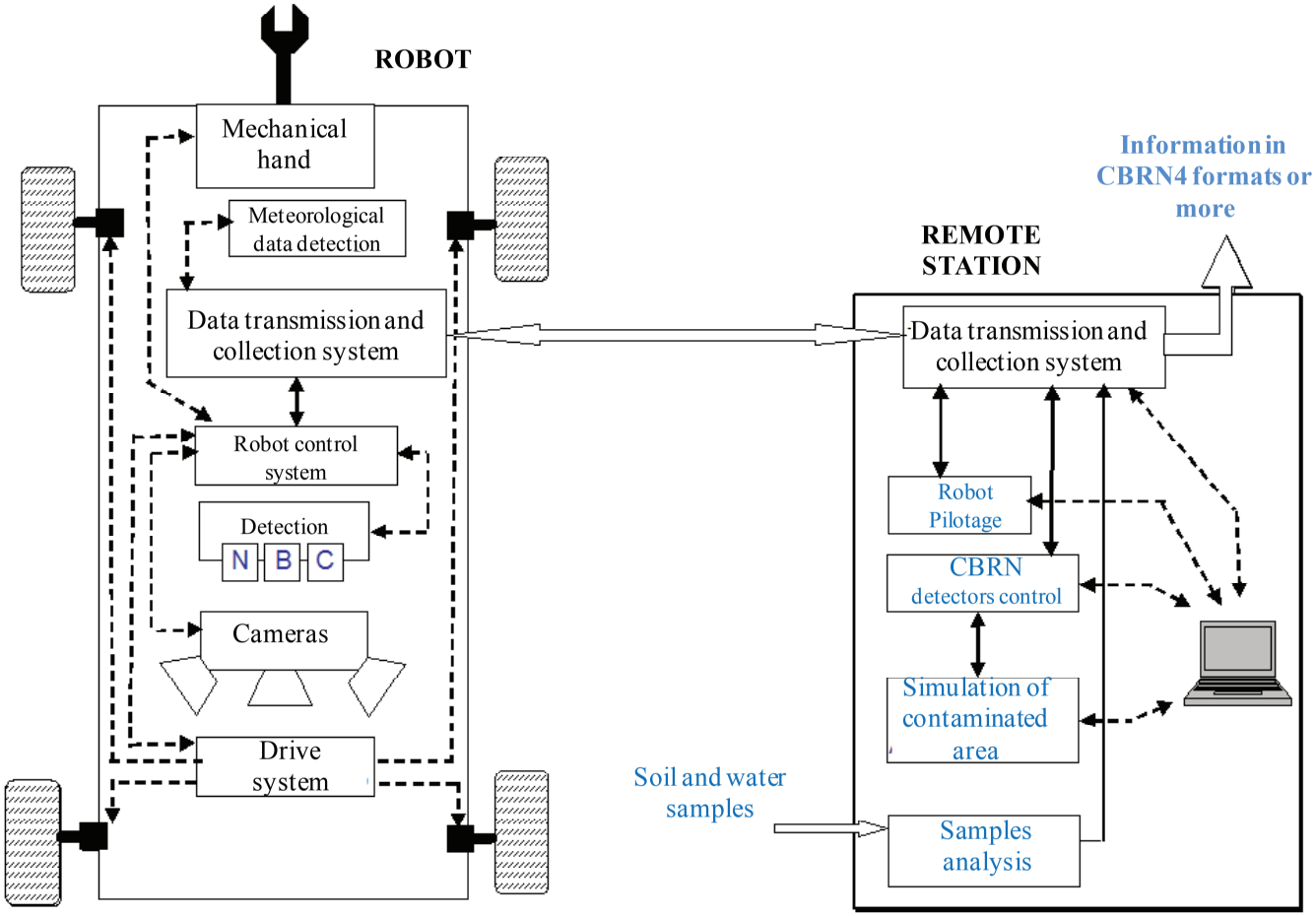

Figure 1: The RoSyD-CBRN conceptual scheme.

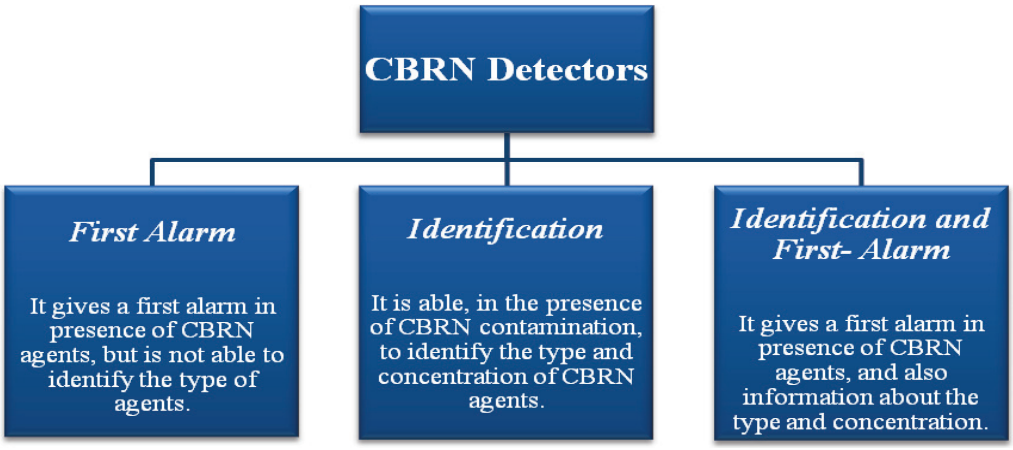

Figure 2: CBRN detectors family (DOA, 2002).

Table 1: CBRN detectors used for the robot and remote station.

Detector	Robot	Remote Station
R-N	Radiation dosimeter	Geiger Muller detector that works with an extension that allows the control of samples taken by the robot before the samples are introduced inside the remote station
C	Photo ionisation detector (PID) sensor	Gas Chromatography-Mass Spectrometry (GC-MS) type
B	Trigger detector	Polymerase chain reaction (PCR)

Table 2: Main characteristics of the R-N detector for the robot.

Radiation detectable	Accuracy	Response time	Principle of work and characteristics	Implementation	Detector Category	Advantages	Disadvantages
Gamma ray, neutron	5 cGy to 10 cGy	10 sec to 24 h	Semiconductors Dimension: 80.4 x 48 x 9 mm Weight: 56 g	Robot - Remote station	First Alarm	Reduced dimensions	Slow response time

Table 3: Main characteristics of the R-N detector for the remote station.

Radiation detectable	Accuracy	Response time	Principle of work and characteristics	Implementation	Detector Category	Advantages	Disadvantages
Gamma and beta ray	1 mSv to 10 Sv	< 1min	Geiger Muller Dimensions: length: 92 cm to 4.25 m; width: 13 cm	Remote station	Identification-First Alarm	Allow measurements at safety distance	It is not remotely handled

Table 4: Main characteristics of the C detector for the robot.

C agents detectable	Accuracy	Response time	Principle of work and characteristics	Implementation	Detector Category	Advantages	Disadvantages
Oxygen	0-30%	30 s – 1 min	PID sensor Dimensions: 11.8 x 7.6 x 4.8 cm Weight : 454 grams with battery	Robot	Identification-First Alarm	A lot of agents detectable High accuracy	Slow response time
Combustible Gas	0-100% LEL						
VOCs	0-200 ppm 200-2000 ppm						
CO	0-500 ppm						
Hydrogen Sulfide	0-100 ppm						
Sulfur Dioxide	0-20 ppm						
Nitric Oxide	0-250 ppm						
Nitrogen Dioxide	0-20 ppm						
Chlorine	0-10 ppm						
Hydrogen Cianide	0-100 ppm						

Table 5: Main characteristics of the C detector for the remote station.

C agents detectable	Accuracy	Response time	Principle of work and characteristics	Implementation	Detector Category	Advantages	Disadvantages
All	Few ppb	20s - 1 min	GC-MS Weight:18 kg Dimensions: 46 cm x 43 cm x 18 cm ;	Robot- Remote station	Identification- First Alarm	A lot of C agents detectable	Database preparation

Table 6: Main characteristics of the B detector for the robot.

B agents detectable	Accuracy	Response time	Principle of work and characteristics	Implementation	Detector Category	Advantages	Disadvantages
All	Few ppb	0-5 min	LIDAR	Remote station	First Alarm	A lot of C agents detectable and high accuracy	False alarms

Table 7: Main characteristics of the B detector of the remote station.

B agents detectable	Accuracy	Renponse time	Principle of work and characteristics	Implementation	Detector Category	Advantages	Disadvantages
Bacillus anthracis	ppb	30 min	PCR	Robot	Identification	Accuracy	Slow response time No all agents detectable
***Brucella* species**							
Francisella tularensis							
Yersinia pestis							
***Clostridium botulinum* Type A**							
Listeria monocytogenes							
Escherichia coli							

3. METEOROLOGICAL DETECTORS PROPOSED AND SOFTWARE

The meteorological detectors have been divided into three categories (Figure 3):

i. Wind
ii. Temperature
iii. Humidity.

The use of these instruments on the robot makes it possible to obtain the environmental parameters that are necessary to launch simulation with the predictive software (such as NBC-Analysis) in order to provide safe routes for the responders and the population.

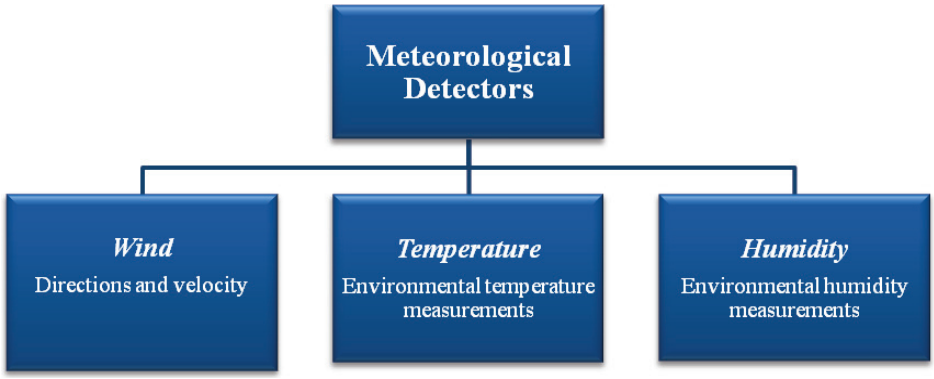

Figure 3: Meteorological detectors family.

4. MAIN CHARACTERISTICS OF THE REMOTE STATION

The station for remote management and data reception / transmission must be:

i. Equipped with:
   - A guidance system (e.g., joystick)
   - SRS-232 serial ports, USB 2.0 and FireWire.

ii. Prepared for internet connection and data transmission.
iii. Compatible with the installation of specific software to control the robot instrumentations.

The remote management station of the robot, and data reception and transmission must be allocated in a mobile laboratory equipped with:

i. Laboratory equipment for analysis of air, water and soil samples.
ii. Software that takes as input weather data, the robot's position and the first measurement of the robot, allowing for improvement to the simulation.
iii. Dry power inhalers (DPI) for responders.
iv. Decontamination systems for responders and hardware systems.

Based on the above requirements, the Iveco One firetruck (Figure 4), used by the Italian Fire Brigade, has been chosen as the remote station.

Figure 4: The Iveco One firetruck.

5. MAIN CHARACTERISTICS OF THE ROBOT

The robot must be equipped with:

i. Wheels or tracks, or a combination of both, to ensure mobility on any terrain and even within urban areas (overcoming speed bumps, humps, steps, etc.).
ii. Electric motor and rechargeable batteries that feed both the motor and in-vehicle systems.
iii. A CCD camera capable of transmitting images, even in poor visibility conditions (darkness, rain, fog, smoke, etc.). It will allow a panoramic view of the area covered by the robot, and that the area in front of the point where the responder decides to perform specific operations (read point values of contamination detected, sampling, etc.).
iv. IR / thermal camera.
v. A GPS satellite receiver.
vi. Sensors to detect the direction and speed of wind, and temperature and humidity.
vii. Apparatus for detection/identification of Chemical Warfare Agents (CWA), Biological Warfare Agents (BWA), Radiological Warfare Agents (BWA) and Industrial Toxic Components (ICT), where possible, will be the same type.

6. PROPOSED PROTOTYPE

The proposed prototype has a conceptual work scheme divided into three phases (Figure 5):

Phase 1: Launch of the robot
Phase 2: Detection and data transmission
Phase 3: Robot returns and sample analysis in the laboratory.

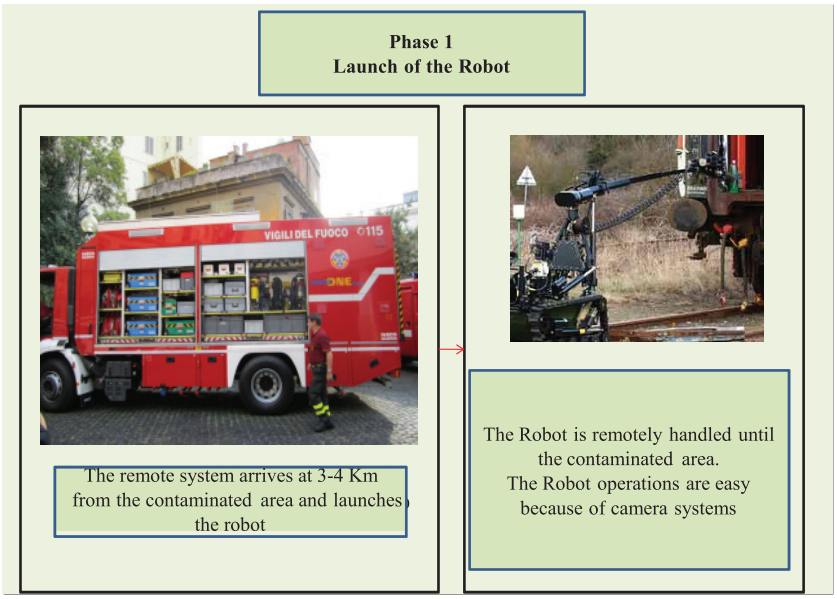

(a)

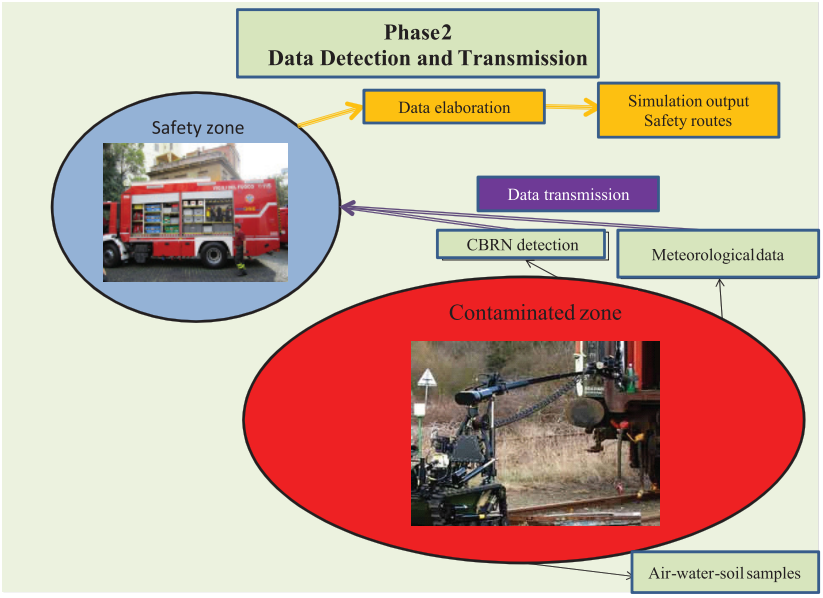

(b)

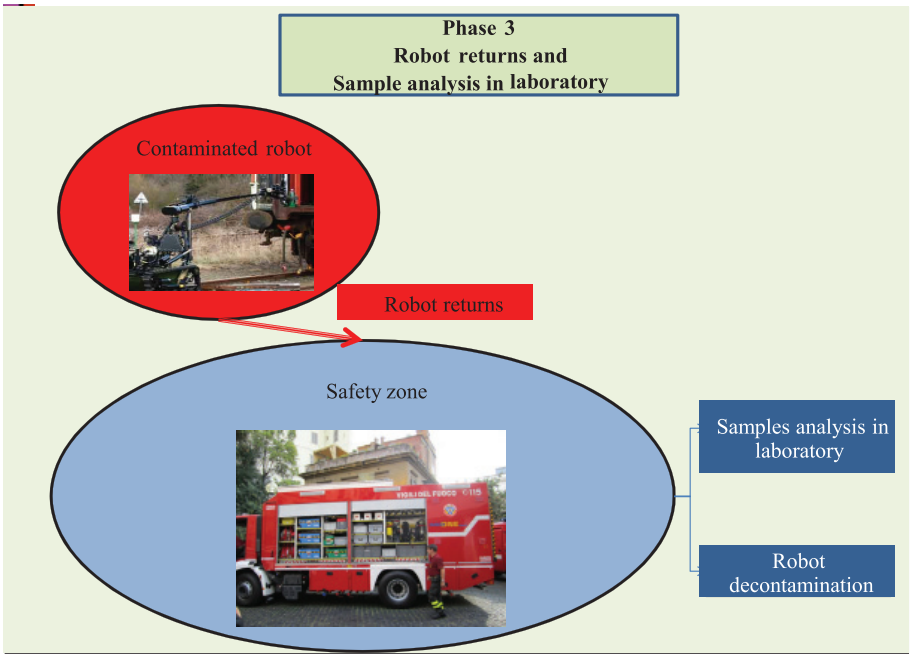

(c)

Figure 5: Conceptual work scheme of the prototype: (a) Phase 1: Launch of the robot. (b) Phase 2: Detection and data transmission. (c) Phase 3: Robot returns and sample analysis in the laboratory.

7. CONCLUSION

In conclusion, the following main objectives have been achieved:

Mobile system (robot):

1. Acquisition of data concerning CBRN contaminants detected.
2. Acquisition of data regarding weather conditions.
3. Transmission of the environmental situation in order to facilitate driving of the vehicle using a camera system.
4. Collection of samples (air, water and soil) using a robotic arm controlled remotely.
5. Data transmission to the laboratory in the remote station.
6. Control of the CBRN sensors.

Remote station:

1. Data exchange with the robot.
2. Positioning and guidance on predetermined routes and points, or through direct view of the surrounding environment from the acquired images.
3. Data acquisition from external sensors, placed on the robot.
4. Analysis of samples (soil, air and water) collected by the robot.
5. Production of maps that show the spread of CBRN contaminants and help identify

safe routes to allow the optimisation of responder operations.

On the whole, in addition to similar CBRN detection systems in the market today, all the technologies that can be used to develop this prototype have been analysed. On the basis of this analysis, a choice of technologies and their architecture that optimises the system has been proposed in terms of response reliability and speed, easy exchange of information, and safety of responders.

REFERENCES

Department of the Army (DOA) (1988). *FM 21-11: First Aid for Soldiers*. Department of the Army (DOA), Washington D.C.

Department of the Army (DOA) (1996a). *FM 3-4: NBC Protection*. Department of the Army (DOA), Washington D.C.

Department of the Army (DOA) (1996b). FM 8-9: *NATO Handbook on the Medical Aspects of NBC Defensive Operations*. Department of the Army (DOA), Washington D.C.

Department of the Army (DOA) (2002). *FM 4-02.7: Health Service Support in a Nuclear, Biological, and Chemical Environment*. Department of the Army (DOA), Washington D.C.

International Atomic Energy Agency (IAEA) (2005). *RS-G-1.9: Categorization of Radioactive Sources*. International Atomic Energy Agency (IAEA), Vienna.

International Atomic Energy Agency (IAEA) (2004). *Code of Conduct on the Safety and Security of Radioactive Sources*, International Atomic Energy Agency (IAEA), Vienna.

International Atomic Energy Agency (IAEA) (2003), *Method for Developing Arrangements for Response to a Nuclear or Radiological Emergency* International Atomic Energy Agency (IAEA), Vienna.

Lazcka, O., Del Campo, F.J. & Munoz, F.X. (2007). Pathogens detection: A perspective of traditional methods and biosensor. *Biosens. Bioelectron.*, **22**: 1205-1217.

North Atlantic Treaty Organization (NATO) (2005). STANAG 4632: Deployable NBC Analytical Laboratory. North Atlantic Treaty Organization (NATO), Brussels.

The Militarily Critical Technologies List (TMCTL) (1998). *Part II: Weapons of Mass Destruction Technologies*. Office of the Under Secretary of Defense for Acquisition and Technology, Washington D.C.

REKABENTUK DAN PEMBANGUNAN SEBUAH KENDERAAN ROBOTIK BAWAH AIR (*REMOTELY OPERATED VEHICLE*)

Nur Afande Ali Hussain[1], Fadzli Ibrahim[2], Norazlina Md Nasuddin[1], Rosdi Yaacob[1], Hasril Mohd Naim[3], Nor Emi Salwani Sulaiman[1], Rozi Ramli[1], Mohd Ridzuan Mohd Rashid[1], Idayu Ramle[1], Ayu Shahida Ismail[1], Elizabeth Louisnaden[1] & Nor Alyani Ibrahim[1]

[1]Bahagian Teknologi Maritim (BTM), Institut Penyelidikan Sains dan Teknologi Pertahanan (STRIDE), Kementerian Pertahanan, Malaysia
[2]Bahagian Teknologi Jentera dan Aeroangkasa (BTJA), Institut Penyelidikan Sains dan Teknologi Pertahanan (STRIDE), Kementerian Pertahanan, Malaysia
[3]Pusat Penyenyapan Kapal (PPK) Tentera Laut Diraja Malaysia (TLDM), Malaysia

[*]E-mail: afande.hussain@stride.gov.my

ABSTRAK

Objektif kajian ini adalah untuk membangunkan sebuat platform robotik bawah permukaan air (remotely operated vehicle (ROV)) bagi tujuan pemantauan dan pemeriksaan bawah permukaan air, khususnya bagi membantu sebarang operasi yang dijalankan oleh pihak Tentera Laut Diraja Malaysia (TLDM). Rekabentuk struktur ROV, yang mengambilkira kesesuaian saiz, berat dan kedudukan komponen-komponen yang akan diintegrasikan, telah dijalankan dengan menggunakan perisian Solidworks 2009. Kesemua perkakasan elektronik serta penderia menerima bekalan kuasa daripada 2 unit bateri lead acid. Sistem kawalan navigasi ROV yang dibangunkan terdiri daripada dua bahagian utama, iaitu sistem kawalan jauh dan sistem kawalan navigasi. Sistem kawalan jauh terdiri daripada sebuah komputer riba dan joystick, manakala sistem kawalan navigasi di dalam ROV pula terdiri daripada sebuah microcontroller, sebuah depth sensor, sebuah magnetic compass, 4 buah thruster dan 2 buah kamera bawah air. Keseluruhan sistem tersebut diintegrasikan dengan menggunakan perisian LabView 8.5. Pengujian tahap integrasi di makmal serta pengujian tahap kefungsian di lapangan telah membuktikan yang ROV ini adalah sesuai untuk operasi ketenteraan dan aplikasi komersial. Walaubagaimanapun, projek ini perlu diteruskan ke arah pembangunan sebuah platform robotik bawah permukaan yang lebih sofistikated dengan pelbagai ciri tambahan lain bagi meningkatkan tahap pengoperasian ROV tersebut.

Kata Kunci: *Remotely operated vehicle (ROV); struktur kerangka; sistem kawalan dan komunikasi; sistem pendorongan; integrasi sistem.*

1. PENGENALAN

Teknologi kenderaan robot bawah-air atau lebih dikenali sebagai *unmanned underwater vehicle* (UUV) merupakan salah satu bidang teknologi yang memainkan peranan penting dalam aplikasi maritim pada masa kini, khususnya untuk tujuan pengawasan dan pemeriksaan. Teknologi ini mempunyai tahap keupayaan yang tinggi untuk menjalankan pelbagai tugas bukan hanya untuk tujuan komersial dan industri, malah juga untuk operasi ketenteraan (Yuh, 2000; Molland, 2008).

Antara contoh aplikasi teknologi UUV yang begitu meluas digunakan sekarang ialah pemeriksaan struktur binaan bawah laut, pemeriksaan keadaan persekitaran bawah laut, pengesanan lokasi, pemetaan, pengumpulan maklumat, malah turut digunakan juga bagi tujuan perisikan ketenteraan. Secara tidak langsung, penggunaan sistem robot seumpama ini dapat mengurangkan tahap risiko bahaya terhadap manusia dalam operasi tertentu dan seterusnya dapat mengurangkan kos operasi serta meningkatkan tahap ketepatan tugas rutin (Lygouras *et al*., 1998; Yuh, 2000; Molland, 2008).

Secara amnya, terdapat dua jenis UUV iaitu *remotely operated vehicle* (ROV) dan *autonomous underwater vehicle* (AUV). ROV merupakan kenderaan robot yang dikawal secara langsung oleh operator di stesen permukaan melalui kabel kuasa dan komunkasi, manakala AUV pula dikawal tanpa menggunakan sebarang kabel (Frost *et al*., 1996; Molland, 2008).

Pada masa ini, Tentera Laut Diraja Malaysia (TLDM) telah pun mempunyai beberapa model ROV seperti PAP 109 yang digunakan oleh Skuadron *Mines Countermeasure Vessel* (MCMV) dan juga Benthos yang digunakan oleh KD Duyong. Walau bagaimanapun, peralatan ini merupakan teknologi masa lampau yang sukar untuk disenggara, mempunyai tahap operasi yang agak terbatas, dan memerlukan tahap kepakaran serta kos yang tinggi untuk pengoperasian (Jamian, 2009).

Ini menunjukkan bahawa adalah amat penting kajian ini menepati keperluan operasi sebenar TLDM, contohnya seperti operasi ant-periuk api oleh skuad penyelam ranjau Skuadron MCMV. Oleh yang demikian, pembangunan platform ini diharap dapat membantu pihak TLDM pada masa akan datang. Penggunaan platform robotik bawah permukaan merupakan aplikasi yang dapat memudahkan pemantauan bawah laut secara efektif oleh pihak tentera seperti (Mahoney *et al.*, 2009; Muljowidodo *et al.*, 2010)

Secara amnya, objektif kajian ini adalah untuk membangunkan sebuah kenderaan robot bawah-air yang hibrid serta tahan lasak untuk aplikasi saintifik dan ketenteraan, dan seterusnya, membuktikan kesesuaian teknologi tersebut untuk aplikasi industri dan juga komersial. Objektif khusus kajian pula adalah untuk membangunkan sebuah ROV yang mempunyai keupayaan terapung, tenggelam, menyusur, berputar dan bergerak kembali bagi tujuan meneroka dan memantau ruang bawah permukaan laut. ROV yang ingin dibangunkan seharusnya mempunyai ciri-ciri berikut:

i. Bahan yang tahan karat, terutamanya terhadap air laut yang berkemasinan tinggi (*high salinity*).

ii. Rekabentuk hidrodinamik, iaitu kebolehan menyelam ke dasar laut dan mudah bergerak (Alvarez *et al*., 2009).

iii. Mempunyai kerangka yang kuat, teguh dan tahan lasak, sesuai dengan keadaan persekitaran serta kedalaman laut.

iv. Mampu merentasi ruang-ruang kecil, contohnya di celah-celah kapal karam dan terumbu yang kecil dan sempit.

v. Berkuasa untuk menentang arus laut dalam pergerakan yang perlahan dan tepat untuk merekod, merakam imej, mengesan serta memeriksa keadaan persekitaran (akustik, suhu dan daya magnetik).

vi. Jelas kelihatan di laut atau ketika timbul di permukaan untuk kemudahan pencarian semula (*recovery*).

vii. Keapungan positif (*positive buoyancy*), di mana akan terapung sekiranya tidak beroperasi atau dalam keadaan melahu (*idle*) (Howse, 2009) .

viii. Darjah kebebasan atau *degree of freedom* (DOF) yang tinggi bagi memudahkan pergerakan dalam ruang tiga dimensi (3D) (Presto, 2001).

2. PEMBANGUNAN PROTOTAIP

Secara umumnya, sistem kenderaan ROV ini terbahagi kepada beberapa sub-sistem yang penting iaitu:

i. **Sistem mekanikal:** Struktur kerangka dan binaan badan kenderaan.
ii. **Sistem elektrikal:** Bekalan kuasa, penderia dan sistem pendorongan.
iii. **Sistem kawalan dan komunikasi:** Sistem kawalan kenderaan, dan sistem penghantaran dan penerimaan data dari ROV ke operator dan sebaliknya.

Proses pembangunan bermula dengan menyediakan rekabentuk konsep kenderaan sebelum proses integrasi sistem dilakukan (Rajah 1). Adalah amat penting untuk menentukan kesesuaian parameter mekanikal dengan sistem-sistem lain yang berkaitan, iaitu sistem elektronik, kawalan dan komunikasi, termasuklah dengan mengambil kira kesesuaian saiz, berat dan kedudukan kotak kawalan elektronik, bekalan kuasa, dan juga peralatan elektronik yang lain seperti lampu, kamera dan sonar. Komponen-komponen utama yang digunakan adalah seperti di dalam Rajah 2. Rekabentuk prototaip yang lengkap seterusnya akan diuji di makmal dan juga di lapangan bagi menentukan keseluruhan rekabentuk dan tahap kefungsian setiap sistem berada di tahap yang optimum.

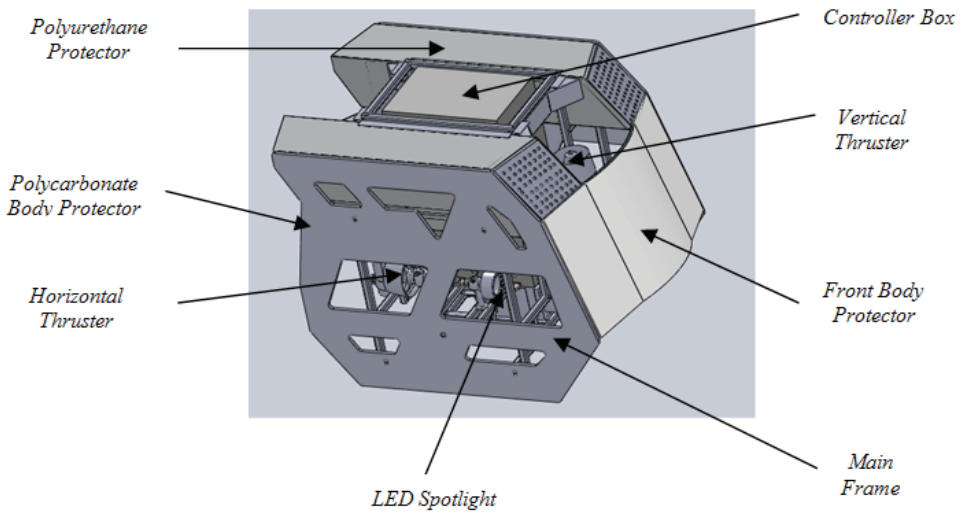

Rajah 1: Rekabentuk konsep ROV.

(a) (b) (c)

(d) (e)

Rajah 2: Perkakasan yang akan dipasang pada kerangka ROV: (a) Sistem pendorongan; (b) Sistem kawalan yang menggunakan *CompactRio*; (c) *GyroCompass* atau pengesan kedudukan; (d) Kamera bawah permukaan jenis *SharkEye* yang berkeupayaan menahan tekanan melebihi 100 m; dan (e) Lampu bawah permukaan jenis LED.

2.1 Sistem Mekanikal

Peringkat awal pembangunan prototaip adalah melibatkan proses rekabentuk struktur kerangka dan binaan badan kenderaan (Rajah 3). Terdapat tiga pilihan utama bentuk binaan untuk merekabentuk kenderaan bawah-air ini iaitu bentuk segiempat, bentuk seperti peluru berpandu ataupun silinder, dan juga bentuk bulat. Setiap konsep binaan badan itu mempunyai kelebihan masing-masing dan bergantung kepada aplikasi yang hendak dilakukan oleh kenderaan bawah-air yang dibina (Ross, 2006).

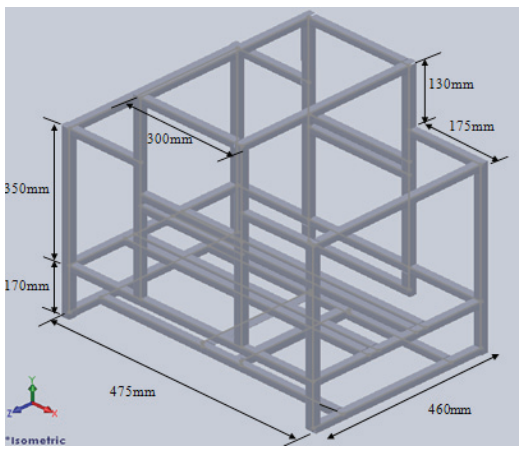

Rajah 3: Cadangan struktur kerangka ROV.

Rekaan berbentuk segiempat dan konsep *open frame* telah dipilih berdasarkan faktor bentuk ini mudah diubahsuai untuk penambahan aksesori seperti lengan robotik dan alat pemotong pada masa akan datang. Konsep *open frame* memudahkan proses-proses meletakkan kedudukan sistem pendorongan, penderia, kamera dan lampu pada struktur ROV dengan hanya menggubah kedudukan *mounting*. Dalam erti kata lain, bentuk segiempat ini memudahkan kerja-kerja fabrikasi dilakukan.

Rekabentuk struktur kerangka utama telah dibina dan disimulasikan menggunakan perisian *Solidworks 2009* (Rajah 4) untuk mengukur dan menganalisa kekuatan struktur utama yang dibina serta kekuatan dan tindakbalas struktur utama terhadap komponen-komponen yang digunakan (Rahim *et al*., 2010).

Dalam aspek pemilihan bahan kerangka pula, faktor-faktor seperti tahan hakisan, keteguhan (*durability*), mampu merentangi halangan di bawah permukaan, tahan tekanan dan boleh diubahsuai mengikut kehendak pengguna, kebolehmesinan yang jitu dan pada kos yang boleh dipertimbangkan telah menjadi elemen penting bagi memastikan kenderaan berada di dalam keadaan berkeupayaan tinggi dan selamat. Antara contoh pilihan bahan bagi mencapai tujuan ini ialah aluminium AL 6061 dan AL 5083 serta keluli tahan karat jenis 304, 308 dan 316. Bahan AL 6061 telah dipilih untuk dijadikan rangka di dalam melaksanakan projek pembangunan ROV ini kerana kesesuaiannya yang tinggi untuk aplikasi marin.

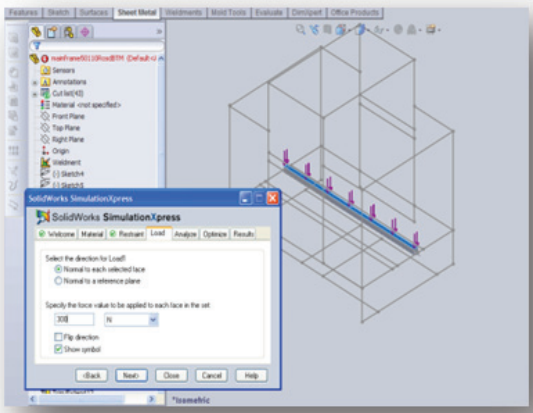

Rajah 4: Rekabentuk kerangka ROV meggunakan perisian *SolidWorks 2009*.

Sebagaimana yang telah dinyatakan, rekabentuk keseluruhan struktur perlu mengambilkira kesesuaian saiz, berat dan kedudukan komponen-komponen yang akan diintegrasikan. Oleh itu, bagi tujuan konfigurasi kedudukan komponen-komponen utama ROV, saiz dan berat setiap komponen telah diukur (Jadual 1), dan berdasarkan kepada analisis kesesuaian kedudukan komponen tersebut, konfigurasi bagi rekabentuk lengkap ROV telah diperolehi (Rajah 5).

2.2 Sistem Elektrikal

Sistem elektrikal ROV terdiri daripada beberapa sub-sistem utama termasuklah:

i. Bekalan kuasa
ii. Kawalan navigasi
iii. Sistem pendorong.
iv. Sistem penderia

ROV yang dibangunkan terbahagi kepada dua bahagian utama iaitu bahagian atas permukaan dan bahagian bawah permukaan air (Rajah 6). Oleh kerana platform tersebut tidak membawa bekalan kuasa sendiri secara *on board*, maka ia perlu dibekalkan dengan bekalan kuasa berterusan dari bahagian atas permukaan melalui kabel kuasa.

Jadual 1: Saiz dan berat bagi komponen-komponen utama ROV.

Komponen	Berat (kg)
Kerangka utama	10
Kotak elektronik	15
4 X *Thruster*	4x0.95
Kamera 1	3.07
Kamera 2	0.75
Gyro Compass	0.465
Depth sensor	1.57
Lampu LED	0.92
NI Controller	2.19
Jumlah	37.8

Pemilihan jenis sumber kuasa pula bergantung kepada rekabentuk binaan badan kenderaan dan jumlah penggunaan kuasa yang digunakan oleh keseluruhan komponen dalam kenderaan. Sumber kuasa elektrik akan disalurkan daripada stesen operasi di daratan atau kapal induk melalui kabel sambungan kepada kenderaan di dalam air. Bateri yang digunakan adalah dari jenis *lead-acid.* Faktor yang menyebabkan bateri daripada jenis ini dipilih adalah kerana kos yang murah, mudah didapati dalam banyak bentuk dan saiz, dan senang dicas semula tanpa risiko terbakar atau letupan yang besar.

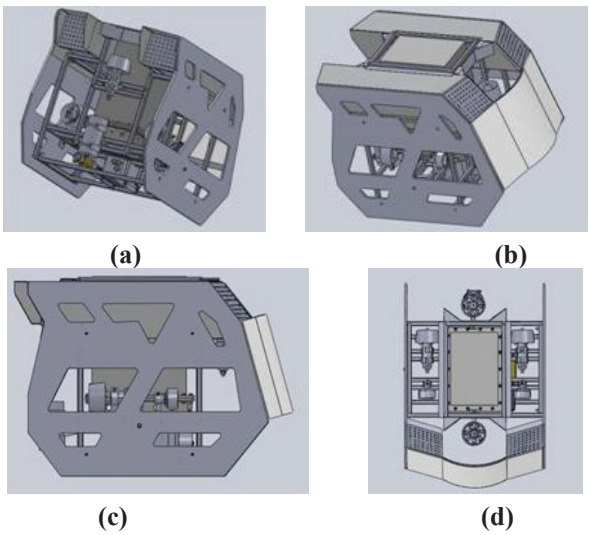

Rajah 5: Rekabentuk lengkap ROV: (a) Pandangan hadapan; (b) Pandangan belakang (c) Pandangan atas; dan (d) Pandangan sisi.

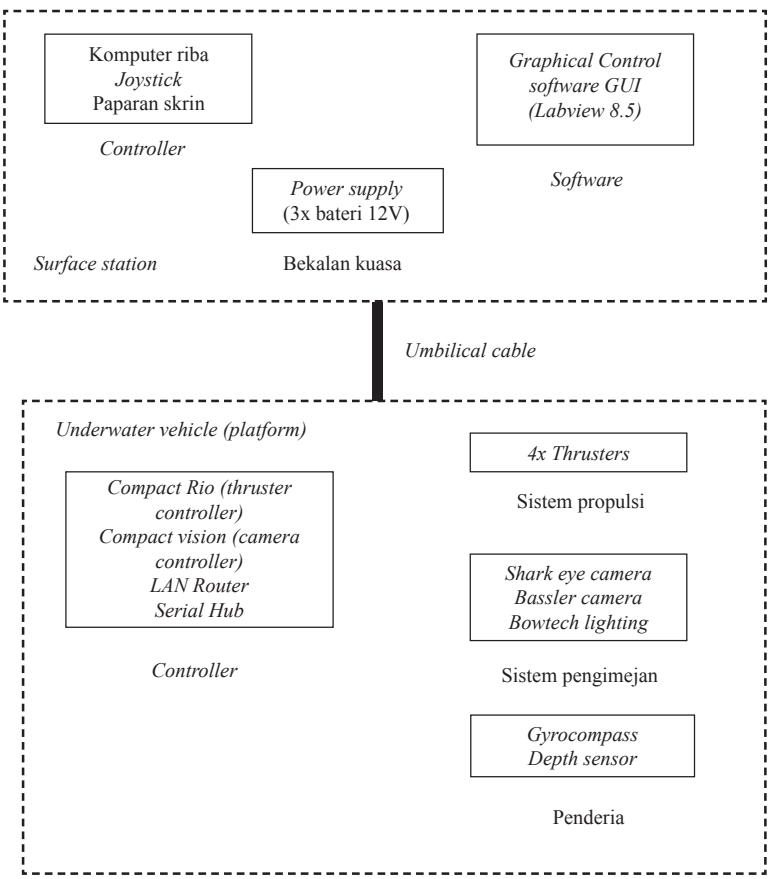

Rajah 6: Sistem kawalan navigasi dan integrasi peralatan.

Secara keseluruhannya, kesemua perkakasan elektronik serta penderia menerima bekalan kuasa daripada 2 unit bateri *lead acid.* Setiap unit bateri mempunyai bekalan 12V dan arus terus 24 AH secara siri dan selari bagi memenuhi permintaan bekalan sebanyak 12 V dan 24 V. Bagi sistem pendorong, lampu, *CompactRio* dan *Compact Vision*, bekalan sebanyak 24 V diperlukan, maka terminal keluaran sambungan secara siri digunakan, manakala sistem penderia kedalaman, *gyrocompass*, kamera dan *router* disambungkan pada terminal keluaran 12 V. Litar skematik pengagihan kuasa elektrik bagi keseluruhan sistem ROV adalah seperti di dalam Rajah 7.

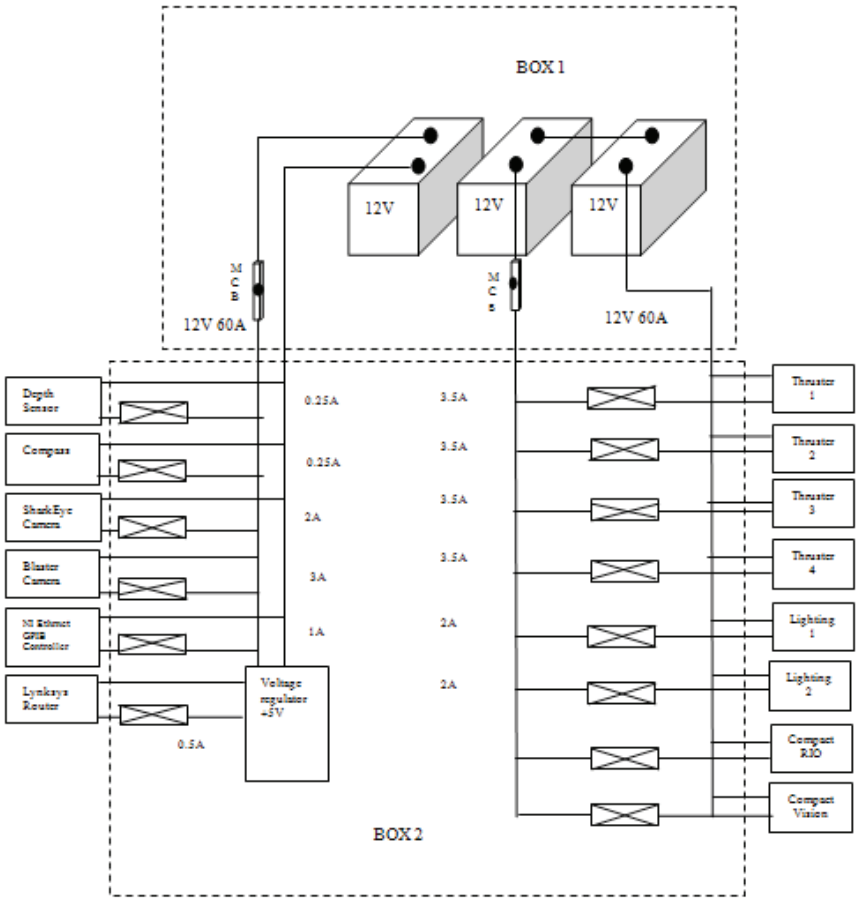

Rajah 7: Litar skematik pengagihan kuasa elektrik keseluruhan sistem.

Sistem kawalan navigasi ROV yang dibangunkan terdiri daripada dua bahagian utama iaitu sistem kawalan jauh dan sistem kawalan navigasi. Sistem kawalan jauh terdiri daripada sebuah komputer riba dan *joystick*, manakala sistem kawalan navigasi di dalam ROV pula terdiri daripada sebuah *microcontroller*, sebuah *depth sensor*, sebuah *magnetic compass,* 4 buah *thruster* dan 2 buah kamera bawah air. Keseluruhan sistem tersebut diintegrasikan dengan menggunakan perisian *LabView 8.5*. Perisian ini adalah mudah untuk difahami dan digunakan bagi integrasi dengan penderia-penderia yang akan digunakan.

Microcontroller yang digunakan adalah *CompactRio* dengan teknologi *field programmable gate array* (FPGA). Ia dipilih berdasarkan faktor mudah untuk diprogram dan diintegrasi, ringan, tahan lasak, sangat sesuai digunakan dalam aplikasi-aplikasi berkaitan robotik, dan menggunakan teknologi yang sesuai (Xunzhang *et al*., 2000). Teknologi FPGA yang diaplikasi di dalam *CompactRio* juga adalah antara teknologi terkini dalam pembinaan *microcontroller*. Ia mampu menyimpan memori yang besar dan kadar pemprosesan yang sangat pantas.

Pergerakan ROV ini boleh dikawal sepenuhnya oleh *thruster*. Dengan menggunakan lebih daripada sebuah *thruster*, pergerakan pada semua arah boleh dilakukan. Perkara yang perlu dilakukan ialah menyusun *thruster* ini mengikut arah pergerakan yang dikehendaki. Susunan *thruster* yang mudahalih memberikan kelebihan apabila sistem dorongan kenderaan hendak diubahsuai (Bai & Bai, 2010)

Sistem dorongan ROV ini terdiri daripada 4 buah *thrusters*, di mana 2 diletakkan di posisi mendatar (untuk pergerakan kiri dan kanan), manakala dua yang selebihnya di posisi menegak (untuk pergerakan atas dan bawah). *Thruster* yang digunakan adalah jenis *DC brushless motor* yang dihasilkan oleh *Technadyne*. Platform ini menggunakan bekalan kuasa 24 V untuk membekalkan kuasa kepada sistem pendorong. Untuk mengawal kelajuan dan arah pusingan thruster, voltan +/-5 V diberikan pada kabel isyarat sistem pendorong.

Apabila bergerak dalam keadaan halaju malar, daya tujah yang dihasilkan adalah bersamaan dengan daya geseran atau daya seret kenderaan tersebut iaitu:

$$daya\ \ tujah\ -\ \ daya\ \ seret = \frac{1}{2}\pi\rho s^2 Ac_D \qquad (1)$$

di mana ρ adalah ketumpatan air, s adalah halaju, A adalah luas permukaan dan c_D adalah pekali daya seret (*drag coefficient*).

Apabila halaju kenderaan meningkat, penggunaan kuasa oleh sistem dorongan juga akan meningkat kerana kuasa tujahan yang terhasil adalah bersamaan dengan gabungan daya tujah dan halaju kenderaan tersebut, sebagaimana berikut:

$$kuasa\ \ tujahan\ -\ \ daya\ \ tujah * s = \frac{1}{2}\pi\rho s^3 Ac_D \qquad (2)$$

2.3 Sistem Kawalan dan Komunikasi

Pembangunan sistem dimulakan dengan memuat-turun perisian *Labview* ke *CompactRIO* dengan perantara komputer riba jenis *Panasonic Toughbook*. Pembangunan perisian kawalan ROV dilakukan di atas PC ini dan kod FPGA dimuat-turun ke dalam sistem *CompactRIO* menggunakan kabel rangkaian RJ45. Aplikasi kawalan yang dibangunkan ini memberikan maklumat kawalan kepada sistem *CompactRIO*, yang seterusnya memberikan maklumat kawalan elektrikal kepada perkakasan yang terlibat di dalam ROV. Perkakasan yang terlibat dalam pembangunan sistem kawalan pergerakan *thruster* ini dihubungkan melalui *wiring diagram* (Rajah 8).

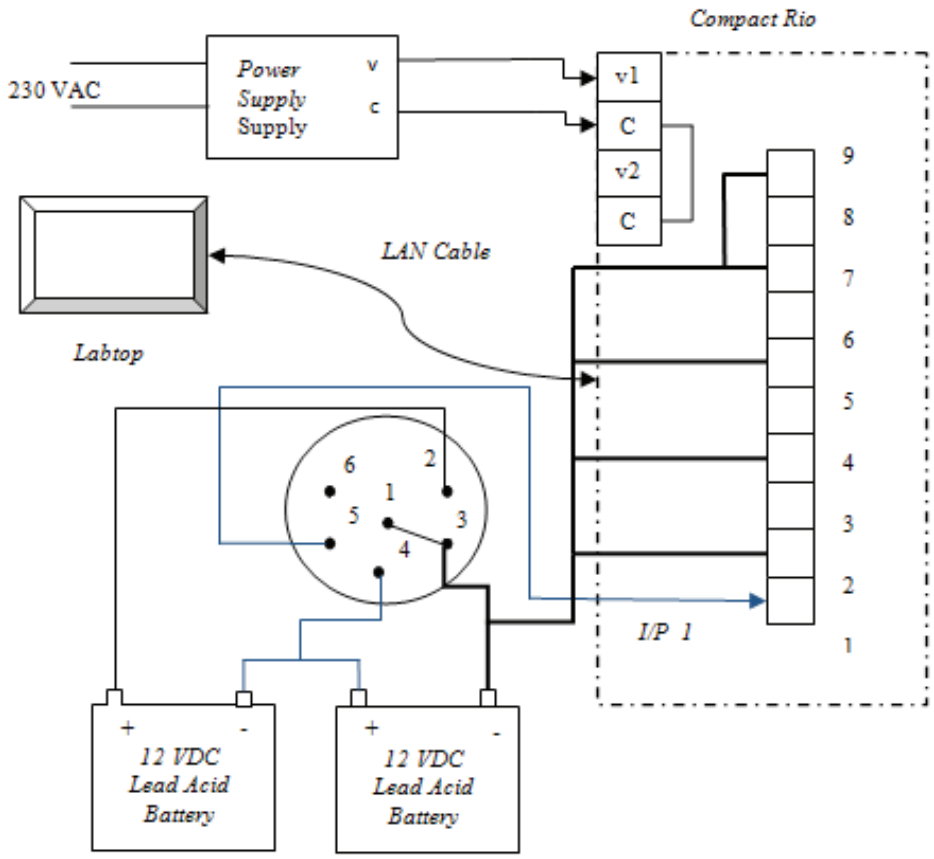

Rajah 8: *Wiring diagram* untuk sistem kawalan *thruster*.

Dua fail utama yang terlibat dalam pembangunan sistem ini dinamakan dengan akhiran _FPGA.vi dan _HOST.vi. Fail FPGA adalah fail yang dimuat-turun ke dalam sistem *CompactRIO* manakala fail HOST pula adalah fail kawalan yang diletakkan di dalam komputer riba dan berkomunikasi dengan fail FPGA di dalam *CompactRIO* (Jingjuan & Rong, 2009; Tian-Ling & En, 2010).

Antaramuka yang telah dibangunkan adalah untuk mengawal keempat-empat *thrusters* bagi menggerakkan ROV ini (Rajah 9). *Thrusters* 1 dan 3 digunakan untuk kawalan lateral (kiri – kanan – depan – belakang) manakala *thrusters* 2 dan 4 digunakan untuk mengawal pergerakan menegak (naik dan turun).

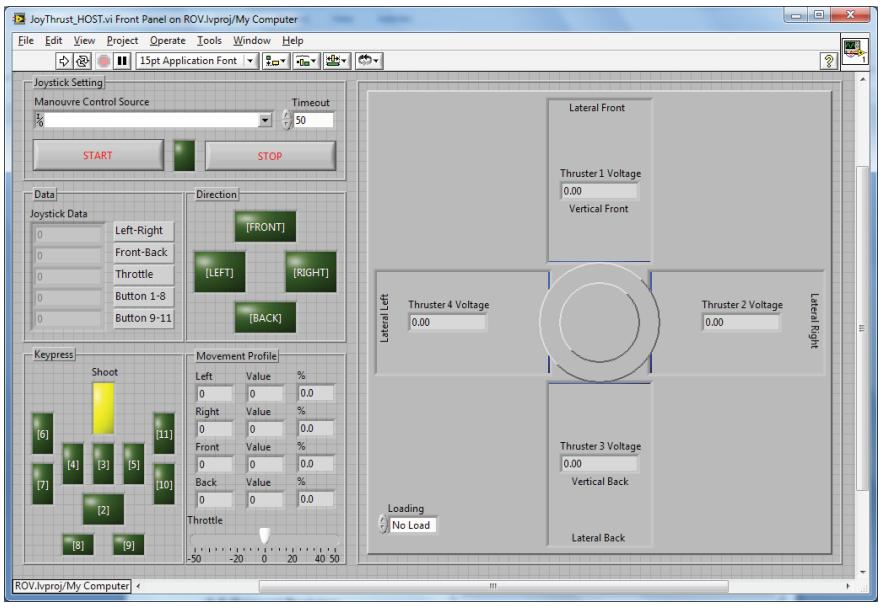

(a)

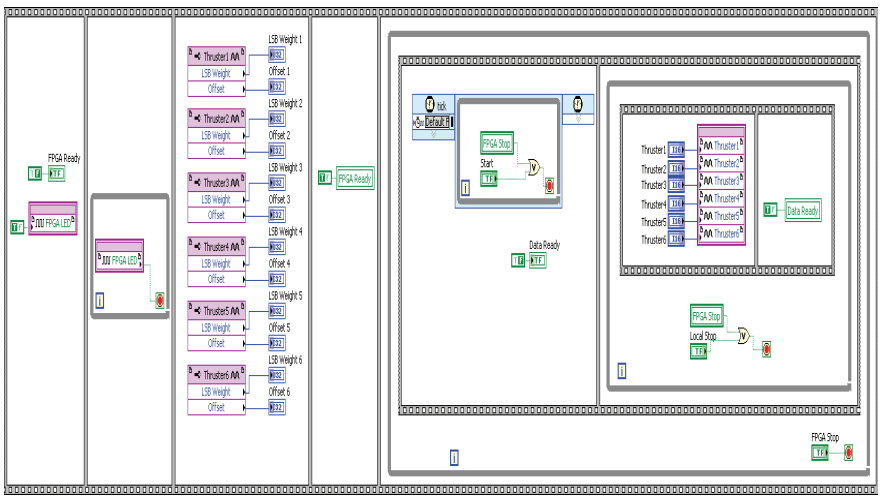

(b)

Rajah 9: Antaramuka bagi fail (a) JoyThrust_HOST.vi (*front panel*); dan (b) fail FPGA (*block digram*).

Setiap kali terdapat gerakan pada *joystick,* terdapat nilai pada bahagian *Joystick Data* dan LED segiempat yang berkaitan akan bernyala. Sekiranya butang pada *joystick* ditekan, ia dapat dikesan dengan melihat bahagian *Keypress.*

3. KEPUTUSAN DAN PERBINCANGAN

Berdasarkan kepada rekabentuk konsep yang telah dicadangkan, satu prototaip ROV telah berjaya dibangunkan (Rajah 10) dan diuji. Pengujian peringkat awal melibatkan tahap integrasi keseluruhan sistem kawalan dengan kerangka utama telah berjaya dilakukan di makmal.

Rajah 10: Prototaip ROV yang telah dibangunkan.

Antara maklumat yang paling penting adalah profil pergerakan bagi ROV tersebut. Maklumat tersebut telah berjaya ditunjukkan di bahagian kanan paparan antara muka yang telah dibina. Voltan *thruster* juga ditunjukkan mengikut setiap pergerakan yang berbeza (Rajah 11). Sekiranya *No Load* dipilih, voltan keluaran sebenar mempunyai maksimum 2.5 V sahaja, berbanding paparan 5.0 V. Ini adalah salah satu langkah keselamatan bagi mengelakkan kerosakan pada *thruster*.

Pengujian peringkat kedua pula melibatkan ujian prototaip di lapangan juga telah berjaya dilaksanakan. Prototaip ROV telah diuji di dalam tangki air buatan sedalam 1.5 m bagi memastikan tahap kefungsian setiap sistem berada di tahap yang optimum. Hasil ujian menunjukkan sistem propulsi kenderaan, sistem pengimejan dan juga sistem penderia berfungsi dengan baik, sekali gus membuktikan bekalan kuasa dan sistem kawalan kenderaan berada dalam keadaan yang optimum. ROV juga didapati berjaya berada di dalam keadaan keapungan positif (*positive buoyancy*), di mana kenderaan akan terapung ketika tidak beroperasi atau dalam keadaan melahu (*idle*) bagi memudahkan proses penyediaan dilakukan apabila sesuatu misi ingin dilaksanakan.

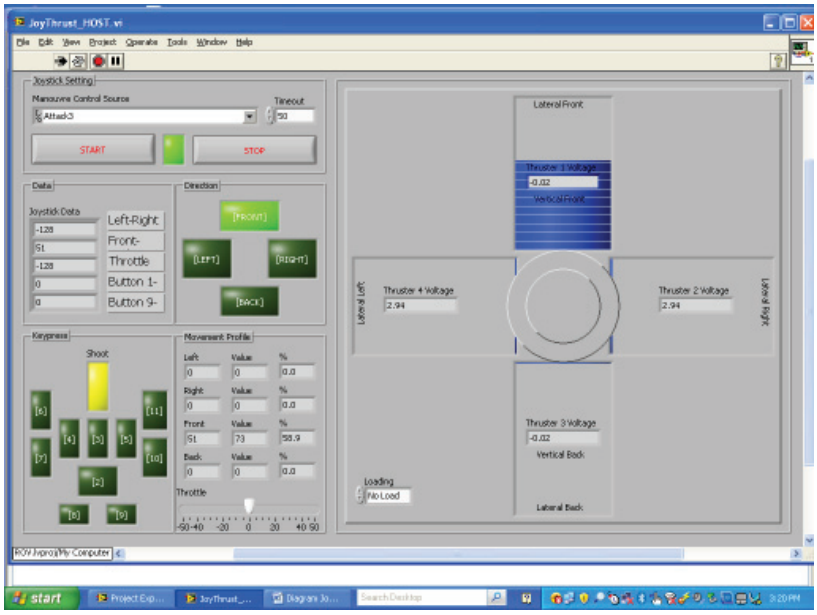

(a)

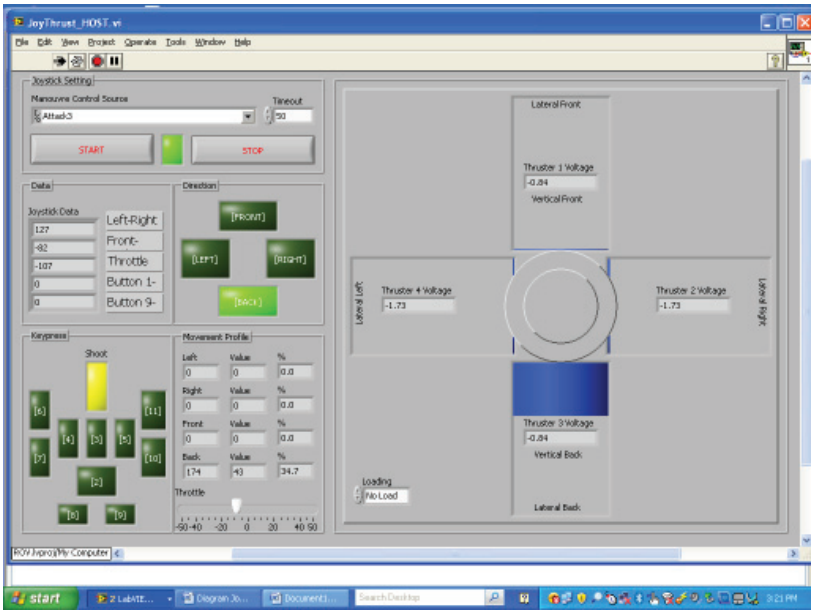

(b)

Rajah 11: Contoh antaramuka untuk profil pergerakan bagi (a) *forward*; dan (b) *backwards*.

4. KESIMPULAN DAN CADANGAN

Secara umumnya, ROV yang dibangunkan sememangnya sesuai bukan hanya untuk aplikasi komersial dan industri, malah juga untuk operasi ketenteraan. Walaubagaimanapun, projek ini perlu diteruskan lagi ke arah fasa yang seterusnya iaitu dengan penambahan pelbagai ciri sokongan lain bagi meningkatkan tahap pengoperasian platform tersebut. Perkara ini dapat dilaksanakan melalui pemadanan beberapa aksesori tambahan seperti lengan robot (*manipulator arm*) bagi tujuan mengambil atau memegang sebarang objek di bawah permukaan air dan juga penambahan lengan pemotong bagi kerja-kerja pemotongan di bawah permukaan air.

Pada masa akan datang, projek ini juga dicadangkan agar memasuki fasa pembangunan ROV yang lebih sofistikated iaitu dengan membangunkan sebuah AUV dan juga platform di permukaan air bagi mengintegrasi sistem perhubungan bawah permukaan dan permukaan air. Platform di permukaan air akan dilengkapi dengan perhubungan radio jarak jauh bagi penghantaran data-data penderia dan video. Platform ini akan dikawal dengan menggunakan sistem *Radio Frequency* dari stesen kawalan di pantai. Ia akan dilengkapi oleh sistem *Global Positioning System* (GPS), penderia akustik, dan penderia saintifik seperti suhu dan kemasinan laut.

RUJUKAN

Alvarez, A., Bertram, V. & Gualdesi, L. (2009). Hull hydrodynamic optimization of autonomous underwater vehicles operating at snorkeling depth. *Ocean Eng.,* **36**: 105-112.

Molland, A.F. (2008). *The Maritime Engineering Reference Book: A Guide to Ship Design, Construction and Operation.* Butterworth-Heinemann, Oxford.

Bai, Y. & Bai, Q. (2010). *Subsea Structural Engineering Handbook*. Gulf Professional Publishing, Boston.

Frost, A. R., McMaster, A. P., Saunders, K. G. & Lee, S. R. (1996). The development of a remotely operated vehicle (ROV) for aquaculture. *Aquacult. Eng.,* **15**: 461-483.

Howse, J. (2009). The ROV Pontus: A winning design in Electrical and Computer Engineering. *22nd Canadian Conference on Electrical and Computer Engineering (CCECE 2009),* 3-6 Mei 2009, Newfoundland, Canada.

Jamian, M.Z. (2009). *Underwater technologies for military applications – securing its future*. Underwater technologies for military applications: Securing its future. *3rd Technical Seminar on Underwater System Technology,* Universiti Putra Malaysia, Serdang, Selangor.

Jingjuan, Z. & Rong, Z. (2009). A better engineering method for measuring gyro drift of INS based on LabVIEW platform. *9th International Conference on Electronic Measurement & Instruments (ICEMI '09)*, 16-19 Ogos 2009, Beijing.

Lygouras, J.N., Lalakos, K.A. & Tsalides, T.G. (1998). THETIS: An underwater remotely operated vehicle for water pollution measurements. *Microprocess Microsy,*. **22**: 227-237.

Muljowidodo, K., Sapto, A. N. & Nico, P. (2010). Design and analysis of "PARI" air deployment AUV. *3rd International Conference on Underwater System Technology: Theory and Application (USYS'10)*, 1-2 November 2010, Cyberjaya, Malaysia.

Mahoney, K. L., Grembowicz, K., Bricker, B., Crossland, S., Bryant, D., Torres, M. & Giddings, T. (2009). RIMPAC 08: Naval oceanographic office glider operations. *Proc. SPIE 7317 (Ocean Sensing and Monitoring),* 731706.

Presto, T., (2001). *Verification of a Six-Degree of Freedom Simulation Model for the REMUS Autonomous Underwater Vehicle*. Tesis M.Sc., Massachusetts Institute of Technology (MIT) dan Woods Hole Oceanographic Institution (WHOI) , Massachusetts.

Rahim, K.I.A., Othman, A.R. & Arshad, M.R. (2010). Pressure hull development using hybrid composite with metal liner concept, *3rd International Conference on Underwater System Technology: Theory and Application 2010 (USYS'10)*, 1-2 November 2010, Cyberjaya, Malaysia.

Ross, C.T.F. (2006). A conceptual design of an underwater vehicle. *Ocean Eng*., **33**: 2087-2104.

Tian-Ling, H. & En, C. (2010). Simulation and analysis of underwater acoustic spread spectrum system based on LabView. *2010 International Conference on Computer Application and System Modeling (ICCASM)*, 22-24 Oktober 2010, Taiyuan, Shanxi.

Xunzhang, W., Seet, G.G.L., Lau, M.W.S., Low, E. & Tan, K.C. (2000). Exploiting force feedback in pilot training and control of an underwater robotics vehicle: an implementation in LabVIEW. *OCEANS 2000 MTS/IEEE Conference and Exhibition*, 11-14 September 2000, Providence, Rhode Island.

Yuh, J. (2000). Design and control of autonomous underwater robots: A survey. *Auton. Robots*, **8**: 7-24.

KAJIAN KEBERKESANAN SOLARGIZER DALAM MENINGKATKAN KEUPAYAAN KAPASITI PENYIMPANAN CAS BATERI KENDERAAN

Nor Hafizah Mohamed*, Zariyah Ariffin & Mohd Hadi Salihin Mohd Supian

Cawangan Penyelidikan Operasi, Bahagian Pengurusan Sumber Manusia & Khidmat Sokongan (BPSM&KS), Institut Penyelidikan Sains & Teknologi Pertahanan (STRIDE), Kementerian Pertahanan, Malaysia

*Email: norhafizah.mohamed@stride.gov.my

ABSTRAK

Kajian ini dilaksanakan ini mengenalpasti sama ada Solargizer dapat memberi impak yang signifikan dalam meningkatkan jangka hayat bateri kenderaan melalui perbandingan bateri dengan dan tanpa penggunaan Solargizer. Tempoh masa menyahcas bateri telah diuji bagi populasi 40 kali kitaran, iaitu 20 ujian bateri menggunakan Solargizer dan 20 ujian bateri tidak dipasang alat tersebut. Kaedah Rekabentuk Ujikaji / Design of Experiments (DOE) telah digunakan untuk menguji keberkesanan Solargizer terhadap jangka hayat bateri . Data yang diperolehi daripada ujikaji / ekperimen yang dijalankan di makmal telah dianalisis berdasarkan teknik Rekabentuk Penuh Rawak / Complete Randomized Design (CRD) dan ujian Analisis Varians / Analysis of Variance (ANOVA) untuk menguji hipotesis kajian. Hasil kajian menunjukkan yang penggunaan Solargizer tidak memberi kesan yang signifikan ke atas peningkatan keupayaan jangka hayat bateri. Penemuan ini adalah tidak konsisten dengan anggapan asal terhadap Solargizer, serta kajian lepas yang dijalankan. Ini adalah mungkin kerana terdapat ralat pada data yang diambil semasa ekperimen yang dijalankan. Selain itu juga, kajian ini hanya tertumpu kepada satu jenis Solargizer sahaja.

Kata Kunci: *Solargizer; Rekabentuk Ujikaji / Design of Experiments (DOE); Rekabentuk Penuh Rawak / Complete Randomized Design (CRD); Analisis Varians / Analysis of Variance (ANOVA); Ujian Hipotesis.*

1. PENGENALAN

Bateri merupakan nadi kepada kebanyakan peralatan dan perkakasan yang digunakan oleh manusia. Ia berfungsi sebagai sumber tenaga dan kuasa bagi menjana dan menggerakkan peralatan yang umumnya beroperasi melalui orientasi elektrik dan elektronik. Bateri terdiri daripada beberapa kombinasi sel yang bertindak sebagai pencetus kepada penjanaan kuasa elektrik apabila dikenakan cas-cas tertentu. Dalam pelbagai peralatan yang dicipta oleh manusia, bateri menjadi keperluan dan sangat berguna bagi melakukan aktiviti seharian.

Secara umumnya, bateri terbahagi kepada dua kategori yang dikelaskan mengikut ciri-ciri yang tertentu; bateri bersel basah dan bateri bersel kering. Bateri bersel kering kebanyakannya terdiri daripada bateri-bateri daripada jenis Nikel, Kadmium, Merkuri, Lithium dan Alkaline. Bateri-bateri ini kebanyakanya digunakan dalam perkakasan dan peralatan konvensional seperti jam, lampu suluh, radio, telefon bimbit dan sebagainya. Setiap sel daripada bateri bersel kering ini dapat menjanakan kuasa elektrik sebanyak 1.5 V dan sesetengahnya boleh dicas (Crompton, 2000; Linden & Reddy, 2001; Buchmann, 2011).

Untuk bateri bersel basah, sel-selnya adalah berbentuk plat-plat logam yang direndam ke dalam sejenis cecair yang dikenali sebagai elektrolit. Elektrolit mengandungi komposisi 62 % asid sulfurik dan 38 % air suling. Bateri bersel basah selalunya digunakan dalam perusahaan berat seperti automobil. Kebanyakan kenderaan darat khususnya, menggunakan bateri ini kerana ia berkuasa tinggi dan mampu dicas semula dalam tempoh yang singkat. Namun begitu, terdapat masalah yang wujud di mana, dalam jangka waktu yang tertentu, plat-plat logam tersebut mengalami kesukaran menerima cas-cas tenaga yang akan menjana kuasa elektrik. Keadaan ini biasanya terjadi kerana tindak balas yang berlaku di dalam elektrolit menyebabkan proses pensulfatan berlaku (Crompton, 2000; Linden & Reddy, 2001; Buchmann, 2011).

Sejak kebelakangan ini, pihak Angkatan Tentera Malaysia (ATM) sering mengalami masalah kehilangan kuasa bateri kenderaan yang digunakan sebelum jangka hayat bateri tersebut tamat. Kebanyakan bateri yang berada di pasaran dan yang digunakan oleh ATM adalah bateri yang menggunakan teknologi *Lead Acid Battery.* Kebanyakan bateri dikatogerikan sebagai mati (*dead battery*) kerana tiada lagi keupayaan untuk menyimpan dan menerima cas pada plat. Hal ini menimbulkan kesulitan kepada pihak ATM di dalam menjalankan tugas mereka. Setelah terjadi berulang-kali, pihak ATM mendapati masalah yang timbul adalah disebabkan oleh pensulfatan (*sulfation*) yang berlebihan pada bateri. Pensulfatan akan terbina pada plat bateri semasa pengecasan dan juga nyahcas bateri tersebut. Pensulfatan ini terbentuk daripada *lead sulfates*.

Di dalam proses ini, sebahagian daripada sulfat akan bertambah dan seterusnya melekat pada plat tersebut, dan akan menyebabkan plat tidak dapat menerima cas lagi. Dengan pertambahan penggunaan dan masa, sulfat ini akan bertambah pada plat bateri mengakibatkan keupayaan bateri berkurangan dan seterusnya menyebabkan bateri itu mati. Menurut kajian yang dibuat oleh kilang pengeluar Solargizer, 80% daripada punca kegagalan bateri adalah disebabkan oleh faktor ini (Industrial Solargizer, 2007).

Apabila bateri dinyahcas atau kekal tidak aktif, unsur-unsur sulfat yang sememangnya wujud dalam elektrolit akan terbentuk pada plat-plat atau sel-sel bateri. Dalam jangka waktu yang singkat, sulfat ini akan bergabung secara beransur-ansur dan seterusnya membentuk mendapan berhablur. Ini menyebabkan plat-plat bateri tersalut lalu mengakibatkan plat-plat tidak dapat menerima atau memindahkan cas-cas secara efektif. Proses ini dikenali sebagai pensulfatan yang berlaku ke atas semua asid utama bateri dalam pelbagai aplikasi seperti pengendalian bahan mentah, janakuasa bantuan, pelombongan, automotif dan marin. Malah, ia adalah menjadi punca utama kepada kerosakan bateri. Apabila proses pensulfatan ini berlaku, plat-plat logam yang terhalang daripada menerima cas akan gagal berfungsi dan lama-kelamaan ia akan melemahkan kapasiti penyimpanan bateri.

Alternatif yang muncul bagi menangani permasalahan ini adalah dengan menggunakan peralatan yang dipatenkan dengan teknologi denyutan (*pulse technology*) supaya dapat menghalang proses pensulfatan berlaku di dalam bateri yang sedia ada mahupun yang baru (Industrial Solargizer, 2007). Dengan mengalirkan denyutan arus terus (*direct current*) ke dalam bateri, ia akan menjana semula tenaga sulfat yang terhablur dan mengembalikannya semula ke dalam asid bateri dalam bentuk molekul-molekul sulfur yang aktif. Dengan plat-plat bateri yang sentiasa bersih, ia akan memberikan lebih kuasa, tempoh mengecas yang pantas, suhu mengecas yang lebih sejuk dan jangka hayat bateri yang lebih lama. Menggunakan alternatif tersebut, banyak syarikat daripada industri pembuatan telah mengambil inisiatif dalam merangka projek-projek penyelidikan untuk mencipta alat yang khusus untuk mengurangkan proses pensulfatan daripada terus berlaku.

Solargizer telah dicipta dan digunapakai oleh kebanyakan kenderaan yang menggunakan kuasa bateri di seluruh dunia supaya dapat mempertingkat dan mengoptimum penggunaan bateri terutamanya kepada kenderaan-kenderaan darat seperti trak, lori, jentera dan kereta (Global Merchants, 2000). Ia juga menjadi satu pelaburan yang penting dalam jentera-jentera pertahanan di kebanyakan negara maju. Pihak Tentera Amerika Syarikat juga telah menggunakan Solargizer bagi membantu memanjangkan hayat bateri daripada cepat rosak sejak tahun 1995 (PulseTech Products Corporation, 2001). Justeru, penggunaannya yang meluas telah menarik minat Malaysia terutama di Kementerian Pertahanan, untuk digunakan dengan jentera-jentera pertahanan bagi mengurangkan keperluan dan kos pembelian bateri yang baru.

Objektif kajian ini adalah untuk mengkaji keberkesanan penggunaan Solargizer di dalam meningkatkan keupayaan jangka hayat bateri kenderaan, dan membandingkan penggunaan Solargizer pada bateri kenderaan dengan bateri tanpa Solargizer.

2. UJIAN STATISTIK

Ujian statistik yang digunakan dalam kajian ini adalah *Design of Experiments* **(**DOE) melalui teknik Rekabentuk Penuh Rawak / *Complete Randomized Design* (CRD). Data kajian ini dianalisis secara statistik oleh kumpulan teknik yang dirujukkan sebagai ujian Analisis Varians / *Analysis of Variance* (ANOVA) dan mempunyai perkaitan langsung dengan ujian hipotesis bagi mendapatkan keputusan kajian.

2.1 Rekabentuk Ujikaji / *Design of Experiments* (DOE)

DOE ialah rancangan dan struktur untuk menguji hipotesis dimana penyelidik sama ada boleh mengawal atau memanipulasi satu atau lebih angkubah (Hazura *et al*, 2009). Selain itu, DOE juga boleh didefinasikan sebagai suatu kerangka kajian atau penyelidikan saintifik yang relevan dengan masalah yang dihadapi (Hinkelmann & Kempthorne, 2008). Ia mengandungi angkubah sandar dan angkubah bebas. Di dalam rekabentuk ujikaji, angkubah bebas mungkin sama ada angkubah rawatan dan angkubah kelasifikasi. Angkubah rawatan (Solargizer) ialah satu ujikaji kawalan atau ujikaji yang telah diubahsuai. Angkubah kelasifikasi ialah beberapa ciri-ciri bagi subjek ujikaji yang telah ditetapkan terdahulu dan ia bukanlah hasil manipulasi ujikaji atau kawalan. Angkubah bebas kadangkala dirujukkan sebagai faktor (bateri).

Satu lagi jenis angkubah di dalam DOE ialah angkubah sandar (tempoh masa tamat menyahcas). Angkubah sandar ialah tindakbalas terhadap perbezaan paras di dalam angkubah bebas. Ia adalah ukuran yang diambil dibawah keadaan rekabentuk ujikaji yang menggambarkan kesan angkubah bebas. Terdapat berbagai-bagai teknik yang boleh digunakan dalam kaedah ini seperti CRD, *Complete Randomised Block Design* (CRBD), *Latin Square Design* (LSD), *Graeco-Latin Square Design* (GLSD), dan 2^k *Factor Factorial Design*. Walaubagaimanapun, pengaplikasian teknik-teknik tersebut adalah tertakluk kepada kondisi masalah dan jenis data yang terlibat.

2.2 Teknik Rekabentuk Penuh Rawak / *Complete Randomized Design* (CRD)

Pengkaji telah menetapkan ujian statistik yang akan digunakan adalah teknik CRD kerana unit dalam eksperimen ini adalah homogen. CRD adalah subjek diletakkan secara rawak kepada rawatan. Rekabentuk penuh rawak hanya mengandungi satu angkubah bebas, dengan dua atau lebih paras rawatan (tahap rawatan), atau kelasifikasi. Bagi kajian ini terdapat hanya dua paras rawatan (Rajah 1), atau kelasifikasi angkubah bebas. Rekabentuk ini adalah sama dengan apa yang digunakan untuk menguji perbezaan min dua populasi bebas dengan menggunakan ujian t untuk menganalisis data. Ujian ANOVA digunakan untuk menganalisis data yang dihasilkan dari rawatan.

2.3 Ujian ANOVA

Ujian ANOVA adalah ujian yang paling banyak digunakan dalam kajian sains dan tingkah laku (Howell, 1999). Ujian ANOVA ini sesuai digunakan untuk menguji sama ada terdapat perbezaan yang signifikan antara dua atau lebih daripada dua set data yang dipungut daripada subjek yang sama pada masa yang berlainan sepanjang rawatan (Chua, 2006). Oleh yang demikian, pengkaji telah menetapkan untuk menggunakan Ujian ANOVA sebagai satu prosedur untuk menguji sama ada terdapat perbezaan di antara dua atau lebih min populasi bagi sesuatu data selanjar (*interval data*) (Rasimah, 2005). Seterusnya, ia membantu mendapatkan inferens dan interpretasi secara analitikal terhadap populasi kajian.

Secara amnya, Rekabentuk Penuh Rawak dianalisis menggunakan ANOVA satu hala. Terdapat beberapa elemen atau aspek penting bagi kajian ini yang berkaitan dengan ujian ANOVA. Elemen-elemen tersebut ialah Rawatan (*Treatment*), Ralat (*Error*) dan Jumlah (*Total*). Kesemua elemen ini akan dihitung menggunakan formula-formula tertentu bagi mendapatkan Jadual ANOVA. Prosedur seterusnya adalah menjalankan Ujian Hipotesis ke atas data-data atau rekod-rekod kajian yang diperolehi. Manakala, jadual bagi nilai genting diperolehi daripada jadual taburan kebarangkalian *F* (*F Distribution*) dalam menentukan sama ada menolak atau tidak menolak hipotesis nul.

3. METODOLOGI KAJIAN

3.1 Pengumpulan dan Penyusunan Data

Di dalam eksperimen asal yang dijalankan di makmal Bahagian Teknologi Instrumentasi & Elektronik (BTIE), STRIDE, terdapat empat jenis ujian berbeza yang dilakukan bagi menguji keupayaan Solargizer bagi kegunaan ATM (STRIDE, 2002). Ujian-ujian tersebut ialah *Recovery Dead Battery, Charge Maintenance Test, Pulsation Effect on Stored Battery* dan *Loss Charge Capacity*. Kesemua empat jenis ujian tersebut telah diuji menggunakan Solargizer.

Data daripada ujian *Loss Charge Capacity* digunapakai dalam penyelidikan ini kerana ia mempunyai rekod yang lengkap dan relevan terhadap penyelidikan. Kajian yang dilaksanakan dan data yang diperoleh ini adalah berdasarkan tempoh masa yang dicatatkan apabila *voltmeter* yang dipasang dalam litar bersiri menunjukkan bacaan 10.50 V, iaitu menunjukkan keupayaan mengecas bateri telah habis. Catatan masa yang lebih lama menunjukkan tempoh pengecasan yang lebih efektif.

Di dalam kajian ini, rekod ujikaji adalah berupa catatan data atau nilai bacaan yang diambil daripada ujian *Loss Charge Capacity* untuk dianalisis. Ia bertujuan untuk mengenalpasti keupayaan dan keberkesanan Solargizer yang dipasang, terhadap kapasiti penyimpanan cas bateri kenderaan. Penilaian terhadap eksperimen ini lebih cenderung untuk mengenalpasti kadar pengurangan cas terhadap kapasiti bateri. Lazimnya, kadar kehilangan cas pada bateri yang lebih lama adalah lebih baik, kerana kapasiti penyimpanannya dapat bertahan lama. Justeru, eksperimen ini antara lain bertindak sebagai tanda aras bagi menentukan tahap keberkesanan Solargizer.

Pada peringkat awal kajian, data mentah daripada lembaran data akan diekstrak untuk membentuk jadual yang mewakili data bagi keempat-empat buah bateri. Data untuk dua buah bateri yang dipasang Solargizer dan dua buah bateri yang tidak dipasang akan diasingkan untuk membentuk dua kumpulan iaitu kumpulan bateri yang dipasang dan tidak dipasang dengan Solargizer. Setiap satu kumpulan ini mengandungi bacaan bagi bateri yang ditandakan sebagai Bateri 1 dan Bateri 2 yang menjadi bahan eksperimen. Di dalam ujian menentukan tempoh masa menyahcas bateri dengan atau tanpa menggunakan Solargizer, purata masa bagi setiap dua buah bateri yang dipasang atau tidak dipasang alat tersebut akan dihitung. Ini bermakna, purata masa bagi Bateri 1 dan Bateri 2 yang dipasang Solargizer akan diperolehi, dan begitu juga dengan purata masa bagi Bateri 1 dan Bateri 2 yang tidak dipasang Solargizer. Ini adalah bagi mendapatkan suatu bacaan yang boleh mewakili kedua-dua sampel yang diambil.

Nilai purata yang telah dihitung disusun di dalam jadual lain bagi mendapatkan perkaitan di antara kedua-dua kumpulan eksperimen, seterusnya memudahkan pengiraan menggunakan Kaedah Rekabentuk Ujikaji / *Design of Experimental* (DOE). Data bagi setiap bateri adalah dicatat di dalam unit minit dengan mengabaikan kiraan saatnya. Purata masa diambil kerana keempat-empat bateri tersebut adalah sama dari segi jenis dan kapasiti asalnya. Catatan masa telah ditukar kepada unit minit bagi memudahkan pengiraan.

3.2 Persampelan

Persampelan berstrata dilakukan dalam kajian ini kerana jumlah populasi kajian telah diketahui melalui unit eksperimen yang terlibat. Dalam melaksanakan pensampelan ini, data akan diasing mengikut kumpulan yang terdiri daripada unit-unit yang homogen. Bagi mendapatkan sampel yang dapat mewakili keseluruhan populasi kajian dalam ujikaji bateri tersebut, sampel diambil dalam kuantiti yang banyak bagi mendapatkan data yang tepat. Seterusnya, pemilihan sampel dilaksanakan menggunakan Jadual Nombor Rawak (*Table of Random Numbers*). Penggunaan jadual ini bertujuan mendapatkan kebarangkalian yang sama bagi setiap sampel yang akan dipilih bagi mengelakkan *bias*. Kaedah pensampelan ini juga digunakan supaya sampel yang akan dipilih diwakili secukupnya oleh sesebuah golongan spesifik atau golongan minoriti yang dikehendaki.

3.3 Analisis Data Kajian

Teknik CRD hanya boleh digunakan apabila unit dalam ekperimen (data) adalah homogen. Dalam kajian ini, data yang diperolehi adalah daripada sumber yang sama, iaitu bateri yang sama jenis dan kapasiti asalnya dengan tempoh masa yang dicatat dalam unit minit. Data eksperimen ini dianalisis untuk membandingkan sama ada keupayaan bateri yang dipasang Solargizer memberi kesan ke atas kitaran, di mana tempoh masa bagi populasi 40 kali kitaran yang telah diuji iaitu sebanyak 20 ujian bateri menggunakan Solargizer dan 20 ujian bateri tidak dipasang alat tersebut.

Perbezaan CRD dengan teknik-teknik yang lain adalah kerana kajian yang dilakukan menggunakan satu faktor sahaja. Dalam kajian ini, faktor atau pembolehubah tidak bersandar yang terkawal adalah kondisi bateri dengan atau tanpa Solargizer. Pembolehubah ini mempengaruhi pembolehubah bersandar iaitu tempoh masa tamat menyahcas (apabila bacaan *voltmeter* menunjukkan 10.50 V). Ini bermakna, kedua-dua pembolehubah ini mempunyai perkaitan langsung kerana kajian bertujuan mengenalpasti wujudnya kesan yang signifikan terhadap bateri dalam populasi kajian hasil pemasangan Solargizer. Sebelum memulakan sebarang pengiraan, beberapa perkara juga perlu ditentukan. Antara aspek yang dipertimbangkan berkaitan kajian ini dihuraikan melalui Rajah 1.

Merujuk kepada Rajah 1, rawatan (*treatment*) bermaksud suatu perkara yang dikendali dan dikawal ke atas unit eksperimen oleh penyelidik. Dalam konteks kajian, ia merujuk kepada alat Solargizer yang dipasang dan diuji ke atas bahan eksperimen iaitu bateri. Tahap rawatan (*level of treatments*) berdasarkan kepada jenis rawatan yang digunakan. Oleh yang demikian, ia mengambil nilai sebagai $a = 2$ kerana hanya "bateri yang tidak dipasang Solargizer" dan "bateri yang dipasang Solargizer" adalah subjek bagi kajian. Selain itu, bilangan unit (*replicates*) merujuk kepada bilangan nilai data yang diperolehi dalam kondisi eksperimen yang sama.

Rajah 1: Antara aspek penting dalam teknik CRD.

Dengan menggunakan teknik CRD dalam kaedah ini, sampel data perlu diambil secara rawak dalam suatu populasi kajian. Bagi melaksanakan tujuan ini, terdapat tiga cara untuk mendapatkan nombor rawak dalam pemilihan sampel – pakej perisian komputer (contoh Microsoft Excel), Kaedah Loteri (*Lottery Method*) dan Jadual Nombor Rawak.

4. DAPATAN KAJIAN

Data daripada eksperimen makmal yang dijalankan akan diasingkan mengikut kumpulan tertentu di mana data daripada bateri-bateri yang menggunakan atau tidak menggunakan Solargizer akan dibentuk dalam sebuah jadual. Data-data ini mewakili tempoh masa yang dicatat oleh petugas-petugas makmal semasa pemerhatian mereka, mengikut prosedur-prosedur ujikaji dalam modul yang telah diberikan dan diselia oleh beberapa kumpulan penyelidik.

Masa yang dicatatkan apabila *voltmeter* menunjukkan nilai bacaan 10.50V adalah seperti di Jadual 1. Apabila proses menyahcas bateri berlaku, nilai *voltmeter* akan berkurangan daripada nilai asal sekitar 12.00V kepada nilai akhir yang dikehendaki iaitu 10.50V. Kadar pengurangan ini adalah disebabkan proses menyahcas menggunakan kapasiti cas bateri apabila tenaga elektrik dijana melaluinya.

Jadual 1: Tempohmasatamatbagi proses menyahcasuntuksetiapbateridenganatautanpaSolargizer. Masadiukurdalam unit minitapabilabacaan voltmeter menunjukkannilai 10.5 V.

Bateri Tanpa Solargizer	**Kitar (min)**																			
	1	2	3	4	5	6	7	8	9	10	11	12	13	14	15	16	17	18	19	20
Batt01	100	139	153	145	134	128	119	109	105	101	109	98	89	89	83	88	87	97	95	91
Batt02	75	161	174	166	175	167	170	165	163	127	150	142	130	110	99	90	85	94	87	81
Purata	87.5	150	163.5	155.5	154.5	147.5	144.5	137	134	114	129.5	120	109.5	99.5	91	89	86	95.5	91	86
Bateri Dengan Solargizer	**Kitar (min)**																			
	1	2	3	4	5	6	7	8	9	10	11	12	13	14	15	16	17	18	19	20
Batt01	156	134	157	151	156	158	140	135	135	133	108	105	110	116	108	103	120	96	91	83
Batt02	170	171	181	168	164	170	160	150	148	134	160	156	141	138	128	126	153	150	150	143
Purata	163	152.5	169	159.5	160	164	150	142.5	141.5	133.5	134	130.5	125.5	127	118	114.5	136.5	123	120.5	113

Jadual 2: Data mentah bagi populasi 40 tempoh masa yang dicatatkan di dalam ujian makmal.

Bateri	**Kitar (min)**																				*Jumlah*
	1	2	3	4	5	6	7	8	9	10	11	12	13	14	15	16	17	18	19	20	
Tanpa Solargizer	87.5	150	164	156	155	148	145	137	134	114	130	120	110	99.5	91	89	86	95.5	91	86	2385
Dengan Solargizer	163	153	169	160	160	164	150	143	142	134	134	131	126	127	118	115	137	123	121	113	2778
Jumlah	251	303	333	315	315	312	295	280	276	248	264	251	235	227	209	204	223	219	212	199	5163

Daripada jadual tersebut, terdapat empat buah bateri yang digunakan dalam eksperimen ini. Dua daripadanya dipasang Solargizer manakala dua lagi tidak menggunakan alat tersebut. Purata masa akan diambil bagi setiap dua buah bateri yang dipasang Solargizer begitu juga dengan dua buah bateri yang tidak dipasang. Bacaan purata tersebut akan diambil untuk proses analisis kerana kajian lebih berminat untuk mengetahui sama ada penggunaan Solargizer dalam bateri memberi kesan yang signifikan terhadap tempoh masa menyahcas. Proses menyahcas ini telah dikendalikan melalui prosedur-prosedur tertentu dan terpaksa melalui proses mengecas sebelum ia kemudiannya dinyahcas, sebagai satu kitar proses yang normal dalam operasi bateri yang digunakan.

Teknik CRD telah ditentukan untuk menganalisis data-data tersebut. Bagi memperincikan dengan lebih jelas, jadual baru telah dibentuk di mana purata yang dihitung (Jadual 2) diambil sebagai elemen utama dalam proses pengiraan selanjutnya. Bacaan purata ini mewakili tempoh masa tamatnya proses menyahcas bateri dengan populasi bagi 80 kali eksperimen (kitaran) yang dijalankan keseluruhannya. Walaubagaimanapun, kajian telah membentuk populasi baru dengan 40 nilai bacaan (Jadual 2). Kajian juga tidak memerlukan keseluruhan data dan memadai mengambil beberapa sampel daripadanya, yang akan mewakili populasi baru kajian seterusnya memberi inferens terhadap penggunaan Solargizer ke atas bateri.

Bagi menentukan sampel kajian diambil secara rawak, Jadual Nombor Rawak digunakan (Jadual 3). Nombor rawak akan dipilih daripada Jadual Nombor secara menegak dengan tiga digit pertama, bermula daripada mana-mana kedudukan yang dipilih. Apabila diaturkan secara menegak, pangkat (*rank*) diberikan bagi menentukan bacaan yang perlu diambil. Apabila Rawatan diselaraskan mengikut pangkat, bacaan daripada Jadual 2 ditentukan untuk dianalisis. Sampel telah ditentukan iaitu sebanyak 20 sampel data yang akan digunakan sebagai sampel kajian (Jadual 4). Setelah CRD menentukan jenis dan orientasi data yang sesuai untuk dianalis, Ujian Hipotesis dilaksanakan bagi mendapatkan inferens dan kesimpulan terhadap populasi kajian.

Langkah 1: Pernyataan Hipotesis

$H_0 = \mu_1 = \mu_2$ (min populasi bagi kedua-dua data adalah sama: Solargizer tidak memberi impak yang signifikan dalam meningkatkan keupayaan jangka hayat bateri kenderaan)

$H_1 = \mu_1 \neq \mu_2$ (min populasi bagi kedua-dua data adalah tidak sama: Solargizer memberi impak yang signifikan dalam meningkatkan keupayaan jangka hayat bateri kenderaan)

Jadual 3: Nombor rawak 3 digit yang disusun bagi mendapatkan 20 sampel datamenggunakanJadualNomborRawak (Table of Random Numbers).

No. rawak	Pangkat	Rawatan	
20	1	dengan	163
853	16	dengan	114.5
972	20	dengan	113
616	14	dengan	127
166	7	dengan	150
427	9	dengan	141.5
699	15	dengan	118
79	3	dengan	169
102	6	dengan	164
539	11	dengan	134
332	8	tanpa	137
34	2	tanpa	150
927	18	tanpa	95.5
856	17	tanpa	86
81	4	tanpa	155.5
512	10	tanpa	114
602	13	tanpa	109.5
949	19	tanpa	91
585	12	tanpa	120
99	5	tanpa	154.5

Jadual 4: Jadual yang dibentuk setelah 20 sampel rawak dipilih.

Bateri	Kitar (mins)										*Jumlah*
	1	2	3	4	5	6	7	8	9	10	
Tanpa Solargizer	137	150	95.5	86	155.5	114	109.5	91	120	154.5	**1213**
Dengan Solargizer	163	114.5	113	127	150	141.5	118	169	164	134	**1394**
											2607

Langkah 2: Pengiraan Statistik Ujian

$$SSA = \frac{y^2 i...}{bcn} - \sum \frac{y^2}{abc} \quad (1)$$

$$SSA = \frac{1}{10}\left(1213^2 + 1394^2\right) - \frac{2607^2}{20} = 1638.05$$

$$SST = \sum\sum\sum y^2 ijkl - \frac{y^2 ...}{abcn} \quad (2)$$

$$SST = \left(137^2 + 163^2 + 150^2 + ... + 164^2 + 154.5^2 + 134^2\right) - \frac{2607^2}{20} = 12117.05$$

$$\text{SSE} = \text{SST} - \text{SSA} \quad (3)$$

$$SSE = 12117.05 - 1638.05 = 10479.00$$

$$MSA = \frac{SSA}{d_f a - 1} \quad (4)$$

$$MSA = \frac{1638.05}{1} = 1638.05$$

$$MSE = \frac{SSE}{d_f abc(n-1)} \quad (5)$$

$$MSE = \frac{10479.00}{18} = 582.167$$

Keputusan pengiraan Ujian ANOVA di atas diringkaskan di dalam (Jadual 5).

Langkah 3: Nilai genting

Daripada jadual taburan kebarangkalian (Abdul Halim & Izham, 2000), nilai genting yang diperolehi ialah $F_{0.05,\ 1,\ 18} = 4.41$ (Jadual 6).

Jadual 6: Sebahagian Jadual F dengan α = 0.05.
(Sumber : Abdul Halim & Izham, 2000)

V_2 \ V_1	α = 0.05								
	Darjah Kebebasan Numerator								
	1	2	3	4	5	6	7	8	9
16	4.94	3.63	3.24	3.00	2.85	2.74	2.66	2.59	2.54
17	4.45	3.60	3.20	2.97	2.81	2.70	2.61	2.55	2.49
18	4.41	3.56	3.16	2.93	2.78	2.66	2.58	2.51	2.46
19	4.38	3.52	3.13	2.90	2.74	2.63	2.54	2.48	2.42
20	4.35	3.49	3.10	2.87	2.71	2.60	2.51	2.45	2.39
25	4.24	3.39	2.99	2.76	2.60	2.49	2.40	2.34	2.28
26	4.23	3.37	2.98	2.74	2.59	2.47	2.39	2.32	2.27
27	4.21	3.35	2.96	2.73	2.57	2.46	2.37	2.31	2.25
28	4.20	3.34	2.95	2.71	2.56	2.45	2.36	2.29	2.24
29	4.18	3.33	2.93	2.70	2.55	2.43	2.35	2.28	2.22
30	4.17	3.32	2.92	2.69	2.53	2.42	2.33	2.27	2.21

Langkah 4: Kesimpulan

Oleh kerana nilai statistik $F_{stat} = 2.814 < F_{nilai\ gnting}$ maka gagal tolak H_0 (Rajah 4).

Langkah 5: Keputusan

Tidak terdapat bukti yang cukup untuk menyatakan bahawa penggunaan Solargizer memberi kesan yang signifikan ke atas peningkatan keupayaan jangka hayat bateri. Ini menunjukkan tiada perbezaan antara bateri yang menggunakan Solargizer dan tidak menggunakan Solargizer dalam populasi kajian.

Jadual 5 : Jadual rumusan ANOVA.

Punca Variasi	SS	Df	MS	F
Rawatan	1638.050	1	1638.050	2.814
Ralat	10479.000	18	582.167	
Jumlah	12117.050	19		

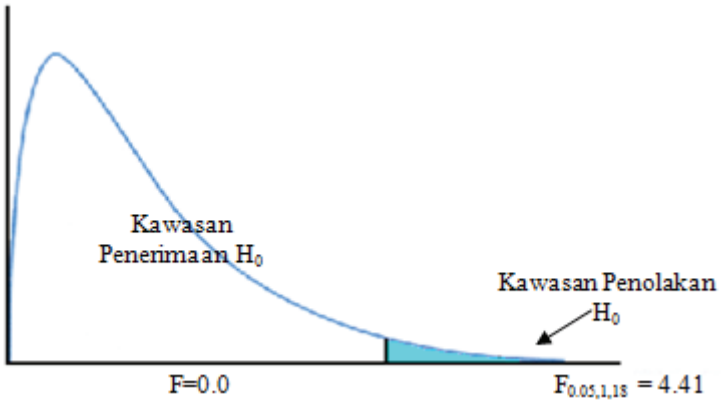

Rajah 4: Graf Nilai F bagi Taburan F dengan aras keertian α =0.05.

5. LIMITASI

Penggunaan Solargizer merupakan satu alternatif yang baik bagi mengurangkan kadar kerosakan bateri dengan lebih cepat (PulseTech Products, 2001). Sungguhpun begitu, terdapat banyak lagi alatan sedemikian yang boleh diuji bagi mengenalpasti keberkesanannya terhadap bateri kenderaan. Sekiranya pengkaji dapat menjalankan pengujian terhadap pelbagai jenis Solargizer dan tidak hanya tertumpu kepada satu alternatif sahaja, ini akan memberi keputusan yang lebih baik. Selain itu, data-data yang diperolehi mungkin dapat dianalisis dengan menggunakan kaedah lain seperti Kaedah Peramalan (*Forecasting*), Simulasi (*Simulation*) dan Heuristik (*Heuristic*) bagi memperolehi keputusan kajian yang lebih menyeluruh. Teknik-teknik lain dalam kaedah DOE mungkin juga dapat diaplikasikan berdasarkan data ujikaji yang tepat dan relevan terhadap objektif kajian.

Selain itu, terdapat juga kebarangkalian wujudnya ralat dalam perekodan data yang tidak konsisten dan kehilangan beberapa data yang penting dalam aspek kajian. Keadaan ini akan mempengaruhi keputusan pengiraan kerana ia bergantung kepada nilai bacaan yang diambil. Di samping itu, populasi kajian juga terhad kepada kuantiti yang kecil relatif kepada penggunaan Solargizer ke atas bateri. Secara tidak langsung, ini juga boleh mempengaruhi keputusan kajian kerana kebarangkalian sampel yang dipilih tidak dapat menunjukkan variasi yang signifikan ke atas data-data bagi mewakili sesuatu populasi.

6. KESIMPULAN

Daripada kesimpulan terhadap ujian-ujian statistik yang dibuat, dapat dirumuskan bahawa kaedah Rekabentuk Ujikaji dengan teknik CRD yang digunakan tidak konsisten dengan tanggapan dan anggapan asal terhadap Solargizer. Kajian ini menunjukkan tiada perkaitan di antara min bagi dua populasi bateri, dengan atau tanpa penggunaan Solargizer, terhadap jangka hayat bateri. Ini jelas menunjukkan bahawa penggunaan Solargizer ke atas bateri bagi populasi kajian tidak memberi kesan langsung yang signifikan terhadap keupayaan kapasiti bateri. Kajian yang dibuat oleh kilang pembuat Solargizer telah membuktikan bahawa penggunaan Solargizer memberi impak dan berupaya memanjangkan jangka hayat bateri

bagi sesuatu kenderaan (Industrial Solargizer, 2007). Perbezaan keputusan kajian ini dengan kajian-kajian lepas yang dilakukan terhadap penggunaan Solargizer adalah mungkin kerana terdapat ralat pada data yang diambil semasa ekperimen yang dijalankan. Selain itu juga, kajian ini hanya tertumpu kepada satu jenis Solargizer sahaja.

PENGHARGAAN

Penulis ingin merakamkan penghargaan kepada Dr Mahdi Che Isa, Pn Kathryn Tham Bee Lin dan Pn Jamaliah Mohd Noor kerana turut membantu dalam menjayakan kajian dan penyediaan artikel ini.

RUJUKAN

Abdul Halim, A. & Izham, S. (2000). *Sifir Statistik*. Universiti Utara Malaysia, Sintok, Kedah.

Buchmann, I. (2011). *Batteries in a Portable World - A Handbook on Rechargeable Batteries for Non-Engineers, 3rd Edition*. Cadex Electronics Inc., Richmond, British Columbia.

Chua Y.P. (2006). *Kaedah dan Statistik Penyelidikan*. Mc Graw Hill (Malaysia) Sdn. Bhd. Kuala Lumpur.

Crompton, T.R. (2000). *Battery Reference Book*. SAE International, Warrendale,Pennsylvania.

Global Merchants (2000). *Solargizer Battery Maintainers*. Available online at: http://www.global-merchants.com/home/solargzr.htm (Last access date: 10th Januari 2011).

Hazura, M., Muhammad Hisyam, L., Mazalam, S., Shaharuddin, S. & Bahrom, S. (2009). Application of Taguchi's Design of Experimental in performance analysis of destination sequence distance vector (DSDV) routing protocol in mobile ad hoc networks. *Sains Malaysiana*, **38**: 423-428.

Hinkelmann & Kempthorne. (2008). *Introduction to Experimental Design*, *2nd Ed.* John Wiley & Sons, Inc, Hoboken, New Jersey.

Howell, D.C. (1999). *Fundamental Statistics For The Behavioral Sciencse*. 4th Edition. Brooks/ Cole Publishing Co. California.

Industrial Solargizer (2007). *IS-24-L 24 Volt Industrial Solargizer*. Available online at: http://www.chargingchargers.com/pulsetech/is-24-l.html (Last access date: 10th Nov 2010).

Linden, D. & Reddy, T.B. (2001). *Handbook of Batteries*. McGraw-Hill, New York.

PulseTech Products Corporation (2001). *Solargizer Battery Maintenance System.* Available online at: http://www.pulsetech.net/products/Manuals/solargizer/SOL_Manual.PDF (Last access date: 8th February 2011).

Rasimah Aripin. (2005). *A Guide To Data Management and Analysis Using SPSS*. Universiti Teknologi MARA UiTM), Shah Alam, Selangor.

Institute Penyelidikan Sains & Teknologi Pertahanan (STRIDE) (2002). Laporan Ujinilai ke atas Peralatan *Pulsetech Battery Maintenance System* bagi Kegunaan Angkatan Tentera Malaysia. Institute Penyelidikan Sains & Teknologi Pertahanan (STRIDE), Kementerian Pertahanan, Malaysia.